Trinity College Dublin
Coláiste na Tríonóide, Baile Átha Cliath
The University of Dublin

Master Dissertation

Theoretical and experimental study on electron transport in oxygen-plasma-treated monolayer MoS_2

Author:
Gen Li

Supervisors:
Prof. Hongzhou Zhang
Prof. James Lunney

May 31, 2019

Declaration

I declare that this thesis titled, "Theoretical and experimental study on electron transport in oxygen-plasma-treated monolayer MoS_2" and the work presented in it are my own. I confirm that:

- This thesis has not been submitted as an exercise for a degree at this or any other university and it is entirely my work. Where any part of the thesis has previously been submitted for a degree or any other qualification at this University or any other institution, this has been clearly stated.
- This work was done wholly or mainly while in candidature for a research degree at this University.
- I agree to deposit this thesis in the University's open access institutional repository or allow the Library to do so on my behalf, subject to Irish Copyright Legislation and Trinity College Library conditions of use and acknowledgement.
- Where the thesis is based on work done by myself jointly with others, I have made clear exactly what was done by others and what I have contributed myself.
- Where I have quoted from the work of others, the source is always given. With the exception of such quotations, this thesis is entirely my own work.
- I have acknowledged all main sources of help.
- This dissertation does not exceed 60,000 words in length.

Signed:

Date:

I have read and I understand the plagiarism provisions in the General Regulations of the University Calendar for the current year, found at http://www.tcd.ie/calendar.

Signed: ____

I have also completed the Online Tutorial on avoiding plagiarism 'Ready Steady Write', located at http://tcd-ie.libguides.com/plagiarism/ready-steady-write.

Signed: ____

July 9, 2019

Summary

In recent years, two dimensional (2D) molybdenum disulfide (MoS_2) has attracted wide a range of interest due to its interesting physics properties, such as valley electronics and quantum spin Hall effect, and its potential applications for the semiconductor industry such as in field-effect transistors (FETs) and photodetectors.

Chapters 1 to 4 contain background knowledge related to this work, including the crystal structures of MoS_2, plasma engineering, density functional theory (DFT) and the transfer matrix method (TMM).

In Chapter 5, we introduce the experimental instruments used in this work, including mechanical exfoliation, electron beam lithography (EBL), Atomic Force Microscopy (AFM), Raman and photoluminescene (PL) spectroscopy, and an electrical measurement system.

In Chapter 6, we utilize radio-frequency oxygen plasma to treat 2D MoS_2 FET to enhance the performance of the device. We study the surface morphology of the same device before and after a two-second rapid plasma treatment. We find that the surface thickness to be doubled after treatment by using AFM. We find that both Raman E and A peaks are attenuated. An A exciton peak is quenched and broadened from PL spectroscopy. We further conduct electrical measurements to evaluate the device performance. We find that photoresponsivity and mobility are enhanced after 2s of oxygen plasma exposure. The threshold voltage of the device shifts to a more negative value, indicating the FET becomes more easily switched on. Moreover, we also utilize polymer encapsulation technique to modify the device. We find that polymer protection can improve the device mobility and significantly enhance the device stability. The polymer protection technique can further be utilized to realize site-specific modification on MoS_2. This Chapter gives insight into surface modification and mobility engineering of 2D MoS_2 nano devices.

In Chapter 7, based on the experimental observations in Chapter 6, we apply DFT to study the electronic and magnetic properties of oxygen-plasma-treated monolayer MoS_2. We consider three types of unit cells, which are proposed based on our experimental observation in the Chapter 6. We firstly

optimize the lattice parameters of the studied unit cells. We further combine the three types of unit cell to make various 2×2 super cells. By calculating their band structures, we find that sulphur vacancies can cause significant quenching of band gap and that oxygen adatoms can make the direct band gap of pristine MoS_2 to indirect band gap. Moreover, from the spin-dependent DOS, we also find that neither sulphur vacancies nor oxygen adatoms can introduce a ferromagnetic phase in to ML MoS_2, which is consistent with previous work. Regarding spin-orbit coupling, our calculate SOC strength of pristine MoS_2 is consistent with previous work. Oxygen adatoms can cause the location of band splitting to change, which is attributed to the modification of band structure by oxygen adatoms. This Chapter gives insights into band-structure engineering and valley electronics of 2D materials.

In Chapter 8, we firstly show how to fabricate MoS_2/MoO_x heterostructures using a plasma. Then, we study the electron transport in it by TMM. We analyse the tunneling process in a double-well structure and step-well structures under the condition of electric field and no electric field. Our work shows that the increasing of transverse momentum will result in the red shift of the resonant peak. We also show that low electric fields ($\pm 0.3\ V$) can enhance the magnitude of peaks and intensify the coupling between longitudinal and transverse momentums. However, it can't optimize the resonant tunnelling condition due to the heavier electron effective mass of MoS_2/MoO_x heterostructures than that in traditional semiconductor superlattices. Thus, a higher bias is applied and ideal resonant tunnelling peaks are obtained, indicating that negative differential resistance (NDR) effect can be observed. Moreover, a step-well structure shows a better performance regarding resonant tunnelling than a double-well structure, due to the absence of well separation, which can alter the phase of electrons to affect resonant tunnelling condition. This Chapter gives insights into the physics of resonant tunnelling effect and NDR in 2D-materials nano devices, and also sheds light on the design of quantum electronic devices.

Acknowledgements

I would like to thank my supervisors Prof. Hongzhou Zhang and Prof. James Lunney for the huge amount of help and guidance they have shown me to date. I would also like to thank members of both research groups for their assistance. In particular, Jakub Jadwiszczak and Darragh Keane for their help at every step along the way, Prof. Yangbo Zhou for training me on experimental skills and sharing his profound theoretical knowledge, Jingjing Wang and Pierce Maguire for their assistance with Raman microscopy. I would also like to thank James Creel for establishing the inductively-coupled plasma chamber and sharing his profound knowledge of plasma engineering, Taj for establishing the inductively-coupled plasma jet and sharing his profound knowledge of atmospheric plasma, colleagues from Paula's group for training me on the plasma chamber. Thanks Danny Fox for doing TEM imaging and characterization. Thanks Niall McEvoy's group for sharing CVD samples.

Here, I would like to give my sincere gratitude to the following people. Without them I certainly would not have been able to come this far.

My high-school classmate Boyuan Ning who teaches me advanced mathematics, including functional analysis, group theory and differential geometry.

My undergraduate classmate Zhaowei Cai who teaches me basic particle physics and Relativity.

My undergraduate classmate Junwen Zheng who teaches me density functional theory. My friend Bosoni who teaches me the algorithm of DFT.

I would like to thank the innovation of Internet due to the huge knowledge and resources I have absorbed from it.

I would like to thank my mother, father and relatives who have given huge support to me since I was born both financially and mentally.

I would like to thank my girlfriend Ms. Tong for her warm-hearted mental support over the past two years.

Contents

Chapter 1

Introduction

Conventional integrated circuits (ICs) are based on Si metal-oxide-semiconductor field-effect transistors ($Si\ MOSFET$).[1, 2] The fabrication and integration techniques of the device have evolved rapidly, and processors with five billion MOSFETs have been commercialized. However, the gate length of the most advanced Si MOSFET is 20 nm, beyond which quantum tunnelling effect will play an important role. This applies a fundamental barrier to Moore's law and research in the field, resulting in the conception of More Than Moore.[1]

More than Moore is not primarily targeted on increasing circuit complexity but rather on enhancing functionalities of individual devices. The emergence of graphene and other two-dimensional (2D) materials that exhibit abundant new properties enables novel types of nano devices.[3, 4] Extensive research effort has been concentrated on 2D field-effect transistors (2D FETs) whose channel materials are 2D materials. These novel devices reveal great potential to meet the requirements of More Than Moore.

Graphene FETs used to be the first candidate for post-silicon electronics due to their incredible mobility.[5] However, in graphene, the lack of bandgap and poor power gain make graphene FETs impractical to logical applications - the device cannot be properly turned off.[6, 7] The emergence of thin-film MoS_2 brought new vitality to the study of 2D FETs. Monolayer MoS_2 with direct bandgap 1.9 eV and electron effective mass 0.39 m_e not only meets the requirement of an effective off state but also overcomes the difficulty of the short-channel effect, a major challenge in the FET miniaturization.[2, 4] Moreover, monolayer MoS_2 also has great photoresponsivity to a broad range of wavelengths, which makes them a good candidate for nanoscale photoelectronics.[8, 9]

The most important issue of 2D MoS_2 FETs is its relatively low mobility. For pristine MoS_2, the theoretical mobility value at room temperature is about 410 $cm^2\ V^{-1}\ s^{-1}$.[10] However, the mobility of 2D MoS_2 FETs is several hundred centimeters squared per volt-second lower than Si MOSFETs and the existing experimental extracted mobilities from MoS_2 MOSFET structures are between $1 \sim 300\ cm^2\ V^{-1}\ s^{-1}$.[11, 12, 13, 14] It is crucial to understand the effects that degrade the mobility and to seek a practical approach to enhance it. In addition to low mobility, other problems also exist, such as contact resistance, fabrication method, etc.

Plasma treatment is one of the backbones of modern semiconductor industry. Regarding the microfabrication of an IC, one-third of the tens to hundreds of fabrication steps are typically plasma based.[15] Reasons for which one utilizes plasma to conduct massive production of ICs are anisotropy and manageable parameters.[15] It is indubitable that plasma has been a powerful tool in materials treatment.

Moreover, monolayer MoS_2 has also attracted a wide range of interest in terms of the study of fundamental physics. In the first Brillouin zone, the K and $-K$ valleys are related to one another by time reversal.[16] The band edges of the conduction and valence bands are located at $\pm K$ valleys.[17] If we study the electronic behaviour at the $\pm K$ valleys to first order, we find electrons are described by massive Dirac Fermion.[18] However in graphene, it is well known that the linear dispersion relation leads a massless Dirac Fermion behaviour. Moreover, the coupled spin and valley indices can cause a more complex interband selection mechanism during the photoexcitation process,[18] which has been observed by polarization-resolved photoluminescene.[19, 20] The spin-orbit coupling effect in MoS_2 has also been studied. Tight-binding method, DFT and $\mathbf{k} \cdot \mathbf{p}$ method give the same result that the band splitting between spin up and down electrons at K and $-K$ valleys are opposite.[17, 21, 22] This interesting spin-orbit coupling effect also gives insight into spintronics, like valley- and spin-dependent spin filters.[23, 24]

Chapter 2

Two-dimensional Molybdenum disulfide and plasma engineering

2.1 Molybdenum disulfide

Crystal structure

Molybdenum disulfide is the main ingredient of molybdenite. Its chemical formula is MoS_2. It belongs to the family of transition metal dichalcogenides. Its melting point is 1185 ^oC. In ambient conditions, it is chemically stable and starts being oxidised into MoO_3 when temperatures increase to 315 ^oC. Molybdenum disulfide has been commercialized as a solid lubricant, especially under high temperature and pressure.

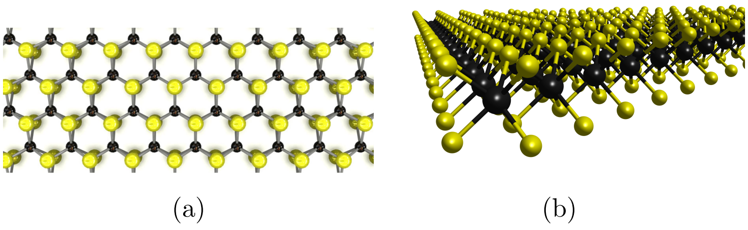
(a) (b)

Figure 2.1: Crystal structures of monolayer MoS_2. (a) is the top-view image showing two dimensional hexagonal geometry, (b) is the cross section image showing a sandwich structure with molybdenum atoms sandwiched by sulphur atoms.

In this work, we focus on two dimensional MoS_2. In Fig. 2.1, for each layer, it is a sandwich structure, with a hexagonal coordination from the top view. Van der Waals interaction connects two different layers together, similarly to bilayer graphene. The typical thickness of single layer MoS_2 is 0.6 nm. A few-layer MoS_2 flake can exist in three different phases. They are 1T, 2H and 3R, indicating different ways of stacking of layers. The phases of bulk MoS_2 found in nature are usually 2H and 3R, with H and R referring to hexagonal and rhombohedral symmetry. For 1T phase (T stands for Trigonal), it can be obtained by intercalating 2H MoS_2 with alkali metals.[25]

Band structure

The lattice structure of monolayer MoS_2 is hexagonal. So, its reciprocal space also has a hexagonal geometry (Fig. 2.2). By choosing the path $\Gamma - M - K - \Gamma$ in the first Brillouin zone, the band structure is shown in Fig .3.[26]

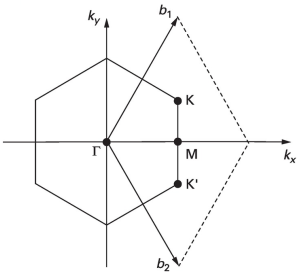

Figure 2.2: First Brillouin zone of monolayer MoS_2 with high symmetry points shown (Γ, M and K). Graphic reproduced from [27] by P. Avouris *et al.*

In Fig. 2.3, it can be seen that the bulk MoS_2 crystal is an indirect-gap semiconductor with a band gap of 1.29 eV.[28] With thickness of the MoS_2 flake reducing to a single layer, not only does the gap increase to 1.84 eV, but also the indirect gap transforms to a direct gap. Due to its direct band gap, monolayer MoS_2 has good photoresponsivity and photoluminescence. Moreover, by calculating the second derivative of the band energy with respect to reduced momentum, the electron effective mass in monolayer MoS_2 is 0.39 m_e (m_e is the rest mass of an electron).[26]

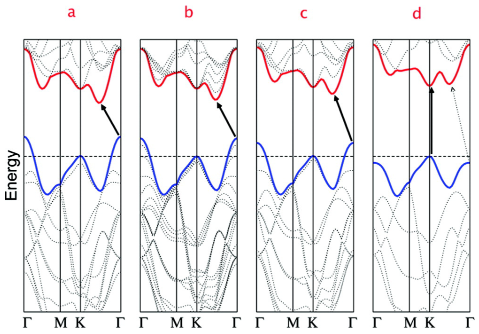

Figure 2.3: Band structures of (a) bulk MoS_2, (b) quadrilayer MoS_2, (c) bilayer MoS_2, and (d) monolayer MoS_2. Graphic reproduced from [28] by Splendiani *et al.*

2.2 2D field-effect transistors

Threshold voltage

The threshold voltage V_{th} is one of the most important parameters in FETs. A simple definition of V_{th} is the voltage where the channel current starts to increase exponentially. A strict definition is that gate voltage for which the surface potential ϕ_s in the semiconductor below the gate oxide is given by[29]

$$\phi_s = 2\phi_F = \frac{2kT}{q} ln(\frac{n_h}{n_e}) \tag{2.1}$$

for an n-channel MOSEFT. This equation is based on equating the surface minority carrier density to the majority carrier density in the neutral bulk. Here, ϕ_F is the Fermi level of semiconductor. n_h and n_e are surface minority carrier density and bulk majority carrier density, respectively.

The V_{th} can be extracted from the transfer curve. Based on established knowledge, there are several ways to extract V_{th}. In this work, we introduce four commonly used methods. They are constant-current method (CC), extrapolation in the linear region method (ELR), transconductance extrapolation in the linear region method (GELR) and ratio method (RM).[29, 30]

CC method evaluates the V_{th} by choosing an arbitrary constant drain current, for example $I_{ds} = 10^{-7}\ A$. It is widely used in the well-established Si MOSFET industry due to its simplicity. However, the severe disadvantage of

CC method is an incomparability resulting from the arbitrarily chosen drain current.

ELR and GELR methods both aim at calculating the x-axis (gate voltage) intercept to obtain V_{th}. The difference is that ELR uses x-axis intercept from the transfer curve, while GELR uses that from the curve of transconductance *vs.* gate voltage. Both of them can be strongly influenced by parasitic series resistances and mobility degradation effects.

The Ratio method (also called Y method) was developed to avoid the dependence of parasitic resistance and mobility degradation. By dividing source-drain current by the square root of transconductance, the mobility degradation factor can be eliminated. The gate dependent source current is commonly defined as [29]

$$I_d = \frac{WC_{ox}}{L}\frac{\mu_0}{[1+\theta(V_g - V_{th})]} \cdot (V_g - V_{th}) \cdot V_d \tag{2.2}$$

Differentiation of Eq. 2.2 with respect to V_g gives the transconductance g_m,

$$g_m = \frac{WC_{ox}}{L}\frac{\mu_0}{[1+\theta(V_g - V_{th})]^2} \cdot V_d \tag{2.3}$$

Here, W and L are the channel width and length. C_{ox} is the gate oxide capacitance. μ_0 is the low-field mobility and θ is mobility reduction factor. V_g, V_{th} and V_d are the gate voltage, threshold voltage and source-drain voltage, respectively. Equation 2.2 shows that the intercept of x-axis equals the threshold voltage. However, the slope contains a term θ which involves both mobility reduction factor θ_0 and parasitic resistance R_{sd}.

$$\theta = \theta_0 + R_{sd}C_{ox}\mu W/L \tag{2.4}$$

Thus, the mentioned methods, such as ELR and GMLE, are sensitive to parasitic resistance and mobility degradation. However, by dividing the source current by the square root of the transconductance, an expression with slope not containing the factor θ can be obtained,[31]

$$\frac{I_d}{g_m^{1/2}} = (\frac{WC_{ox}}{L}\mu_0 V_d)^{1/2}(V_g - V_{th}) \tag{2.5}$$

In Eq. 2.5, the factor θ is eliminated, suggesting that extraction of V_{th} can exclude effects caused by parasitic resistance and mobility degradation.

Mobility

The carrier mobility plays an important role in determining the device performance. In a low electric field, the carrier velocity is proportional to the electric field strength. Thus, materials with a higher mobility lead to higher frequency response. Especially in radio frequency circuits, how fast an electron can response to an electric field mainly determines the device performance. In a semiconductor, there are two types of charge carriers (electrons and holes). Both of them have mobilities. Usually, the mobility of a hole is larger than that of electron since it has larger effective mass. In this project, we focus on the electron mobility because MoS_2 FETs are typically n-type.

The general electron mobility is defined by $\mu = \frac{v_e}{E}$. v_e and E are electron speed and electric field strength. The commonly used unit of mobility is $cm^2\ V^{-1}\ s^{-1}$. The electron mobility of a pristine material is determined by its effective mass whose value is proportional to the second derivative of the band structure (Energy *vs.* reduced momentum). Electron mobility is significantly affected by other factors, such as impurity scattering, phonon scattering, lattice defects scattering and etc. All these factors causing mobility reducing are called mobility degradation effect. Each scattering mechanism corresponds to a mobility. According to Mathiessen's rule,[29] the net mobility μ is,

$$\frac{1}{\mu} = \frac{1}{\mu_1} + \frac{1}{\mu_2} + \cdots \tag{2.6}$$

To be specific, in the case of an FET, the electric field is applied perpendicular to the planar device by either back or top gating. The mobility is named field-effect mobility (μ_{fe}), referring to how fast an electron can response to the gate field. The expression of μ_{fe} is,

$$\mu_{fe} = \frac{L}{W C_{ox} V_{ds}} \frac{\partial I_{ds}}{\partial V_g} \tag{2.7}$$

Where C_{ox} is oxide capacitance, with $C_{ox} = \epsilon_0 \epsilon_r / d_{ox}$. ϵ_0 is vacuum dielectric constant with value $8.85 \times 10^{-12}\ F \cdot m^{-1}$. ϵ_r is the dielectric constant of SiO_2, which is a back gate material, with value $\epsilon_r \sim 3.9$. L and W are channel length and width, respectively. V_{ds} is the source drain voltage, which is usually set below one volt to help carriers drifting. $\partial I_{ds}/\partial V_g$ can be extracted from the transfer curve, which is also called transconductance.

Conductivity

In a 2D FET, the current flow is in the plane of the sheet, without a perpendicular component. In a normal three-dimensional conductor, the resistance can be written as $R = \rho L/S$. ρ is the resistivity, L and S are length and cross-section area. For a bulk conductor, resistivity is in units of $\Omega \cdot cm$. When the thickness thins to thin films with negligible thickness, the unit of sheet resistivity will change to $\Omega \cdot cm/cm = \Omega$, which is same as the bulk resistance. In order to distinguish the sheet resistivity from bulk resistance, one uses "Ohms square (Ω/sq)" as the unit for sheet resistivity. [11, 32]

The sheet conductivity of a 2D FET is the reciprocal of its resistivity, and can be extracted from the output characteristics,[11]

$$\sigma_{sheet} = \frac{L}{W}\frac{I_d}{V_d}, \tag{2.8}$$

where L and W are channel length and width, while V_d and I_d are source-drain voltage and current.

2.3 Plasma engineering

Plasma state

Plasma state is the fourth state of matter, along with solid, liquid and gas. For a system composed of gas, if the temperature further increases, then the atoms decompose into freely moving charged particles, and the substance enters the plasma state. This state is characterized by a common charged particle density $n_e \approx n_i$. In equilibrium, the temperature is characterised as $T_e = T_i$. Here, T_e and T_i refer to electron and ion temperatures respectively.

Plasma widely exists in both nature and our daily life. In the nature, sunlight is generated by nuclear fusion of the plasma state within the sun. Sixty kilometers above the ground, the ionosphere is also a plasma state ionized by the solar radiation and cosmic rays. In our daily life, the most common plasma is energy-saving bulb where a filament is heated to about 1000K to generate electrons to ionize Ar plasma. Plasma has also been widely employed to treat the materials surface and modify its functions, such as integrated circuit mass production, welding and sterilization.

In this work, we utilize plasma to treat and modify 2D materials (MoS_2) in order to enhance their performance for the interests of electronics applications. Thus, we focus on controllable artificial plasma rather than natural plasma.

Plasma sheath

If a plasma exists between two walls with width l, the electric potential ϕ and the electric field E are zero in the bulk, since $e(n_i - n_e) = 0$, indicating the bulk region is quasi-neutral. Hence, the fast-moving electrons are not confined and will rapidly be lost on the wall on a very short timescale. The net positive charge ρ within the sheaths leads to a potential profile $\Phi(x)$ that is positive within the plasma and falls sharply to zero near both walls. The region where the electric potential falls sharply from the bulk to the wall is called the plasma sheath. Obviously, ions in the sheath can be accelerated due to the presence of large potential gradient, leading the potential applications for surface science. Indeed, the semiconductor industry utilizes the ions within the sheath to etch silicon wafers mounted on substrates connected to RF (radio frequency) supplies (see Fig. 2.4).

Plasma discharges

The principle of direct current (DC) glow discharge is to utilize a high voltage to break down the neutral gas and maintain it using electrons generated at the cathode. The normal operating pressure ranges from 10 $mTorr$ to 10 $Torr$. Several kilovolts are needed to ignite the plasma and a few hundred volts are needed to maintain the plasma. In order to have a clear physics image of DC discharge, the relationship between breakdown voltage and related

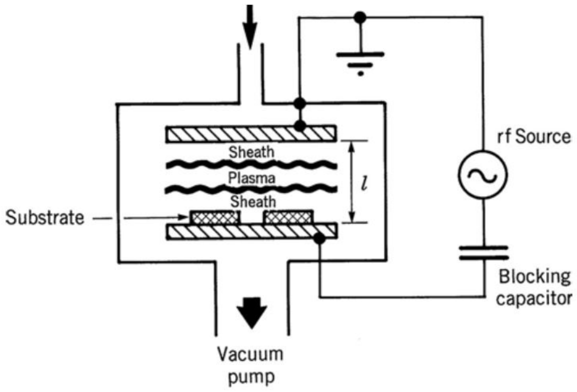

Figure 2.4: Sketch of RF plasma etching silicon wafer. Graphic reproduced from [15] by A. Michael *et al.*

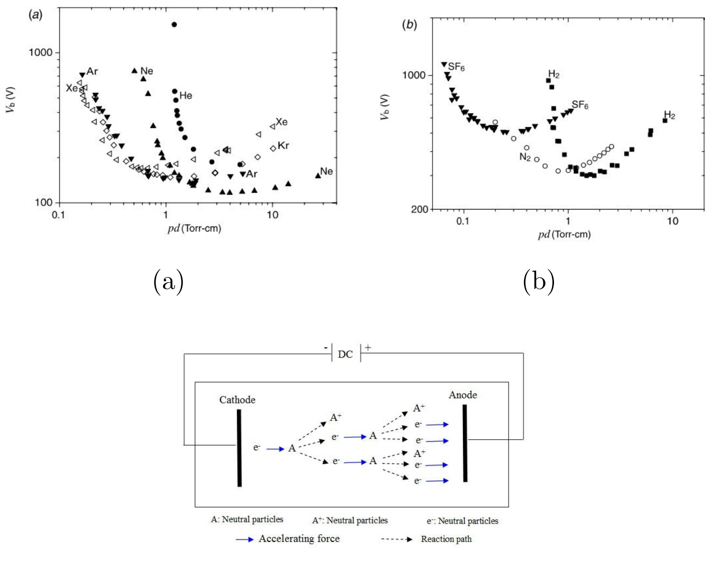

(a) (b)

(c)

Figure 2.5: (a) and (b) are Paschen curves of breakdown voltage for plane-parallel electrodes at 20 ^{0}C for noble gases and molecular gases. (c) is an illustration of DC discharge. Graphics reproduced from [15] by A. Michael *et al.*

parameters is needed, which is called Paschen's Law. Paschen's Law (Fig. 2.5 (a) and (b)) describes how pressure and distance between two electrodes affect the breakdown voltage.

Capacitive discharges are plasmas generated within a parallel-plate capacitor and driven by radio-frequency power supply (Fig. 2.6). A clear physics image of capacitive discharges can be understood by analogy to the relationship between resistance and capacitor. For a DC power supply, current can pass through a resistance, but it is not able to pass through a capacitor. The same circumstance holds for DC plasma discharges, both electrodes and plasma are conductive to allow current to pass through. However, if we mount silicon wafers onto one electrode (Fig. 2.4), the region between the two electrodes will become an insulator for a DC power supply. Hence, we can introduce an AC power supply to maintain the system since the geometry of electrode-insulator-electrode can be regarded as a capacitor. In order to maintain the plasma discharges with a high efficiency, one prefers to utilize high-frequency power supply to avoid charging the insulator. The reason to define 13.56 MHz as the commonly used discharge frequency is to avoid interfering the radio communications.

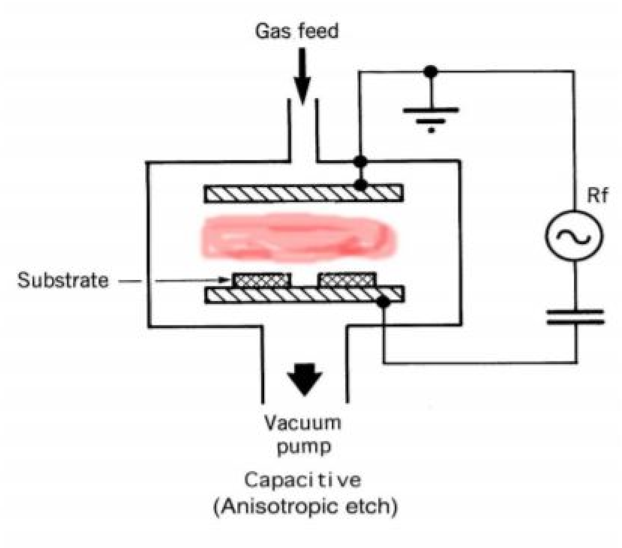

Figure 2.6: Illustration of a capacitive plasma driven by RF source for silicon wafer etching. Graphic reproduced from [15] by A. Michael *et al.*

Figure 2.7 is a common setup for inductively-coupled plasma (ICP). As can be seen, several turns of coils are wrapped onto a cylindrical chamber. Coils connected with RF power supply are utilized to generate vortex electric field inside the chamber to heat up and ignite the plasma. The commonly driven frequency is also 13.56 MHz. The advantage of ICP is that it can avoid sputtering on the cathode caused by ions, compared with the direct connection between electrodes and plasma in capacitively-coupled plasma (CCP).

One combines ICP and a mass spectrograph together, utilizing charged particles in ICP to atomise the specimen. Then, the highly atomised specimen can be analysed by mass spectrograph. Thus, ICP has been widely used for trace analysis, including materials science, geoscience and crime analysis.

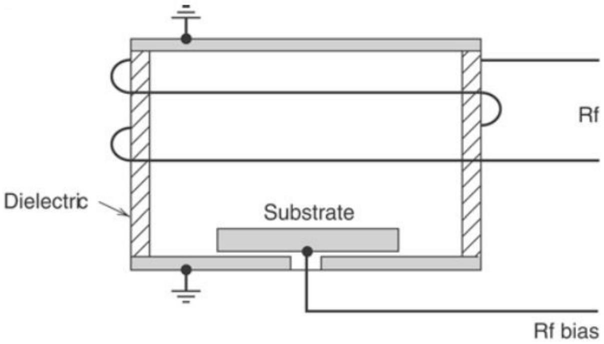

Figure 2.7: Configuration of an inductively coupled plasma driven by RF power supply. Graphic reproduced from [15] by A. Michael *et al.*

Plasma and materials processing

Plasma has been widely used to treat and modify materials. The process of treatment involves different reactions, making the mechanism of treatment complicated. As can be seen in Fig. 2.8, it includes thin film deposition, cleaning, etching, modification and activation. Among them, the knowledge of cleaning and etching have already been well established, and commercialized for more than a decade. In this work, we focus on the modification section in order to make contributions to achieving the goal of *More than Moore*.[1]

The physics image of plasma-surface interaction is clear. Assuming that we can zoom in to the scale of microscopic world, and we can watch the interactions between particles in a plasma and particles on a surface (see Fig. 2.8). Thus, we can gain some insights into which parameters will affect the interaction, such as pressure, plasma power, gas composition, flow rate, exposure time, exposure location and surface materials, etc.

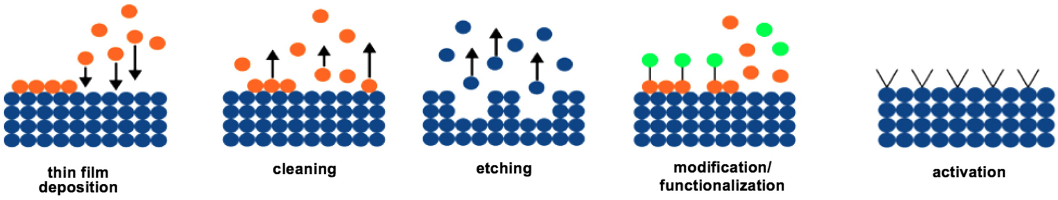

Figure 2.8: Different interactions between plasma and surface. Graphic reproduced from [33] by Von Woedtke *et al.*

In terms of plasma treatment of MoS_2, most researchers focus on oxygen and argon plasma. Oxygen plasma can introduce the effect of photoluminescence quenching in monolayer MoS_2. The corresponding experimental parameters are a gas composition with oxygen (20%) and argon (80%), input power of 100 W with driving frequency 50 kHz, under pressure 250 $mTorr$ and a flow rate 15 $sccm$.[34] The flow unit $sccm$ is defined as standard cubic centimeters per minute (cm^3/min). MoO_3 can be obtained based on remote-oxygen-plasma treatment on MoS_2 after 5 min or longer.[35] Samples were placed far away from the plasma zone (52 cm).[35] Zhu *et al* tried different treatment times, 1, 5 and 20 mins.[35] They also controlled the substrate temperature under three different values 100, 200 and 400 ^0C.[35] Their plasma power was 2500W with RF frequency 1.9-3.2 MHz, and oxygen flow rate 130 $sccm$.[35] The pressure during treatment was 6 $mbar$.[35] Brown reported that oxygen plasma can introduce oxidation and cause the loss of sulphur.[36] Their operation pressure was 1×10^{-6} $mbar$.[36] Their samples were placed at the bottom of the chamber.[36] Additional self-bias was used to accelerate the ions onto samples.[36] Regarding pure argon plasma, Inoue *et al* reported that concave surface defects can be generated in MoS_2 via Ar^+ ions.[37] Their ion density was 2.75×10^{-3} $ions/nm^2$ and ion energy was 500 eV.[37] Their operation pressure was 2×10^{-8} pa.[37]

Plasma treatment on graphene and carbon nanotube has also been widely studied. Ye *et al* reported that $N_2 : He = 1 : 49$ plasma can generate a clear written area in graphene and introduce disorder and defects in the lattice.[38] Their total flow rate was 50 *sccm*. Ref [38] also showed that the density of the jet has an order of 10^{12} cm^{-3} including various reactive species. Their energy of ions was kept at a very low level (below 0.1 eV).[38] A nozzle with a diameter of 2 μm was shown to generate a 10 μm width written area under a moving speed 0.5 mm/min.[38] The distance between the nozzle and sample was 3 mm.[38] Concerning CNT, consistent conductance CNT FETs can be obtained by oxygen plasma treatment with such experimental parameters as plasma power 100 W, flow rate 90 *sccm*, and pressure 300 $mTorr$.[39] Moreover, oxygen-plasma treatment can remove amorphous carbon and generate defects with such experimental parameters as vacuum value 100 $mTorr$ and RF frequency 13.56 MHz.[40] Yeo *et al* reported that the sensitivity of carbon nanotube based sensors can be enhanced 74 times through surface modification by oxygen plasmas.[41] Their plasma setup was an inductively coupled plasma with an operating pressure of 270 $mTorr$.[41] Their plasma power was 10 W.[41] The flow rate was 15 *sccm*.[41] The exposure time was set at 0, 5 and 20 s.[41] The plasma was generated 8 *cm* away from the samples.[41]

Furthermore, plasma treatment on metal surface has also been investigated. Timko *et al* reported that plasma arcs can generate craters on the surface even in materials such as Cu.[42] Their experiment was carried out in an UHV chamber.[42] A direct current arc with 10 kV was generated between a Cu cathode and anode.[42] For the metal niobium, Upadhyay *et al* reported that surface modification of niobium can be altered by plasma by different experimental parameters.[43] Their set up was a capacitively coupled RF plasma.[43] The driven frequency was 13.56 MHz.[43] The operating pressure was about 20 $mTorr$.[43] They studied how driven-electrode diameter, pressure, RF power and gas concentration affected the etching rate of niobium.[43]

Above all, plasma has been utilized in a wide range of surface treatments. Researchers carried out experiments with different plasma parameters based on their different requirements. However, the common point among different publications is the key parameters for plasmas, such as pressure, flow rate, input power, gas composition, exposure time and sample location.

Plasma classification

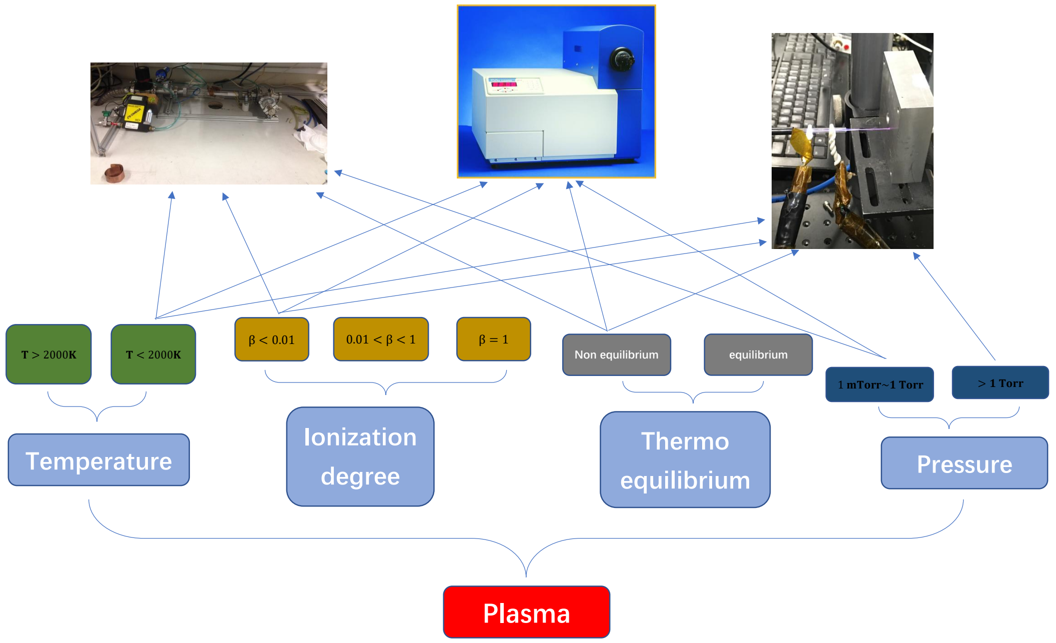

Figure 2.9: Classification of the three different plasma sources in our group. The left setup is the inductively-coupled plasma chamber. In the middle, it is the FISCHIONE 1020 plasma cleaner. The right setup is the inductively-coupled atmospheric plasma jet.

Fig. 2.9 classifies the three plasma sources used in this work. For the plasma chamber, the operating pressure is from 20 to 70 $mTorr$. For the commercial plasma cleaner, the operating pressure ranges from 40-50 $mTorr$. For the plasma jet, the operating pressure is atmospheric. All of them are non-equilibrium since they are all low temperature plasmas where electrons have higher energy than ions.

In Chapter 6, plasma treatments were conducted in the FISCHIONE 1020 plasma cleaner. It generates a standard radio frequency (RF) plasma with a 13.56 MHz oscillating field system coupled to a quartz and stainless steel chamber. The gas source is 25% oxygen and 75% argon mixture gas. Inside the plasma cleaner, the ion energy at the sample location is about 12 eV when the chamber pressure is 46 $mTorr$.[44]

Chapter 3

Transfer matrix method for electron transport

Transfer matrix method (TMM) is a common tool to deal with second-order differential equations. In a quantum system such as a quantum well and barrier, by solving the Schrödinger equation which is a typical second-order differential equation, electron transmission can be obtained. A typical quantum well (barrier) is a semiconductor superlattice (for example GaAs/$Ga_{1-x}Al_xAs$) which can be fabricated by the molecular beam epitaxy technique. In this Chapter, we are going to introduce the basic knowledge of the transfer matrix method. And we will apply the TMM to study the electron transport in oxygen-plasma-treated monolayer MoS_2 in Chapter 8. Moreover, in Chapter 10, we will discuss the application of TMM in valley electronics and spintronics.

3.1 Scattering matrix

Before introducing the TMM, we need to introduce the concept of the scattering matrix first, because the derivation of the transfer matrix is based on the scattering matrix. The scattering matrix describes the relation between incoming and outcoming waves of the system. The scattering matrix S is defined as[45]

$$
\begin{bmatrix} \psi_{zl}^{-} \\ \psi_{zr}^{+} \end{bmatrix} = S \begin{bmatrix} \psi_{zl}^{+} \\ \psi_{zr}^{-} \end{bmatrix} \tag{3.1}
$$

As shown in Fig. 3.1, the quantum well (barrier) is located in the middle. ψ stands for an electron wave function. Subscripts z mean that it is a one-dimensional problem and the wave propagates in the longitudinal direction z. Subscripts l and r clarify the region where electron wave functions are. Superscripts + and - stand for the moving directions of wave functions. For example, ψ_{zr}^{+} represents an electron wave function on the right side of the quantum well (barrier) moving to the right.

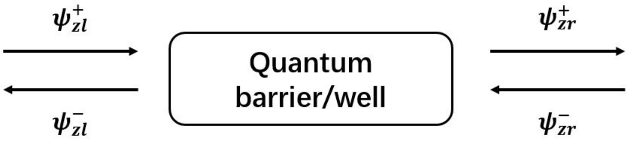

Figure 3.1: Illustration of transfer matrix method. In the middle is the quantum barrier/well. On the left and rights are wavefunctions entering and leaving the barrier/well region.

The next step is to determine the elements of the scattering matrix. Two conditions are applied in this step. The first condition is the conservation law of the current density, and the second is time-reversal symmetry. The current density $j(z)$ is commonly defined as,

$$
j(z) = \frac{\hbar i}{2m} \left[\psi(z) \frac{\partial \psi^{*}(z)}{\partial z} - \psi^{*}(z) \frac{\partial \psi(z)}{\partial z} \right] \tag{3.2}
$$

The expression for the current density of a plane wave is commonly defined as $j = (\hbar q/m)|\Psi|^2$. Inserting this into Eq 3.2, we obtain the current density in the left and right region.

$$
j_L = \frac{\hbar q}{m} \left(|\psi_{zl}^{+}|^2 - |\psi_{zl}^{-}|^2 \right) = \frac{\hbar q}{m} \left(|\psi_{zr}^{+}|^2 - |\psi_{zr}^{-}|^2 \right) = j_R \tag{3.3}
$$

Equation 3.3 can be written in a more compact way, $|\psi_{zl}^{+}|^2 + |\psi_{zr}^{-}|^2 = |\psi_{zl}^{-}|^2 + |\psi_{zr}^{+}|^2$. Now transforming it into vector notation, we have

$$
[\psi_{zl}^{-*} \psi_{zr}^{+*}] \begin{bmatrix} \psi_{zl}^{-} \\ \psi_{zr}^{+} \end{bmatrix} = [\psi_{zl}^{+*} \psi_{zr}^{-*}] \begin{bmatrix} \psi_{zl}^{+} \\ \psi_{zr}^{-} \end{bmatrix} \tag{3.4}
$$

Conjugating Eq 3.1, we obtain $[\psi_{zl}^{-*}\ \psi_{zr}^{+*}] = [\psi_{zl}^{+*}\ \psi_{zr}^{-*}]S^{\dagger}$. By inserting it and Eq 3.1 into Eq 3.4, we obtain an important property of scattering matrix from current density conservation,

$$SS^{\dagger} = 1 \tag{3.5}$$

It means the scattering matrix is unitary, namely $|det\ S| = 1$. We further apply time-reversal symmetry to the scattering matrix. If the system possesses time-reversal symmetry and ψ_z is the solution of Schrödinger equation, then its complex conjugate ψ_z^* is also a solution. Thus, after time reversal, the relation between incoming and outcoming waves becomes,

$$\begin{bmatrix} \psi_{zl}^{+*} \\ \psi_{zr}^{-*} \end{bmatrix} = S \begin{bmatrix} \psi_{zl}^{-*} \\ \psi_{zr}^{+*} \end{bmatrix} \tag{3.6}$$

Then complex conjugating Eq 3.1, we have,

$$\begin{bmatrix} \psi_{zl}^{-*} \\ \psi_{zr}^{+*} \end{bmatrix} = S^{*} \begin{bmatrix} \psi_{zl}^{+*} \\ \psi_{zr}^{-*} \end{bmatrix} \tag{3.7}$$

By inserting Eq 3.7 into Eq 3.6, we obtain another important property of the scattering matrix,

$$SS^{*} = 1 \tag{3.8}$$

The obtained properties in Eqs 3.5 and 3.8 tell us the scattering matrix is not only orthogonal but also symmetric.

3.2 Transfer matrix

Unlike the scattering matrix, the transfer matrix describes the relationship between wavefunctions from the left side and right side of the quantum well (barrier). The relation between wavefunctions can be described as[45]

$$\begin{bmatrix} \psi_{zr}^{+} \\ \psi_{zr}^{-} \end{bmatrix} = M \begin{bmatrix} \psi_{zl}^{+} \\ \psi_{zl}^{-} \end{bmatrix} \tag{3.9}$$

where M is the transfer matrix. Then we are going to apply current density conservation and time reversal to the transfer matrix M. We rewrite $|\psi_{zl}^{+}|^2 +$

$|\psi_{zr}^-|^2 = |\psi_{zl}^-|^2 + |\psi_{zr}^+|^2$ into the form $|\psi_{zl}^+|^2 - |\psi_{zl}^-|^2 = |\psi_{zr}^+|^2 - |\psi_{zr}^-|^2$, and express it in the vector notation,

$$[\psi_{zl}^{+*}\ \psi_{zl}^{-*}] \begin{bmatrix} 1 & 0 \\ 0 & -1 \end{bmatrix} \begin{bmatrix} \psi_{zl}^+ \\ \psi_{zl}^- \end{bmatrix} = [\psi_{zr}^{+*}\ \psi_{zr}^{-*}] \begin{bmatrix} 1 & 0 \\ 0 & -1 \end{bmatrix} \begin{bmatrix} \psi_{zr}^+ \\ \psi_{zr}^- \end{bmatrix} \tag{3.10}$$

We also need the conjugated expression of Eq 3.9, $[\psi_{zr}^{+*}\ \psi_{zr}^{-*}] = [\psi_{zl}^{+*}\ \psi_{zl}^{-*}]M^\dagger$. Inserting the conjugated expression into Eq 3.10, we obtain,

$$[\psi_{zl}^{+*}\ \psi_{zl}^{-*}] \begin{bmatrix} 1 & 0 \\ 0 & -1 \end{bmatrix} \begin{bmatrix} \psi_{zl}^+ \\ \psi_{zl}^- \end{bmatrix} = [\psi_{zl}^{+*}\ \psi_{zl}^{-*}]M^\dagger \begin{bmatrix} 1 & 0 \\ 0 & -1 \end{bmatrix} M \begin{bmatrix} \psi_{zl}^+ \\ \psi_{zl}^- \end{bmatrix} \tag{3.11}$$

This expression tells us the relation between transfer matrix M and its Hermitian conjugation $M^\dagger$,

$$M^\dagger \begin{bmatrix} 1 & 0 \\ 0 & -1 \end{bmatrix} M = \begin{bmatrix} 1 & 0 \\ 0 & -1 \end{bmatrix} \tag{3.12}$$

Moreover, time-reversal symmetry can also be applied to the transfer matrix. The process is similar as that of the scattering matrix. The transfer matrix of the time reversed system is,

$$\begin{bmatrix} 0 & 1 \\ 1 & 0 \end{bmatrix} \begin{bmatrix} \psi_{zr}^{+*} \\ \psi_{zr}^{-*} \end{bmatrix} = M \begin{bmatrix} 0 & 1 \\ 1 & 0 \end{bmatrix} \begin{bmatrix} \psi_{zl}^{+*} \\ \psi_{zl}^{-*} \end{bmatrix} \tag{3.13}$$

The complex conjugation of Eq 3.9 reads

$$\begin{bmatrix} \psi_{zr}^{+*} \\ \psi_{zr}^{-*} \end{bmatrix} = M^* \begin{bmatrix} \psi_{zl}^{+*} \\ \psi_{zl}^{-*} \end{bmatrix} \tag{3.14}$$

Then, inserting Eq 3.14 into Eq 3.13, we obtain,

$$\begin{bmatrix} 0 & 1 \\ 1 & 0 \end{bmatrix} M \begin{bmatrix} 0 & 1 \\ 1 & 0 \end{bmatrix} = M^* \tag{3.15}$$

Equation 3.15 is the property of transfer matrix when the time-reversal symmetry is applied. Then we need to study the relation between the transfer matrix and scattering matrix. It can be easily obtained by comparing the coefficients of Eqs 3.1 and 3.9 to give,

$$M = \begin{bmatrix} M_{11} & M_{12} \\ M_{12} & M_{11} \end{bmatrix} = \begin{bmatrix} S_{21} - \dfrac{S_{11}S_{22}}{S_{12}} & \dfrac{S_{22}}{S_{12}} \\ \dfrac{-S_{11}}{S_{12}} & \dfrac{1}{S_{12}} \end{bmatrix} \tag{3.16}$$

Now, let's go back to Fig. 3.1. Consider an electron approaching the quantum well (barrier) from the right, with no electrons coming from the left, we have $\psi_{zl}^{+} = 0$. Based on the definition of scattering matrix, we have $\psi_{zl}^{-} = S_{12}\psi_{zr}^{-}$ and $\psi_{zr}^{+} = S_{22}\psi_{zr}^{-}$. We call S_{12} the transmission amplitude t and S_{22} the reflection amplitude r. In the same way, we can consider electrons only coming from the left side of the system. We obtain $r' = S_{11}$ and $t' = S_{21}$. Thus the scattering matrix has the form,

$$S = \begin{bmatrix} r' & t \\ t' & r \end{bmatrix} \tag{3.17}$$

Then, using the relation between transfer and scattering matrix in Eq 3.16, we have

$$M = \begin{bmatrix} t' - rt^{-1}r' & rt^{-1} \\ -t^{-1}r' & t^{-1} \end{bmatrix} \tag{3.18}$$

Thus, it can be seen that the transmission T is

$$T = \frac{1}{|M_{22}|} = \frac{1}{1 + |M_{12}|^2} \tag{3.19}$$

The above is the basic derivation of TMM. Once it is applied to a real quantum system (such as semiconductor superlattices or nonmagnetic/ferromagnetic heterostructures), the above expressions are still correct. However, the Hamiltonians of the particle are different and the corresponding Schrödinger equations need to be solved, which depends on the properties of the system. In this section, we only introduce the one-dimensional TMM, where movement of the electron is contrained along the longitudinal direction (z axis). In Chapter 8, we are going to discuss the electron transport in a 2D oxygen-plasma-treated MoS_2 nanosheet. We will show the derivation of 2D TMM where the transmission is coupled with two degrees of freedom (k_x and k_y).

3.3 Resonant tunneling

An important physics phenomenon deduced from the TMM is the resonant tunneling effect. Resonant tunneling is a quantum-mechanical phenomenon caused by energy-dependent transmission. In Fig. 3.1, the solution to the Schrödinger equation reads,

$$\Psi(x) = \begin{cases} \Psi_L(x) = Ae^{ikx} + Be^{-ikx}, \ left\ region \\ \Psi_i(x) = Fe^{ik'x} + Ge^{-ik'x}, \ barrier/well \\ \Psi_R(x) = Ce^{ikx} + De^{-ikx}, \ right\ region \end{cases} \tag{3.20}$$

where k and k' are the wave vectors in regions without/with a potential. They are defined as $k = \sqrt{2mE}/\hbar$ and $k' = \sqrt{2m(E - V_0)}/\hbar$. By applying the TMM, the elements of transfer matrix can be obtained, yielding

$$M_{11} = cos2k'a + \frac{i}{2}(\frac{k}{k'} + \frac{k'}{k})sin(2k'a) \tag{3.21}$$

$$M_{12} = \frac{i}{2}(\frac{k}{k'} - \frac{k'}{k})sin(2k'a) \tag{3.22}$$

$$M_{22} = cos2k'a - \frac{i}{2}(\frac{k}{k'} + \frac{k'}{k})sin(2k'a) \tag{3.23}$$

$$M_{21} = -\frac{i}{2}(\frac{k}{k'} - \frac{k'}{k})sin(2k'a) \tag{3.24}$$

Here, a is the half length of the quantum barrier/well. Thus, the transmission T can be obtained, and is given by

$$T = \frac{1}{1 + \frac{1}{4}\left(\frac{k}{k'} - \frac{k'}{k}\right) sin^2(2k'a)} \tag{3.25}$$

The visualization of Eq. 3.25 is shown in Fig. 3.2. In order to study the evolution of transmission with respect to the ratio of incident electron energy to potential, Fig. 3.2 is plotted in dimensionless units. Its x axis is defined by the ratio of incident electron energy to the magnitude of the potential. When the transmission reaches the value of 1, it indicates that resonant tunnelling happens. Resonant tunnelling is the origin of negative-resistance effect, which is the foundation of resonant tunnelling diodes.[46] Another important application of the transfer matrix method and resonant tunnelling is to quantum well electro-absorption modulators, which have been widely used in high-speed optical communication.[47]

Moreover, the physics interpretation of resonant tunnelling is that the length of the quantum barrier/well is an integer multiple of the half wavelength of the electron wave function inside the barrier. The mathematics interpretation of it is that both magnitude of the potential and barrier length are small enough, leading the second term in the denominator of Eq. 3.25 to be negligible.

Fig. 3.2 can also be found in Ref. [45]. The homemade MATLAB code to generate Fig. 3.2 is shown in Appendix B.

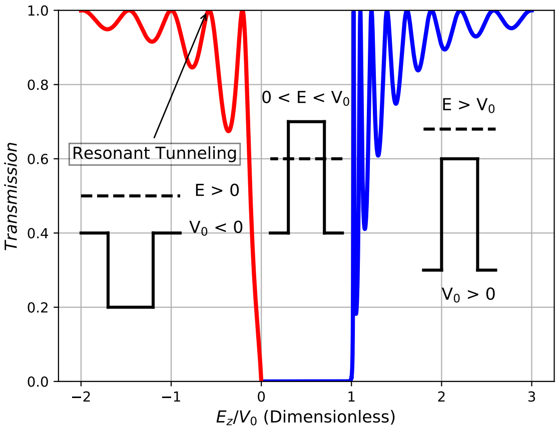

Figure 3.2: For the case of a single barrier/well, the relation between transmission and incident electron energy is shown. MATLAB code to generate the figure is in Appendix B.

Chapter 4

Density functional theory and self-consistent field algorithm

In modern condensed matter physics, density functional theory (DFT) is the most powerful and flexible tool to simulate the electronic properties of materials. Aside from DFT, tight-binding model and $\mathbf{k} \cdot \mathbf{p}$ method are also popular options to analyse the electronic properties of the material. Thus, we firstly need to answer the question why we choose DFT to study the oxygen-plasma-treated $\mathrm{MoS_2}$ rather than these other two methods.

In the tight-binding model, the basis consists of the Fourier transform of atomic orbitals. The nonzero Hamiltonian matrix contains Slater-Koster coefficients.[48] The Slater-Koster coefficients originate from molecular orbital hybridization theory, where each atomic orbital has a specific spatial orientation leading to non-orthogonality between atomic orbitals from different atoms in the molecule. One usually fits the band structure calculated by DFT to determine the Slater-Koster coefficients. Thus, tight-binding theory is also called semi-empirical tight-binding theory. The drawback of the tight-binding model is the difficulty to calculate a super cell. It is very difficult to determine how atomic orbitals hybridize to form molecular orbitals in the presence of a vacancy, which causes a difficulty in determining the Slater-Koster coefficients.

$\mathbf{k} \cdot \mathbf{p}$ theory is mainly based on the Luttinger-Kohn model.[49] $\mathbf{k} \cdot \mathbf{p}$ theory is a powerful tool to study the band structure at high symmetry points. Andor *et al* successfully applied $\mathbf{k} \cdot \mathbf{p}$ theory to 2D TMD systems to reproduce the results calculated by DFT and tight-binding theory.[22] It is clear that the disadvantage of $\mathbf{k}\cdot\mathbf{p}$ theory is the lack of global view of the materials band structure.

Thus, due to the feasibility of studying defective systems and super cells, we apply DFT to study the electronic properties of pristine and oxygen-plasma-treated monolayer MoS_2. The results of calculation will be discussed in Chapter 7.

4.1 Hartree-Fock formalism

The Hartree-Fock (HF) formalism was firstly proposed by D. R. Hartree in 1927, which is the prototype self-consistent field algorithm.[50] It is also a pioneering work applying variational principle in many-body quantum mechanics. I would like to introduce HF formalism at first to show my respect to the pioneers although we don't solve HF equations in this work.

Firstly, I would like to emphasize that the algorithm used in this work is under the framework of Kohn-Sham (KS) DFT rather than Hatree-Fock (HF) DFT. KS DFT considers correlation effects and is much easier to solve as it only involve local potentials, while the exchange interaction in HF involves a convolution with a non-local kernel.

The many-body Hamiltonian in the HF theory is

$$H = \sum_{i=1}^{N}\left[-\frac{\hbar^2}{2m}\nabla_i^2 + u(x_i)\right] + \frac{1}{2}\sum_{i\neq j}^{N} v(x_i, x_i) \tag{4.1}$$

where $u(x_i)$ is the interaction between a nuclei and its electrons,

$$u(x_i) = \sum_{\alpha}\frac{Z_\alpha e}{|\mathbf{r}_i - \mathbf{R}_\alpha|} \tag{4.2}$$

and where $v(x_i, x_{j2})$ is the electron-electron interaction, which is also called Hatree term,

$$v(x_i, x_j) = \frac{e^2}{|\mathbf{r}_i - \mathbf{r}_j|} \tag{4.3}$$

We construct the total energy as the expectation value of the Hamiltonian, $<\Phi|H|\Phi>$. Here Φ is the wave-function of HF theory. It is defined as the Slater determinant, which is a common expression of a many-body wave function,

$$\Phi(x_1, ..., x_N) = \frac{1}{\sqrt{N!}} \begin{vmatrix} \phi_1(x_1) & \dots & \phi_1(x_N) \\ \vdots & & \vdots \\ \phi_N(x_1) & \dots & \phi_N(x_N) \end{vmatrix} \tag{4.4}$$

By inserting Eq 4.4 into the Hamiltonian in Eq 4.1, we obtain,

$$\begin{aligned} < \Phi|H|\Phi > = \frac{1}{N!} \sum_{\mu\nu} sign(\mu) sign(\nu) \int dx_1 \dots x_N \phi^*_{\mu 1}(x_1) \dots \phi^*_{\mu N}(x_N) \\ \left\{ \sum_{i=1}^{N} \left[-\frac{\hbar^2}{2m} \nabla_i^2 + u(x_i) \right] + \frac{1}{2} \sum_{i \neq j}^{N} v(x_i, x_i) \right\} \phi_{\nu 1}(x_1) \dots \phi_{\nu N}(x_N) \end{aligned} \tag{4.5}$$

By applying Lagrangian-multiplier method and the variational principle with the constrain $\sum_{i=1}^{N} \int dy \phi_i(y) \phi_i^*(y) = N$ to Eq 4.5, we have,

$$\frac{\delta}{\delta \phi^*_\alpha(x)} \left[< \Phi|H|\Phi > - \sum_{i=1}^{N} \epsilon_i \int dy \phi_i(y) \phi_i^*(y) \right] = 0 \tag{4.6}$$

By inserting Eq 4.5 into Eq 4.6, we obtain the Hatree-Fock equation,

$$\begin{aligned} \left[-\frac{\hbar^2}{2m} \nabla^2 + u(x) + \sum_{j \neq \alpha} \int dy v(x, y) \phi_j^*(y) \phi_j(y) \right] \phi_\alpha(x) - \\ \sum_{j \neq \alpha} \int dy v(x, y) \phi_j^*(y) \phi_j(x) \phi_\alpha(y) = \epsilon_\alpha \phi_\alpha(x) \end{aligned} \tag{4.7}$$

The final step is to organize Eq 4.7 into a more compact expression by dropping the $j \neq \alpha$ terms in the sums, whereupon we obtain

$$\left[-\frac{\hbar^2}{2m} \nabla^2 + u(x) + \int \frac{\rho(x') dx'}{|\mathbf{r} - \mathbf{r}'|} \right] \phi_\alpha(x) - \int \frac{\rho(x, x') \phi_\alpha(x')}{|\mathbf{r} - \mathbf{r}'|} dx' = \epsilon_\alpha \phi_\alpha(x) \tag{4.8}$$

In Eq 4.8, we can see that on the left side of the Schrödinger equation, the electron density $\rho(x)$ or $\rho(x')$ appears. And the electron density is defined as $\rho(x) = \sum_{i=1}^{N} |\phi_i(x)|^2$ in the coordinate representation. Thus, we can see that the self-consistent method can be applied to Eq 4.8, because the electron density is determined by the calculated wave functions. And after obtaining the electron density, one has to insert the electron density back to the new Schrödinger equation again to calculate a new wave function. This repeating process is the idea of a self-consistent field (SCF) calculation. The HF method sets up the foundation of SCF calculation in condensed matter physics. Later, we are going to introduce Kohn-Sham theory, which is also based on the SCF theory.

4.2 Hohenberg-Kohn Theorem

The Hohenberg-Kohn (HK) theorem is the heart of DFT. However, before introducing HK theorem, I have to introduce Thomas-Fermi (TF) model, which is an important pioneer work in closely related to the HK theorem.

The Thomas-Fermi model was proposed by Llewellyn Thomas and Enrico Fermi in 1927. The idea of the TF model is in expressing the Hamiltonian in terms of electron density. Mathematically speaking, the Hamiltonian is a functional of electron density. Here we only show the expression of TF model rather than deriving it, since it can be found in any condensed matter physics textbook.[50] The TF Hamiltonian has the form

$$E_{total} = C_k \int [\rho(x)]^{5/3} dx + e \int \rho(x) V_{ext}(x) dx + \frac{1}{2} e^2 \int \frac{\rho(x)\rho(x')}{|x - x'|} dx dx' \quad (4.9)$$

where C_k is $\frac{3h^2}{10m_e}(\frac{3}{8\pi})^{2/3}$, and h is Plank's constant. The first term is kinetic term. The second and third terms are electron potential in external field and electron-electron interaction. It is clear that in the TF model the Hamiltonian is a functional of the electron density $\rho(x)$.

Based on the idea of the TF model, it is easier to understand HK theorem. The HK theorem claims that the ground-state energy is not only a functional of the electron density, but also is minimized at the ground-state electron density, such that

$$E_{GS} = E_{GS}[\rho(x)] =< \Phi(x)|\hat{H}|\Phi(x) > \quad (4.10)$$

The HK theorem also claims that for any observable $\hat{O}$ in the ground state, its expectation value is a functional of electron density $\rho(x)$, or more precisely

$$O_{GS} = O_{GS}[\rho(x)] =< \Phi(x)|\hat{O}|\Phi(x) > \quad (4.11)$$

The HK theorem was proposed by P. Hohenberg and W. Kohn in 1964.[51] It successfully builds the bridge between physical observables and the electron density.

4.3 The Kohn-Sham equation

One year after the paper proposing HK theorem published, W. Kohn and L. J. Sham published another significant paper to construct the Kohn-Sham (KS) equation, and to claim that the KS equation can be solved self-consistently like HF equations.[52] The KS equation has the form, in atomic units,[52]

$$\left[-\frac{1}{2}\nabla^2 + \int dx' \frac{\rho(x')}{|x-x'|} + V(x) + \epsilon_{xc}(x)\right] \phi_i(x) = \epsilon_i \phi_i(x) \tag{4.12}$$

where the first to the fourth terms are the kinetic energy, electron-electron interaction, external potential and exchange-correlation potential. The KS equation also has a more compact form

$$\left[-\frac{\hbar^2}{2m}\nabla^2 + V_{eff}(x)\right] \phi_i(x) = \epsilon_i \phi_i(x) \tag{4.13}$$

In the next section, we are going to show how to numerically solve the KS equations.

4.4 Practical implementation of DFT

In Quantum Espresso, we are going to solve the KS equations shown in Eqs 4.12 and 4.13. To solve the KS equations, a basis set should be chosen properly. A plane-wave basis and atom-centered basis are two popular options. However, the one that should be chosen depends on the situation. For example, in non-periodic systems like macromolecules or clusters, one prefers an atom-centered basis. Here, the atom-centered basis refers to the *k-space* Bloch sums, which are the building blocks for the Slater-Koster coefficients in the tight-binding model.[48] The Bloch sums has the form

$$|\phi_j; k >= \frac{1}{\sqrt{N}} \sum_j |\phi_j > e^{i\mathbf{k}\cdot\mathbf{R}} \tag{4.14}$$

where $|\phi_j >$ refers to coordination-representation atom-centered wave functions which are the combinations of spherical harmonics, such as s and p atomic orbitals, and j stands for unit cells. Mathematically speaking, the Bloch sums are the discrete Fourier transform of the real-space atomic orbitals.

In our case, the research object is 2D materials with periodic lattices. In periodic systems with Born-von Karman boundary conditions applied, a plane-wave basis is a common choice. It has three significant advantages. The first is the convenience of accuracy evaluation. The accuracy of the simulation depends on the plane-wave cutoff determined by the largest wave vector. The second is simple manipulation in terms of operators like derivatives. The third is that momentum and kinetic energy operators are diagonal in the plane-wave basis, because plane waves are the eigenvectors of translation operator, namely the momentum operator.

However, a plane-wave basis also has two main limitations. The first limit is the rapid growth of the size of the plane-wave basis with the increasing of the number of atoms in the system, resulting in an excessive time cost when simulating supercells. The second is the difficulty of describing the real nuclei potential analytically, because, near a nuclei, the electric potential changes rapidly, which requires a large amount of plane waves and slows down the speed of convergence. Therefore, pseudopotential method is introduced to overcome the above difficulties.

Pseudopotential

A pseudopotential (PP) can be understood as an effective potential considering contributions from both the nuclear and core-electron potential. The aim of introducing a PP is to make the atomic potential "soft" (the most popular PP is called an ultrasoft pseudopotential), mathematically resulting in the lower cut-off energy of the plane-wave basis compared with the real potential.[50]

In the pseudopotential method, electron wave functions on an atom can be classified into core states or valence states. Because spherical harmonics are the solutions to the Schrödinger equation in a centripetal force field, valence wave functions are orthogonal to core-state wave functions. Mathematically, valence-electron wave functions in coordinate representation have nodes in the atomic region to ensure the orthogonality of the basis. Moreover, it can be concluded that they require a higher cut-off energy of the plane waves when there are more nodes in the valence electron wave functions.

Precisely speaking, the pseudopotential is a projection operator.[50] To see this, we firstly define a valence electron wave function $H|\phi_v >= \epsilon_v|\phi_v >$ and core electron wave function $H|\phi_c >= \epsilon_c|\phi_c >$. They satisfy the orthogonal condition $< \phi_c|\phi_v >= 0$. We further construct the pseudofunction as $|\phi_v^{PS} >= |\phi_v > + \sum a_c|\phi_c >$.[50] Then multiply both sides by $< \phi_c|$ to obtain,

$$|\phi_v^{PS} >= |\phi_v > + \sum_c |\phi_c >< \phi_c|\phi_v^{PS} > \tag{4.15}$$

Then, we use the operator $(H - \epsilon_v)$ to act on it, we can obtain,

$$\left[H - \sum_c (\epsilon_c - \epsilon_v)|\phi_c >< \phi_c| \right] |\phi_v^{PS} >= \epsilon_v|\phi_v^{PS} > \tag{4.16}$$

Equation 4.16 is an equivalent Schrödinger equation for valence electrons. We define the second term $\sum(\epsilon_c - \epsilon_v)|\phi_c >< \phi_c|$ in the bracket as $\widetilde{V}$. It is clear that $\widetilde{V}$ is a projection operator. Then, we replace the $V(x)$ in Eq. 4.12 with $\widetilde{V}$ to obtain the Phillips Kleinman pseudopotential,[53]

$$V^{PK}(x) \equiv \widetilde{V}(x) + u(x) + \frac{e^2}{2} \int dx' \frac{\rho(x)\rho(x')}{|x - x'|} + \epsilon_{xc}(x) \tag{4.17}$$

The most important point should be emphasized is that although the pseudopotential is pseudo its eigenvalues are real. “Real” means that the eigenvalues are same as the eigenvalues of real valence electrons.[50]

So far, we have introduced the pseudopotentials. Next, we show the flow chart of the self-consistent field DFT algorithm in Fig. 4.1. It shows a standard algorithm of modern DFT calculations. In Quantum Espresso, the core algorithm of SCF calculation is same as Fig. 4.1.

In this Chapter, we have introduced the basic knowledge of density functional theory. We will apply DFT to calculate the electronic and magnetic properties of oxygen-plasma-treated monolayer MoS_2 in Chapter 7.

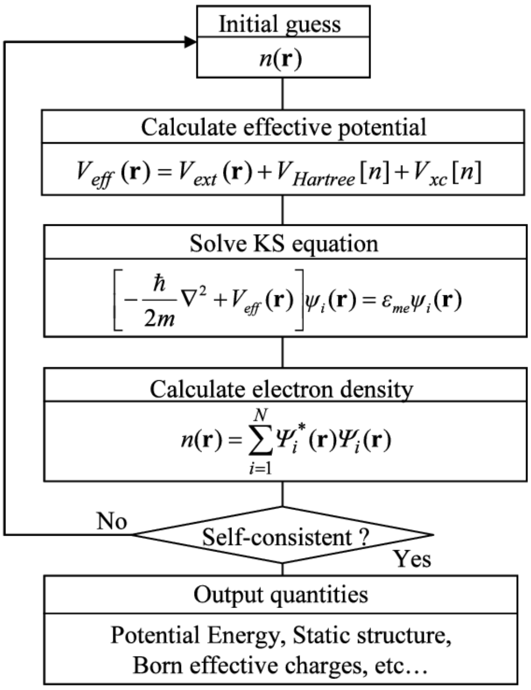

Figure 4.1: The flow chart of the self-consistent field DFT algorithm. The algorithm utilizes SCF calculation to solve KS equations. Graphic reproduced from [54] and copyright hold by Nakamachi *et al.*

Chapter 5

Experimental method

In this Chapter, we are going to firstly introduce the fabrication technique used to obtain 2D MoS_2 field-effect transistors. Then, we introduce the surface characterization techniques including atomic force microscopy, Raman microscopy and photoluminescene microscopy. Finally, we introduce the setup of our electrical measurements.

5.1 Fabrication of 2D MoS_2 FETs

In this work, MoS_2 flakes are obtained by mechanical exfoliation and chemical vapour deposition (CVD). We only introduce mechanical exfoliation technique in this Chapter, because CVD samples were provided by Niall McEvoy's group at Trinity College Dublin, and I don't have any training on the chemical vapour deposition technique.

5.1.1 Micromechanical exfoliation

The micromechanical exfoliation technique was first used by Noroselov *et. al* to obtain graphene.[3] The principle of micromechanical exfoliation is to overcome the weak interlayer van der Waals' interaction to thin the bulk material into thin flakes. Because molybdenum disulfide is a layered material with van-der-Waals interlayer force, the micromechanical exfoliation technique can be applied to isolate 2D MoS_2 from the bulk material.

Shown in Fig. 5.1 (a) is the first step preparing MoS_2 bulk material and scotch tape. Then, we choose a small piece of MoS_2 crystal and put it in the middle of scotch tape (Fig. 5.1 (b)). Then, we fold the tape to let the clean part of the tape adhere to the material and unfold the tape slowly. As shown in Fig. 5.1 (d), by doing the folding and unfolding process for about fifteen times, the bulk material will be uniformly exfoliated on the tape.

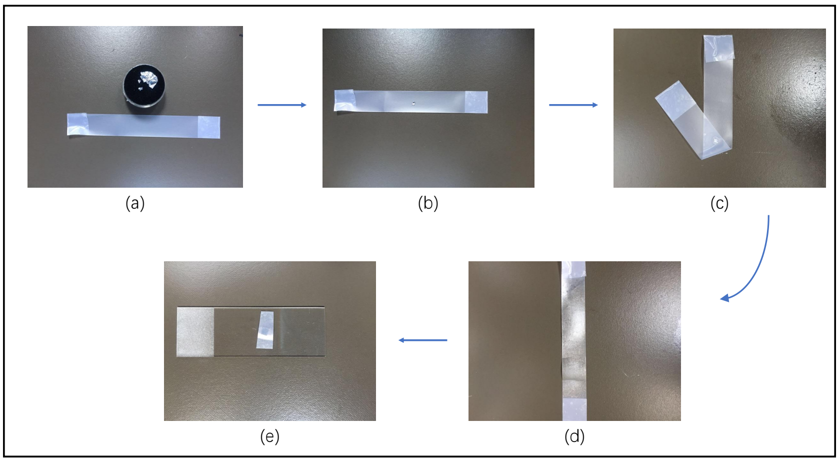

Figure 5.1: The process of the micromechanical exfoliation method. In (a), the material in silver color is MoS_2 bulk and the strip is one piece of scotch tape. (b) One small piece of bulk MoS_2 (area : 1 cm × 1 cm) is place in the center of the scotch tape. (c) and (d) The scotch tape is folded and unfolded in order to peel off the bulk MoS_2 using the viscosity of the rest part of the tape. (e) After several times repeating (c) and (d), we use scissors to cut a region from the tape, where the MoS_2 flakes uniformly distributed, and press it onto a silicon substrate.

The next step is to transfer flakes onto a certain substrate. In our case, the substrate is a p-doped silicon wafer with 285 nm thermally grown SiO_2. Substrates were cleaned with acetone and isopropyl alcohol (IPA). We cut one part of the tape and pressed it onto the cleaned substrate (Fig. 5.1 (e)), then peeled off the tape slowly. Thin flakes were obtained (Fig. 5.2 (a) and (b)).

The thickness of a flake can be identified under an optical microscope by calculating its contrast (C),

$$C = \frac{I_S - I_F}{I_S} \times 100\% \tag{5.1}$$

where I_S is the average red green blue (RGB) intensity value of the SiO_2 substrate, and I_F is the RGB intensity of the flake. As can be seen in Fig. 5.2 (c) and (d), by calculating the contrast value and comparing it with an established contrast table, the number of layers of a MoS_2 flake can be obtained.[55] Figure 5.2 shows the optical image and contrast of a typical bilayer MoS_2 flake on a 285 nm SiO_2 substrate. The reason that contrast evaluation can be used to tell the number of layers of a MoS_2 flake is based on the principle of thin-film interference. The optical path difference (OPD) between light reflected by the upper surface and lower surface of the flake determines the intensity of light received by the camera. Different OPDs caused by different numbers of layers of flakes results in the different contrasts that one observes under an optical microscope.

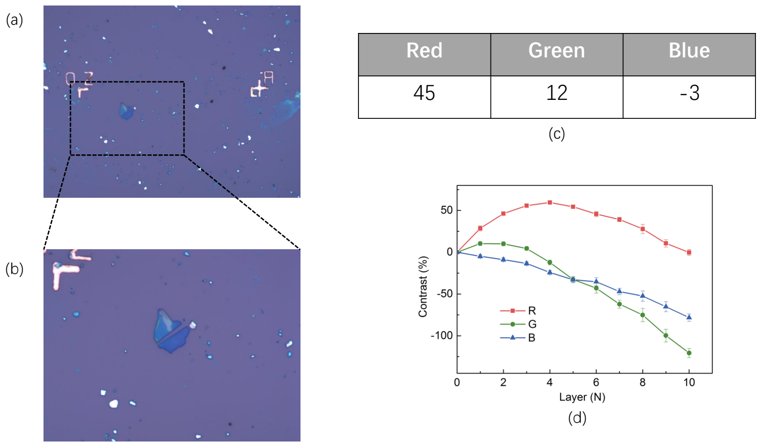

Red	Green	Blue
45	12	-3

Figure 5.2: (a) and (b) are optical images of an exfoliated bilayer MoS_2 flake on 285 nm SiO_2 under 20 and 50 magnification, respectively. (c) is the calculated RGB intensity of the flake. (d) is the contrast table for MoS_2 flakes on a 285 nm SiO_2 substrate.

5.1.2 Electron beam lithography

After obtaining MoS_2 flakes from the above mechanical exfoliation technique, we design patterns on the flake by electron beam lithography (EBL). Patterns refer to the areas where metal will be deposited in order to fabricate electrodes.

Patterns are designed in the software *Draftsight* and *Raith* shown in Fig. 5.3.

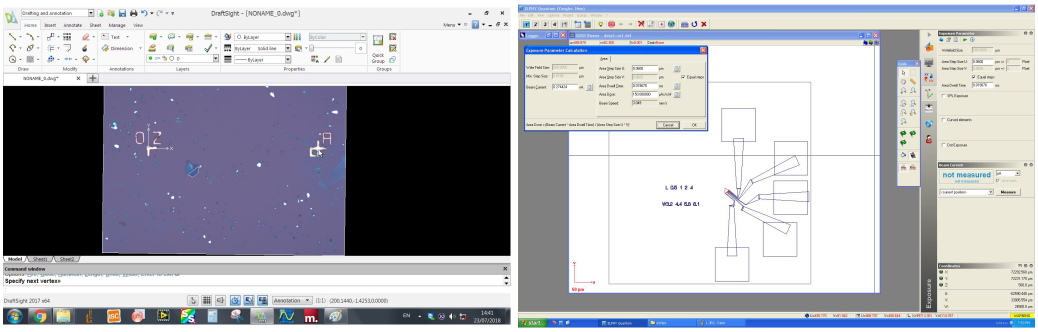

(a) (b)

Figure 5.3: (a) is the screenshot of software *Draftsight*. It shows the same flake as shown in Fig. 5.2. The file is exported as *.dxf* format for further processing. (b) is the screenshot of the software *Raith*, showing the pattern of electrodes. The input file of *Raith* is the exported *.dxf* file from *Draftsight*.

After drawing patterns by using the software shown in Fig. 5.3, we do spin coating to cover the flake with photoresist. EBL utilizes an electron beam to irradiate areas (designed patterns shown in Fig. 5.3) coved by photoresist in order to produce custom patterns. Areas irradiated by e-beams can be removed by developer, leaving the patterns made by unirradiated areas. The photoresist used in this work is polymethyl methacrylate (PMMA) A3 950k. Here A3 means that the PMMA is formulated in anisole solvent with mass concentration 3%, and 950k means that the molecular weight (MW) of the PMMA is 950,000 g/mol. Our developer is methyl isobutyl ketone:isopropyl alcohol (1:3), and the developing duration is 60 s.

Table 5.1: Recipe for spin coating. Step 1 is to accelerate the stage and step 2 is to spread out the PMMA uniformly.

	time(s)	Ramp(rpm/s)	Turn(rpm)
step 1	5	500	1000
step 2	45	3000	3000

Table.5.1 shows the recipe for the spin coating, with a 5-second acceleration process and 45-second uniform speed (3000 rpm/s) spinning. After spin coating, chips were transfered onto a hot plate to bake for 3 mins at 180 ^0C in order to remove the solvent. According to the technique report provided by Micro Chem company,[56] the thickness of the PMMA film is about 200 nm.

After spin coating, chips were loaded into a scanning electron microscope (Zeiss Supra) chamber to proceed EBL. During the EBL session, the gun voltage was set at 20 kV, the aperture size is 30 μm and the work distance is 5.5 mm. Since we use PMMA A3 950k, the optimal e-beam area dose is 200 $\mu As/cm^2$. The expression of dose is,

$$D_e = \frac{I_e t}{U \times V} \tag{5.2}$$

where I_e is the beam current, which can be measured through the Faraday hole on the stage. The Faraday hole is shown in Fig. 5.4. Here, t is the dwell time of the beam at each area unit, $U \times V$ is the size of the area unit.

In Fig. 5.4, the first image in the third row shows patterns made by above process based on the flake in Fig. 5.2. The green area is PMMA (photoresist) and the pattern area is in dark blue which is the original color of the 285 nm SiO_2 substrate. The depth of patterns is equal to the thickness of the PMMA with a value 200 nm. Ti (10 nm) / Au (40 nm) contacts were deposited into the pattern area using an e-beam evaporation tool, followed by lift off in acetone for 8 hours at room temperature. The fabricated MoS_2 FET and a SEM image are also shown in Fig. 5.4.

Figure 5.4 is the summary of the whole device fabrication process.

Figure 5.4: Flow chart of a MoS_2 FET fabrication process. The first row shows mechanical exfoliation, spin coat and baking processes. The second row shows the setup of the SEM and EBL system. In the third row, the first image demonstrates patterns made by EBL on the flake shown in Fig. 5.2, followed by a image showing Au electrodes made by film deposition in the corresponding patterned areas. The third image is a SEM image of fabricated Au electrodes. *The author has finished training on the SEM and has been authorised to use the SEM and EBL system.*

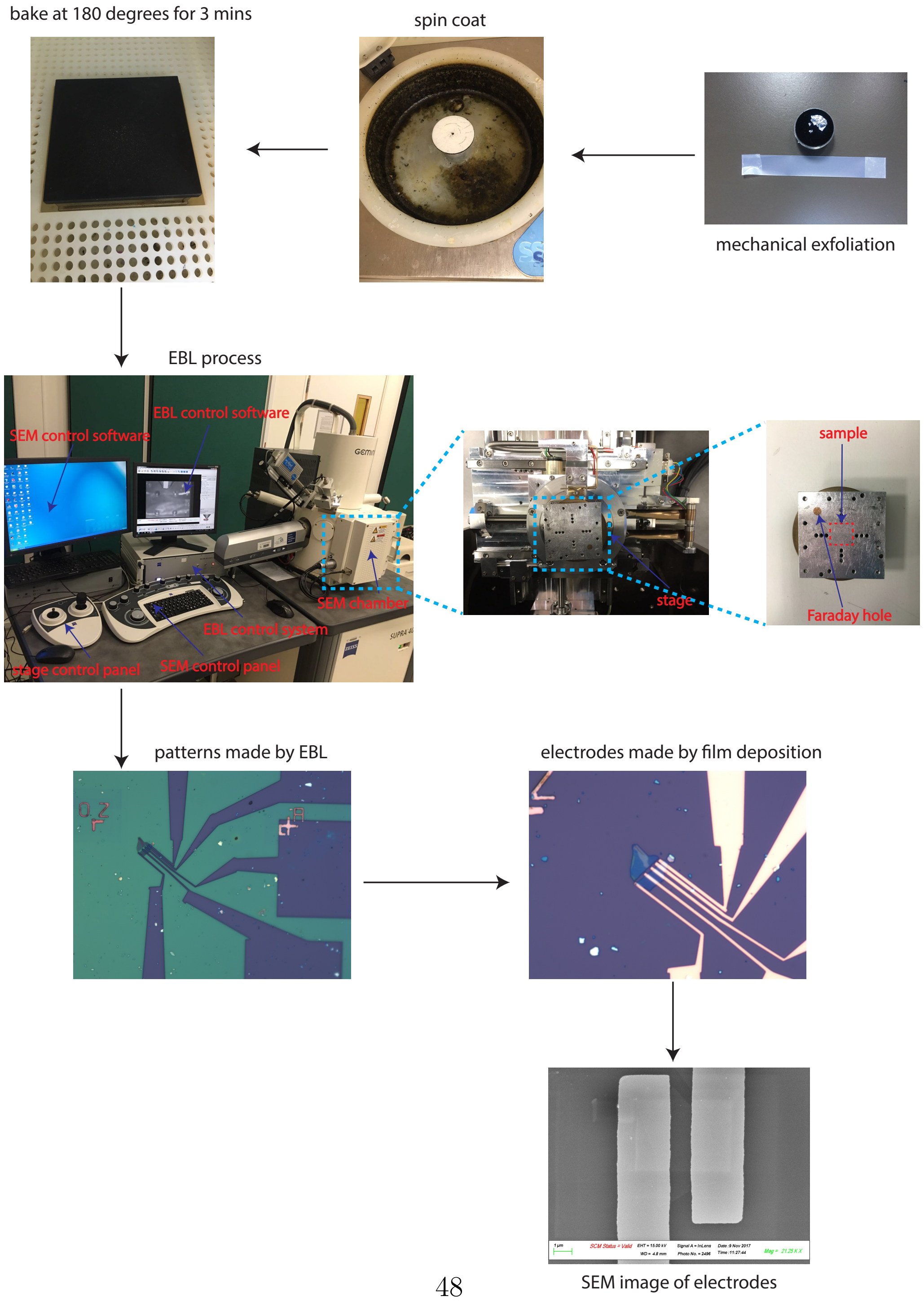

5.2 Device characterization and evaluation

In this section, we are going to introduce how we characterize and evaluate field-effect transistors. Surface characterization techniques used in this work include atomic force microscopy (AFM), Raman and PL spectroscopy. Electronics evaluation is based on a three-terminal source meter in which two terminals are connected with source and drain electrodes and the third terminal acts as back gate. The above techniques will be applied to analyse surface morphology and evaluate electronic performance of devices before and after oxygen-plasma treatment. Corresponding experimental results will be provided in the next Chapter.

5.2.1 Atomic force microscopy

In this work, the model of atomic force microscope used is the Oxford Asylum MFP-3D.

Atomic force microscopy (AFM) utilizes the weak interaction between the surface of the material and the force sensor to study the surface topography of the sample. The detector system of an AFM consists of a cantilever, a tip and photodetectors. The tip is mounted at one end of the cantilever. Another end of the cantilever is connected with a vibration system. A laser is located over the cantilever and it emits a beam onto the backside of the cantilever which will be collected by photodectors. Data collected by photodetectors can reflect the changes of surface topography. During the mapping, the distance between the sample and tip is controlled around one nanometer by a feedback system, since a larger distance will lose information and a shorter distance will damage the sample. In our case, the material of the tip is silicon. And the calibrated vibration frequency of the tip is 140 kHz.

Figure 5.5 shows the setup of Oxford Asylum MFP-3D AFM instrument. MoS_2 samples are mounted at the sample stage shown in (a). (b) shows the MFP-3D head. The MFP-3D head is the most important part of the system, because it integrates the force sensor, mechanical adjustment, piezo electronic system and sensitive laser system together. In (c), the cantilever holder is shown. (d) highlights the cantilever holder with an illustration of each component.

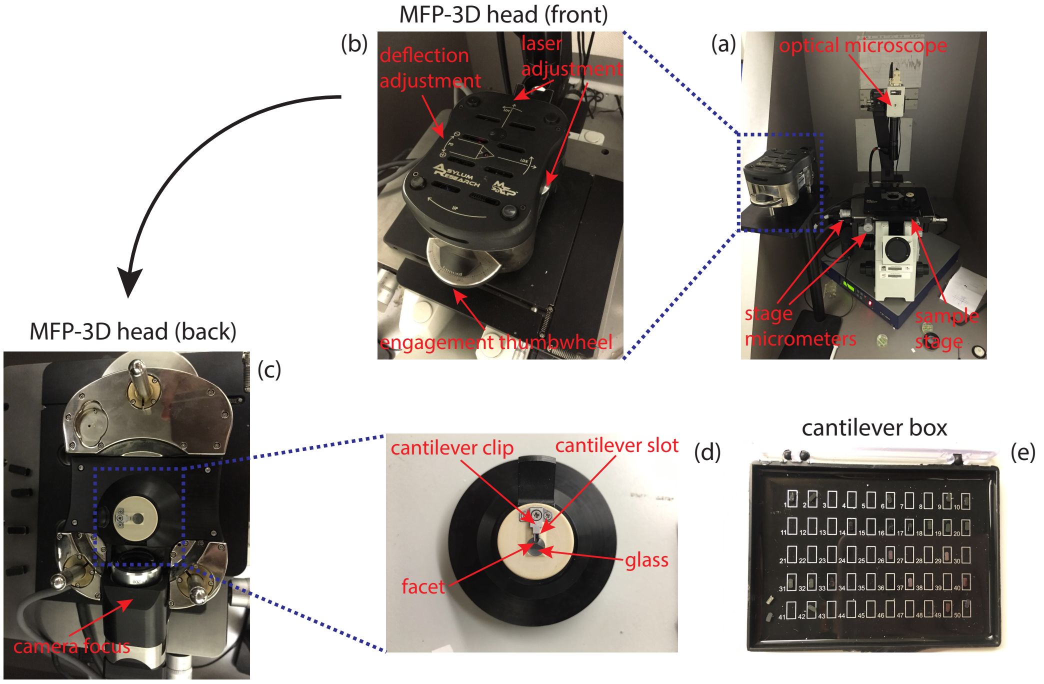

Figure 5.5: Images of the Oxford Asylum MFP-3D AFM system. (a) shows a global view the the AFM instrument. (b) is the front view of the MFP-3D head. (c) is the back view of the MFP-3D head. (d) illustrates the components of the cantilever holder. (e) is the cantilever box. *The author has finished training on the AFM and has been authorised to use the system.*

5.2.2 Raman and PL spectroscopy

Raman and photoluminescene spectra are acquired using a WITec Alpha 300 R confocal Raman microscope with an excitation wavelength of 532 nm. Raman spectra are acquired using a spectral grating with 1800 lines/mm, and a lower resolution grating 600 lines/mm is used for detecting photoluminescene. A low laser power ($<100\ \mu W$) is used to minimize laser-induced damage or heating of the sample.

Both Raman and photoluminescence (PL) spectroscopy are based on a laser and spectrometer. Raman spectra is based on Raman scattering effect discovered by the Indian scientist C. V. Raman.[57] Molecules can absorb energy from an incoming laser beam and transit into a higher energy state, a so-called virtual state. Then, it will transit back to a lower energy state again by emitting photons. The emitted beam may have the same frequency as the incoming beam. If they are equal, the spectra are called Rayleigh spectra. If not, the spectra are called Raman spectra. In the case of PL, an electron absorbs the energy from the incoming beam and transits onto the conduction band with a hole left on the valence band. Then the electron and the hole will recombine to emit a photon. The photon energy is equal to the value of the band gap. In monolayer MoS_2, the band gap is 1.84 eV, corresponding to a wave length of 676 nm. That's the reason that, in the study of photoresponsivity of monolayer MoS_2 FET in the next Chapter, the chosen wavelengths of laser are 488 and 632 nm, which have higher energy than the band gap of monolayer MoS_2.

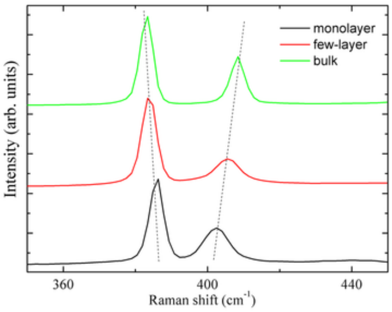

Figure 5.6: Characteristic peaks for bulk, few-layer and monolayer MoS_2. For monolayer MoS_2, E^1_{2g} and A_{1g} peaks are located at 383 cm^{-1} and 407 cm^{-1}.

The characteristic Raman peaks in monolayer MoS_2 are E^1_{2g} at 383 cm^{-1} and A_{1g} at 407 cm^{-1}. E^1_{2g} is caused by in-plane motion of Mo and S atoms moving against each other. A_{1g} originates from out-of-plane motion of S atoms. In Fig. 5.6, with thickness decreasing, the distance between two peaks shows a quenching effect. This phenomenon can be attributed to an increase of the dielectric screening which reduces the long-range Coulomb interaction between the effective charges and thus reduces the overall restoring force on the atoms.[58]

5.2.3 Electrical measurement

Figure 5.7 demonstrates the electrical measurement setup. In our experiment, the model of the probe station is miBoT^{TM} platforms. For each probe, it can move in four freedoms, including X, Y, Z direction and self rotation with motion resolution at the micro-meter scale. The material of the tip is Tungsten and the resistance between the tip and the cable is 3.5 Ω. The probe system can work in both ambient and vacuum conditions. There are four channels on the probe station. In this project, we use two of them for source and drain terminals, and another channel for the back gate.

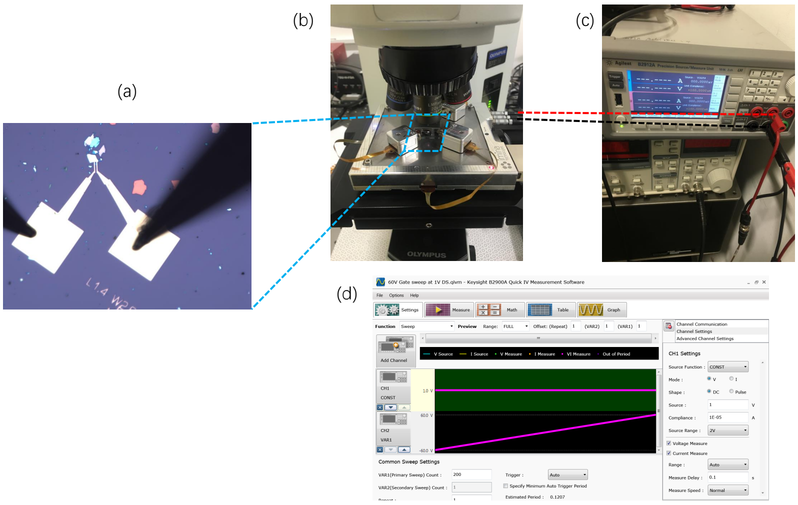

Function: Sweep
Range: FULL
Offset: (Repeat) 1 (VAR2) 1 (VAR1) 1

CH1 Settings
Source Function : CONST
Mode : ● V ○ I
Shape : ● DC ○ Pulse
Source : 1 V
Compliance : 1E-05 A
Source Range : 2V
☑ Voltage Measure
☑ Current Measure
Range : Auto
Measure Delay : 0.1 s
Measure Speed : Normal

Common Sweep Settings
VAR1(Primary Sweep) Count : 200
VAR2(Secondary Sweep) Count : 1
Trigger : Auto
☐ Specify Minimum Auto Trigger Period
Estimated Period : 0.1207

Figure 5.7: Illustration for electrical measurement. (a) Optical image of the device with source and drain probes contacted. (b) Image of the probe station under manipulation. (c) Image of the source meter. (d) User interface of data collection software.

Fig. 5.7 (a) shows the fabricated device (yellow squares are gold electrodes) and probes (black needles). In Fig. 5.7 (b), the probes are manipulated under optical microscope to locate the device. As shown in Fig. 5.7 (c), the probe station is connected to a source meter (model Agilent B2912A) with a current resolution of 10^{-13} A. Then, the source meter is further connected to a computer for data collection. Fig. 5.7 (d) is the user interface of the software for data collection.

Using the software, the minimum and maximum applied voltages are -80 and 80 volts. When gating the device, we usually set the range of gate voltage from -60 to 60 V. Moreover, different sweep modes can be achieved by altering the software parameters. For example, sweep rate can be changed in order to achieve a fast sweep or slow sweep. And single sweep and loop sweep can also be conducted in order to study the hysteresis phenomenon.

Chapter 6

Experimental results on monolayer MoS_2 obtained by rapid O_2:Ar plasma treatment

In Chapter 2 Fig. 2.9, we have shown the system parameters of the FISCHIONE 1020 inductively-coupled plasma chamber. In this Chapter, the experimental results are mainly based on monolayer MoS_2 being exposed in O_2:Ar plasma with a 2s duration in the FISCHIONE 1020 inductively-coupled plasma chamber. The gas source used is oxygen/argon mixed gas with stoichiometric ratio O_2 25% and Ar 75%. Samples are placed in the center of the plasma chamber to directly interact with plasma species whose ion energy is 12 eV.

In this Chapter, we firstly study the morphology of samples before and after plasma irradiation from AFM, TEM, Raman and PL. We find that plasma can not only introduce vacancies into the system, but also cause the formation of a amorphous overlayer which increases the thickness of the flake. Then we compare the electronic performance of the monolayer MoS_2 field-effect transistors before and after treatment from threshold voltage, field-effect mobility and photoresponsivity. We find that both μ_{fe} and R_h are improved after treatment. V_{th} also drops, causing the device to be switched on more easily. Moreover, we also utilize the polymer encapsulation technique to improve the device performance, since water vapour in the air can significantly attenuate the device mobility and cause undesirable hysteresis in transfer characteristics.

Finally, we try to utilize the inductively-coupled atmospheric plasma jet to modify devices. However, due to the bombardment effect, samples are severely damaged after treatment.

6.1 Inductively-coupled plasma cleaner

6.1.1 Morphology modification

Figure 6.1 shows the AFM height images of a monolayer CVD MoS_2 flake with a typical triangle shape. We measured the same flake before and after 2s plasma treatment. The height profiles before and after the treatment were extracted along the blue lines in Figure 6.1. As shown in Figure 6.2, the height of the chosen area doubled from 0.56 *nm* to 1.19 *nm* after the plasma treatment, indicating a significant plasma-caused amorphous overlayer within the system.[35, 59]

Thickness increasing has also been observed by Zhu *et al* and Jakub *et al.*[35, 59] In Zhu's work, a RF plasma bas been generated with plasma power 2500 *W*. The pressure in their plasma chamber is 260 *mbar*, which is five times larger than ours, and which means they have larger reaction rate due to more chemical species. Another difference is their samples are placed 52 *cm* away from the plasma to avoid severe physical damage. However, our samples are placed in the center of the plasma. That's the reason that their treatment duration can be up to 20 *mins*, but ours is 2 seconds.

Jakub *et al* also observe that the edge heights double after five-second oxygen plasma treatment. A longer exposure duration (28 seconds) in the plasma will cause visible voids in the sample, specifically the sample is physically damaged after 28s of plasma irradiation.[59]

Another notable work was done by Liu *et al.* They utilized RF Argon plasmas to thin multilayer MoS_2 to fabricate monolayer flakes, which gives an insight into large-scale synthesis of 2D TMDs for future industrial production.[60] The differences between their work and ours are mainly at plasma species, chamber pressure and exposure duration. They don't have oxygen in the plasma, namely no chemical reaction happens during the exposure. Their chamber pressure is 40 pa (0.3 $Torr$), which is ten times larger than ours (40 $mTorr$). Their exposure duration can be up to 6 $mins$, because the multi-layer MoS_2 flakes are so thick that they can endure such a long duration. Our plasma is generated from a mix gas with 25% oxygen and 75% argon. The physical damage from argon should be aware, since we have learned that argon plays an important role in physical etching from Liu's work.[60]

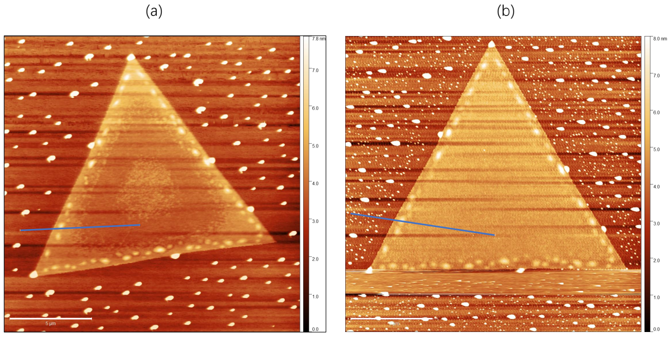

Figure 6.1: AFM height images for a CVD monolayer MoS_2 flake. (a) and (b) are before and after treatment images. Blue lines correspond to the area where height profiles were extracted in Figure 16. White lines are scale bars with value of 5 μm.

Moreover, another informative work done by Kim *et al* should be highlighted.[61] Kim's work is closely related to ours, because their plasma configuration is nearly the same as ours. They use an inductively-coupled plasma source with a standard RF frequency of 13.56 MHz. More importantly, their working pressure is 18 $mTorr$, which is comparable with ours (40 $mTorr$), indicating a similar concentration of plasma species as in our work. Although their samples are polyimide, which is used for flexible electronics devices, the observation is similar as Jakub's work[59] and ours. They discover that the root mean square roughness of the polyimide surface increases significantly after oxygen-plasma irradiation.[61] Furthermore, Ruoff *et al* utilize Ar^+ ion beam to treat polyimide surface and their observation is taht the surface is being physically etched due to the ion bombardment.[62] So far, we have the impression that reactive species like oxygen can cause an increasing of surface thickness and roughness. However, noble gas and its ionized species mainly physically etch the surface and cause damage.

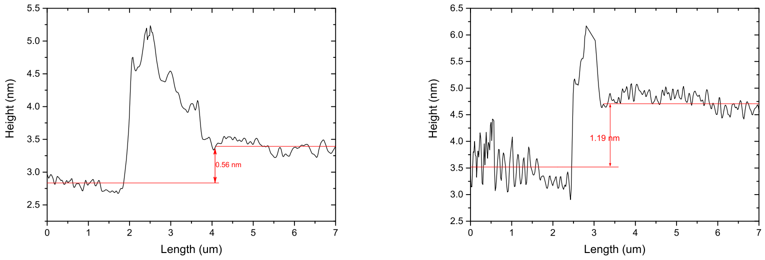

(a) (b)

Figure 6.2: (a) and (b) show height profiles along the blue lines in Fig. 6.1 for 0s and 2s-plasma treatment. The height of the chosen area changes from 0.56 to 1.19 nm after 2s exposure.

Figures. 6.3 (a), (b) present TEM images of a monolayer MoS_2 flakes before and after plasma treatment, respectively. The monolayer MoS_2 sample was obtained by micromechanical exfoliation, and transferred onto a TEM grid by the wet polymer stamp method.[63] Corresponding Fast Fourier Transforms (FFTs) are included as insets. From real space images, it can be seen that a large change in contrast on some flake areas can be noted after 2 seconds of exposure to the plasma. This can be attributed to plasma-introduced vacancies and inevitable physical etching. Insets are corresponding discrete Fourier transform images based on each real space image. In 2D Fourier transforms of a grayscale image, the center of the frequency domain represents how frequently black pixels appear in the original image. In (a), the reciprocal lattice shows a typical hexagonal shape, indicating that the lattice pattern in real space is well-arranged and hexagonal. However, after 2s exposure to plasma, a ring appears around the center of the FFT image, suggesting disorder of the atom arrangement in the real space. There is a simple analogy to help understanding this. In 1D Fourier transforms, the frequency domain of a regular pattern like sine or cosine is trivial. However, with a pattern losing its symmetry and becoming non-periodic, its Fourier transform will become more complicated. Thus, based on the evolution of (a) to (b), we can conclude that plasma treatment breaks the translational symmetry of the real space lattice by introducing vacancies.

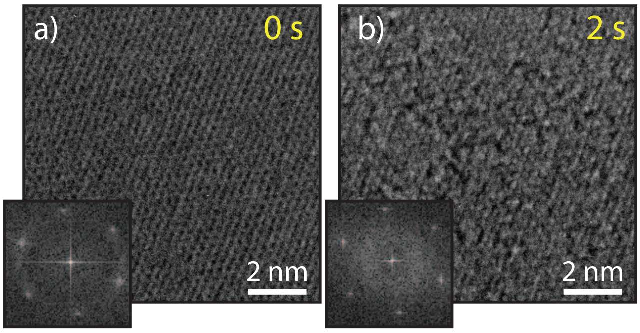

Figure 6.3: Characterisation of the plasma-oxidised MoS_2 CVD monolayers: (a) TEM micrograph of a pristine monolayer of CVD MoS_2. Inset shows the FFT. (b) TEM image of the same MoS_2 flake after undergoing 2 seconds of plasma treatment. Note the change in crystallinity as indicated by the disperse FFT in the inset.

Figures. 6.4 (a),(b) show the spatially-resolved Raman maps of the CVD-grown MoS_2 centered at 385 cm^{-1}, which corresponds to the in-plane vibrational mode (E^1_{2g}), before and after plasma treatment. It can be seen that 2s of plasma exposure causes a drastic change in the E^1_{2g} intensity. The detailed intensity change from (a) to (b) is described in (c). Green (red) line in fig. 6.4 (c) shows the average intensity of the whole image from (a) (or (b)). It is clear that both E^1_{2g} and A_{1g} peaks reduce remarkably after 2s of plasma. This phenomenon has also been found by other researchers.[34, 35, 59, 60]

Liu *et al* and Zhu *et al* both discovered that intensities of E and A peaks of a monolayer MoS_2 flake decrease after plasma treatment.[35, 60] Jakub *et al* find, in a four-layer MoS_2 flake, that both E and A peaks are attenuated by the plasma exposure.[59] Kang *et al* demonstrate a quantitative analysis on Raman spectra of a monolayer MoS_2 flake before and after oxygen-plasma treatment.[34] They claim not only the intensity of E and A peaks decrease but also their full-width half-maxima (FWHM) broaden nearly ten times after the treatment. We also find the similar phenomenon which is summarised in Table. 6.1. In our case, the FWHM of E (A) peak increases significantly from 3.18 (5.18) to 13.18 (37.7) eV. Moreover, the E^1_{2g} peak shifts from 384.8 cm^{-1} to 374.5 cm^{-1} but the A_{1g} peak shifts from 405.3 cm^{-1} to 411.0 cm^{-1} after treatment. This observation is also consistent with Liu and Jakub.[59, 60] It can be attributed to the change of force constant and variation in the dielectric screening environment.[58, 64]

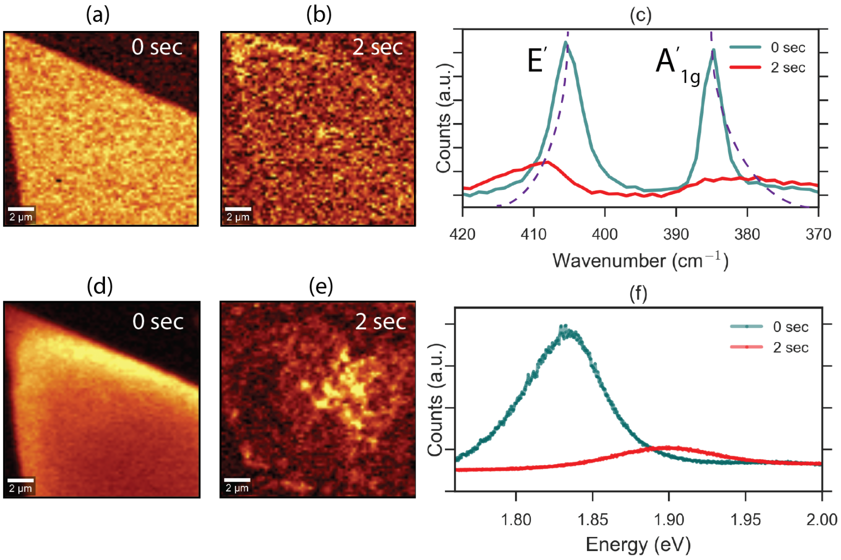

Figure 6.4: Spectroscopic mapping of the plasma-oxidised MoS_2 CVD monolayers: Raman maps of a monolayer flake before (a) and after (b) plasma treatment, filtered for the in-plane E^1_{2g} mode at 385 cm^{-1}. (c) Raman spectrum average from the flake area demonstrating the intensity quenching and peak shifts of the MoS_2 modes. PL maps of the same flake before (d) and after (e) treatment, tracking the emission corresponding to the direct recombination an A exciton. (f) Averaged PL spectra demonstrate the direct recombination quenching in the monolayer MoS_2 after plasma exposure.

Figure. 6.4 (d) shows the pristine photoluminescene (PL) map of the same flake centered at 1.835 eV (energy of an A exciton). It tells, in real-space, that the lattice is well-arranged due to the uniform distribution of intensity. However, after 2s of plasma treatment, in (e) the intensity of A exciton drops from 15.7 to 2.18 a.u. This significant quenching of the A exciton intensity has also been observed by other researchers.[34, 59, 60, 65] In the above references, the PL quenching appears in monolayer MoS_2 to 4L MoS_2. And it is due to the distortion of the MoS_2 lattice caused by plasma bombardment.

Table. 6.1 is a quantitative analysis on Raman and PL spectra reflected in Fig. 6.4. In Table. 6.1, fitting functions for both Raman and PL spectra are Gaussian functions.

Table 6.1: Summary of spectroscopic fits before and after plasma treatment. Pos and Amp stand for peak position and amplitude. The units for Pos and FWHM are cm^{-1}. The unit for FWHM in PL A exciton is eV. The unit for Amp is arbitrary.

	E^1_{2g} peak			A_{1g} peak			PL A exciton		
Plasma exposure time	Pos	FWHM	Amp	Pos	FWHM	Amp	Pos	FWHM	Amplitude
0 seconds	384.8	3.18	5.71	405.3	5.18	5.77	1.83	0.202	15.7
2 seconds	374.5	13.18	1.45	411.0	37.7	0.84	1.90	0.362	2.18

6.1.2 Photoresponsivity

In this section, we describe how our probe station shown in Fig. 5.7 (in Chapter 5) is integrated with a laser system. All the electrical measurement done with laser illumination is carried out under ambient conditions. The laser system has two wavelengths, 488 and 632 nm, which can be operated independently. Both of them can be tuned under five levels of power (shown in Table. 6.2). In order to guide the laser beam onto the MoS_2 phototransistors, a condenser lens is used. The configuration of the condenser lens is an OLYMPUS LMPlanFL N with magnification 20× and numerical aperture (NA) 0.4. The NA value is an important parameter because the calculation of the laser spot size depends on it, which is shown as below,

$$D = \frac{1.22\lambda}{NA} \tag{6.1}$$

where λ is the wavelength of the laser and NA is the numerical aperture of the consender lens. D is the diameter of the laser spot size. It can be seen that the laser spot size depends on the incident laser wavelength. With spot size calculated, the power density can be obtained. Table. 6.2 summaries the detailed information of the laser parameters.

Figure. 6.5 (a) shows a false-color helium-ion image of a CVD monolayer MoS_2 phototransistor where two electrodes (source and drain) are fabricated with 40 nm Au and 10 nm Ti. We can clearly identify that the area of the device is larger than the laser spot size (3 μm^2). Thus, the laser spot avoids the Au electrodes during illumination and all of the collected photocurrent originates in the MoS_2. However, in some of the published works, researchers apply global laser illumination in which impinging on the gold electrodes can not be avoided, [8, 66, 67] implying that the measured current contains a contribution from thermal effect of the gold electrodes. Hence, our results and theirs are uncomparable due to different ways of illumination. Wi *et al* demonstrate an enhancement of photovoltaic response in multilayer MoS_2 transistors by plasma treatment using various gas sources,[68] but they don't show their laser spot size or other detailed information about their laser configuration, leading to an incomparability with our work. Gough *et al* demonstrate photocurrent enhancement in MoS_2 phototransistors by introducing quantum dots.[69] In their work, they clarify that their spot diameter and channel length are 3 μm and 5 μm, respectively, which makes their work and ours comparable.

Table 6.2: Summary of the laser spot size, power and power density for both wavelengths (488 and 632 nm). Laser power can be tuned to five different levels.

Wavelength (nm)	Diameter (μm)	Area (μm^2)
488	1.488	1.739
632	1.928	2.920

	Power (μW)				
488	0.0072	3.6	7.2	36	72
632	0.006	3.0	6.0	30	60

	Power density ($\mu W \cdot \mu m^{-2}$)				
488	0.0041	2.1	4.1	20.7	41.4
632	0.0021	1.0	2.1	10.3	20.6

Figure. 6.5 (b) and (c) show the output characteristics of the device shown in (a), with and without plasma treatment. In (b), the device shows a typical Ohmic contact, because the current is symmetric with respect to the origin. It is also clear from (b) that output current increases with the increasing of laser power. When the laser power reaches 72 μW, the corresponding photocurrent I_{ds} achieves ± 10 μA at $V_{ds} = \pm 5$ V. After treated by plasma for 2s, the device demonstrates a doubled photocurrent with more than 25 μA at the maximum laser power. Curves have the same trends under 632 nm laser irradiation. To avoid redundance, we only show the extracted information from 632 nm laser experiment in Tables. 6.3 and 6.4.

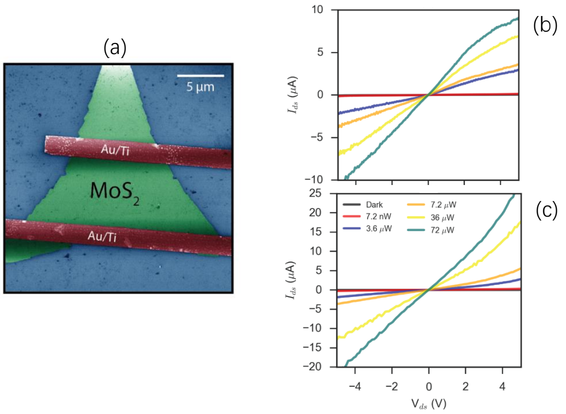

Figure 6.5: FET output characteristics under 488 nm laser illumination: (a) False colored helium-ion micrograph of a monolayer MoS_2 phototransistor device with two gold electrodes contacted. The blue area is the SiO_2 substrate. The scale bar is 5 μm. (b) Output curves of the untreated monolayer MoS_2 device, demonstrating a good Ohmic contact between the material and the metal electrode. Output current increases with laser power increasing. (c) Post-plasma treatment IV curves show a similar trend with increasing laser power, and the output current has increased substantially for the same device.

Moreover, the photoresponsivity R_{ph} can be extracted from Fig. 6.5 (b) and (c) and is summarised in Table. 6.3. R_{ph} is defined by the ratio of photocurrent to laser power. Thus, the calculated R_{ph}s under 488 nm laser for pre and post treatments are 3.7×10^{-2} and 7.3×10^{-2} A/W, respectively. It can be seen that R_{ph} is doubled after plasma treatment. This phenomenon can be attributed to the formation of a MoO_x overlayer or oxygen atoms physically being adsorbed onto the MoS_2 surface. The formation of MoO_x can be regarded as chemical adsorption[34, 35, 59] and surface adhesion of oxygen atoms can be respected as physical adsorption.[70, 71, 72] The chemical-adsorption caused photoresponsivity can be explained by the charge trap effect in the MoS_2/MoO_x,[73] because, at the interface between MoS_2 and MoO_x, a conduction band offset will form, resulting from different Fermi levels of MoS_2 and MoO_x. Due to the conduction band offset, a built-in electric field pointing from MoS_2 to MoO_x is generated at the interface. The built-in electric field can trap holes and avoid electron-hole recombination, leading the enhancement of photocurrent.[73]

The above is the mechanism for photocurrent improvement caused by chemical adsorption. However, based on our observation in Fig. 6.2, the interaction between MoS_2 and oxygen plasma is mainly due to physical adsorption of oxygen atoms. Because chemical adsorption will decrease the thickness, which contradicts our experimental observation in Fig. 6.2. But physical adsorption can cause thickness and surface roughness increase,[70, 71, 74, 72] which match our observation well. A detailed calculation and comparison between chemical- or physical- adsorption caused surface-thickness changes are shown in Chapter 7.

Photocurrent enhancement caused by physical adsorption can be understood as a charge transfer or energy transfer effect.[75] The charge transfer effect is mainly used to describe the optical-electronics property of a hybrid system. The principle of a charge transfer effect is that electron-hole pairs are generated in the active component (like physical adsorbent, quantum dot, or dopant) under laser illumination, and one type of carrier can be transferred to the channel, resulting in enhancement of current.[75] In Gough's work,[69], the active components are CdSeS/ZnS quantum dots, which are introduced into MoS_2 devices by spin coating. They observe photocurrent enhancement and attribute it to the charge transfer effect. They further conduct PL mapping in which they find PL peaks of the quantum dots are quenched significantly because carriers are transferred into MoS_2 channel, avoiding exciton recombination emitting photons.[69] Since their device dimension, laser wavelength and illumination area (only channel materials rather than the whole device) are similar as ours, we can compare the results. After QD sensitizing, their monolayer MoS_2 devices show a maximum R_{ph} of $2.1 \times 10^{-2}\ A/W$.[69] Our maximum R_{ph} is $7.9 \times 10^{-2}\ A/W$. It can be seen that our rapid-plasma-treatment technique not only provides a promising way to improve the device performance but also an easier way to fabricate devices compared with the spin-coating based QD sensitizing technique.

Table 6.3: Photoresponsivity R_{ph} of the device shown in Fig. 6.5 (a) before and after plasma treatment. The unit of R_{ph} is $A \cdot W^{-1}$.

	488 nm	632 nm
Plasma exposure time	R_{ph}	R_{ph}
0 seconds	4.3×10^{-2}	3.7×10^{-2}
2 seconds	7.9×10^{-2}	7.3×10^{-2}

Furthermore, we study the temporal response of the same monolayer MoS_2 phototransistor shown in Fig.6.5 before and after plasma treatment. As can be seen in Fig. 6.6 (a), the photocurrent has been improved two times when the 488 nm laser irradiation is modulated through 5 sec ON/5 sec OFF cycles at a power of 36 μW and $V_{ds} = 5\ V$. After treatment, the fall and rise times are extracted from single exponential fits in (b) and (c) respectively. The time-resolved photoresponses compare favourably with the evaporated MoO_x overlayer devices.[73]

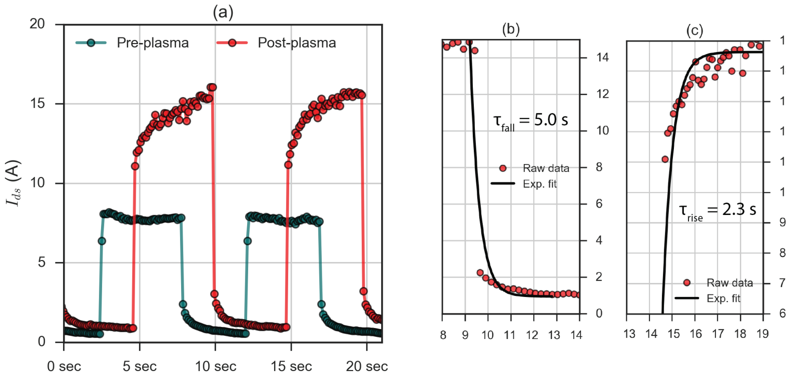

Figure 6.6: Time response of the device before and after plasma treatment, V_{ds} is set at 5V. (a) Comparison of photocurrent response over laser irradiation cycles lasting 5 seconds. (b) Exponential fit of the fall component of the photoresponse for the treated device. (c) Exponential fit of the rise component of the from the next cycle.

Importantly, Fig. 6.6 provides another angle to study the optoelectroni properties of the system. The speed of the photoresponse decays after plasma exposure, which can be explained by the charge transfer effect and is consistency with other published works. [75, 76, 77, 78, 79] As mentioned above, our system is a hybrid system where oxygen atoms are physically adsorbed onto the MoS_2 surface. Based on the charge transfer effect, the adsorbed oxygen atoms are the active component. Thus, under laser illumination, one type of carriers in photo-generated excitons reside in the layer of active component, causing the reduction of electron-hole recombination rate and increase of the carrier lifetime.[75] Thus, the speed of photoresponse will drop due to the increasing of carrier lifetime, which is clearly reflected in Fig. 6.6 (a). It can be seen that the untreated device (green line) shows an instant response and jumps to a plateau when the laser is switched on, namely its response function is a step function. However, the post-treated device needs a longer response time to reach the maximum. The decayed speed of photoresponse in a hybrid 2D system has also been observed by other researchers, as we now summarise.

Kufer *et al* demonstrate photocurrent enhancement in few-layer MoS_2/colloidal PbS quantum dots hybrid system. Their temporal response shows a similar trend and comparable decay time to ours.[76] Yu *et al* fabricate a single-layer MoS_2 transistor with rhodamine 6G organic dye solution drop-cast on. They find photoresponsivity has been improved but response speed has dropped, which is consistent with our observation.[77] Moreover, the attenuated photoresponse speed has also been found in graphene/QD hybrid system.[78, 79] Liu *et al* report that pristine graphene transistors responsed to laser illumination rapidly.[78] However, after being fabricated in a hybrid system with PbS quantum dots, the response speed drops.[79]

From the above references, it can be seen that the fabrication of 2D-materials/QD hybrid systems are based on drop-cast, which is a physical process. Thus, in our case, the physical adsorption process of oxygen atoms onto the MoS_2 surface is similar to the formation of 2D-material/QD systems, because the two techniques realize the adhesion of an active component onto the surface of the device. This suggests that the charge transfer theory can be applied to our system. Furthermore, a theoretical elucidation of the charge transfer effect in MoS_2/QD hybrid system has been reported by Raja *et al.* They claim that dielectric screening originated from increasing thickness of MoS_2 layer and charge transfer effect are two mechanisms competing in the electron transport during laser illumination, by studying the relation between nonradiative energy transfer and number of layers.[80] In our case, the dielectric screening effect doesn't exist since the studied samples are monolayers, and the charge transfer effect plays an important role in electron transport under laser irradiation.

6.1.3 Mobility

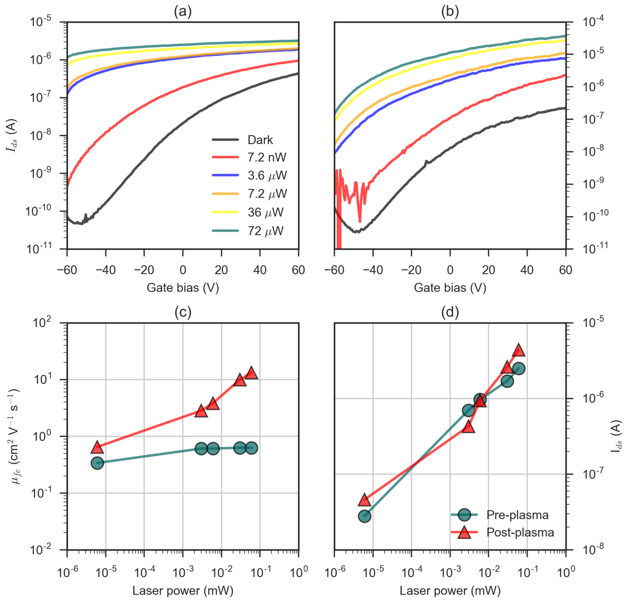

Figure 6.7: Gate characteristics, field effect mobility and photocurrent comparison before and after plasma treatment: (a) Transfer characteristics of the same untreated device, demonstrating standard n-type FET behaviour and increasing of photocurrent in the channel at higher laser powers. (b) Similarly to the IV curves in Fig. 6.5, the level of current in the transfer curves of the plasma-exposed device has increased, in this case by one order of magnitude at higher laser powers. (c) Mobility comparison before and after plasma treatment as a function of laser power. (d) Photocurrent comparison before and after plasma exposure as a function of laser power. The laser wavelength is 488 nm.

Figure. 6.7 tracks the MoS_2 channel field effect mobility before (a) and after (b) plasma exposure under 488 nm laser irradiation. V_{ds} is set at 1 V in all the transfer curves. From Fig. 6.7 (c), when the device is exposed to the plasma for 2 seconds, the field-effect mobility increases 10-fold (0.95 to 13.5 $cm^2 \cdot V^{-1} \cdot s^{-1}$) at the maximum laser power. In dark, the μ_{fe} nearly remains the same level, with $\mu_{fe} \sim 0.34\ cm^2 \cdot V^{-1} \cdot s^{-1}$ for pre-treatment and $\mu_{fe} \sim 0.40\ cm^2 \cdot V^{-1} \cdot s^{-1}$ for post-treatment. The enhancement of μ_{fe} is consistent with the improvement of photocurrent and photoresponsivity. Based on the charge transfer effect, it is clear that the retention of one type of carriers in the active component can improve the electron mobility due to the attenuated electron-hole recombination rate. Mobility enhancement is summarised for the two wavelengths in Table. 6.4.

Table 6.4: Mobility at maximum laser power for different illumination wavelengths before and after plasma treatment. The unit of μ_{fe} is $cm^2 \cdot V^{-1} \cdot s^{-1}$.

	488 nm	632 nm
Plasma exposure time	μ_{fe}	μ_{fe}
0 seconds	0.95	0.63
2 seconds	13.5	13.3

6.1.4 Threshold voltage

By applying ratio method (RM) (mentioned in Chapter 2) to Fig. 6.7 (a) and (b), V_{th}s can be extracted. After transferring Fig. 6.7 (a) into a linear plot, we find that the device is already in the on state at $V_g = -60\ V$ when the laser power exceeds 3.0 nW. Thus, it is impossible to extract V_{th} from it. Referring to Fig. 6.7 (b), which shows transfer curves for the post-treatment device, corresponding linear plot is shown in Fig. 6.8 (a).

In Fig. 6.8 (b), we extracted V_{th}s by using RM. With laser power increasing, V_{th} shows a dramatic shift towards the negative region. As mentioned, RM shows the intrinsic V_{th} of a device. Thus, oxygen-plasma treatment changes the intrinsic properties of the device. As mentioned above, we believe that the adhered oxygen atoms increase the surface thickness and causes the electronic properties of the device to be changed. It is known that laser illumination on a semiconductor can generate electron-hole pairs (excitons) when the photon energy is comparable to the semiconductor band gap. In our case, the device still shows an n-type FET behaviour after plasma exposure, as seen in Fig. 6.7 (b), suggesting that the majority carrier in the system is still the electron. Then, based on the observation of enhanced photocurrent, we conclude that holes reside in the active component (adhered oxygen atoms), leading the electron concentration to be increased. Hence, the post-treated n-type 2D FET becomes easier to switch on with a lower threshold voltage. This is the reason why V_{th} shifts to lower voltage with the increasing laser power, as shown in Fig. 6.8 (b).

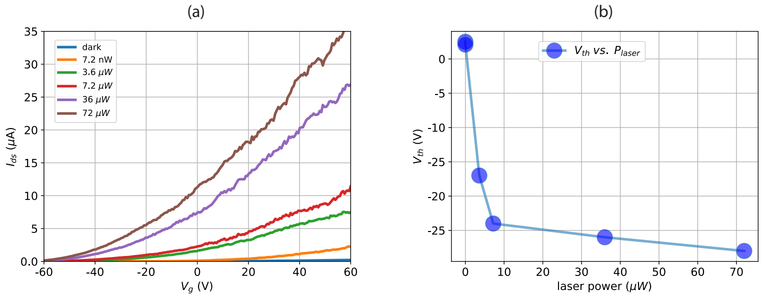

Figure 6.8: (a) Linear plot for the transfer curves under 488 *nm* laser with different power level in Fig. 6.7 (b). (b) Extracted V_{th}s by using RM. V_{ds} is set at 1 V in all the transfer curves.

6.1.5 Polymer encapsulation

(Measured devices are not treated by plasma in this section.)

In this section, we study the device performance under polymer encapsulation. There are two reasons to study how polymer protection affects the device performance. Firstly, impurity scattering introduced by dirty surface and gaseous molecules can significantly attenuate the device mobility.[81] Devices protected by polymers can effectively avoid mobility degradation from impurity scattering. Secondly, in the previous section, we discussed the electronic performance of a monolayer MoS_2 FET *globally* treated by oxygen plasma. By combining the polymer-encapsulation technique and electron-beam lithography together, we can *locally* treat devices and fabricate 2D heterostructure based on monolayer MoS_2. The 2D heterostructure can be further designed to realize 2D semiconductor superlattices, which is a promising architecture for neuromorphic electronics and spin filters, which will be discussed in the Outlook Chapter.

Threshold voltage

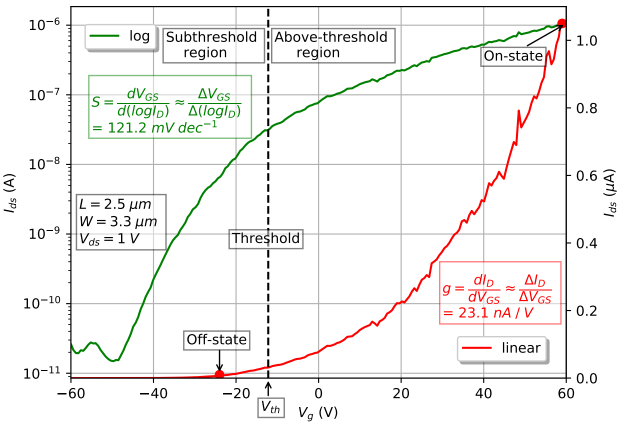

Figure 6.9: The transfer curve of a five-layer MoS_2 device measured in air. The information of device dimension, transconductance and sub-threshold swing is included. V_{ds} is set at 1 V. Channel length and width are 2.5 μm and 3.3 μm respectively.

In Fig. 6.9, the channel material is five-layer MoS_2 prepared by mechanical exfoliation. The device performs as a typical n-type field-effect transistor with on-off ratio of 10^5, transconductance 23.1 $nA\ /\ V$, and sub-threshold swing 121.2 $mV\ dec^{-1}$ under ambient conditions. The transconductance g reflects the performance of a FET when it plays a role of an amplifier in a circuit. Larger g values indicate better amplification ability. The sub-threshold swing S evaluates the performance of a FET working as a logic device. A smaller S indicates better stability of the device at off state. The expressions for both g and S are shown in Fig. 6.9.

The threshold voltage is a key parameter in a transistor. It evaluates how easily a FET can be switched on and off. Several methods were invented to extract it based on transfer curves. Here, we employed four different methods mentioned in Chapter 2 to extract threshold voltages based on Fig. 6.9. V_{th}s from different methods are summarised in Table. 6.5.

Table 6.5: V_{th}s extracted from Fig. 6.9 with four calculation methods in Chapter 2.

Methods	CC	ELR	GELR	RM
V_{th} (V)	3.92	21.9	11.9	-1.41

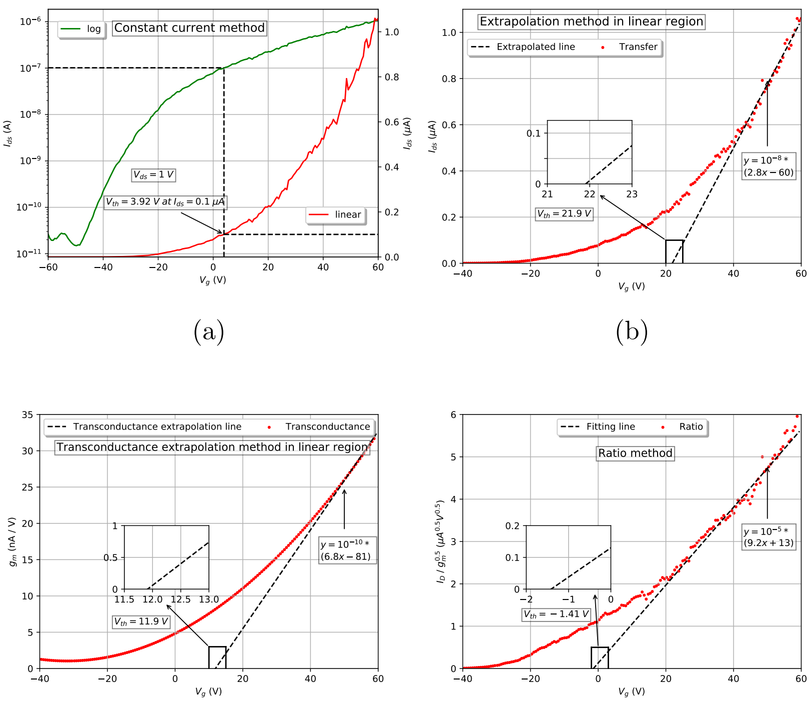

(a) (b)

(c) (d)

Figure 6.10: Different methods of threshold voltage extraction.(a) CC. (b) ELR. (c) BMLE. (d) RM. Results are summarised in Table. 6.5.

In Fig. 6.10 and Table. 6.5, it can be seen that threshold voltages extracted through different methods vary significantly compared with MOSFETs, whose threshold voltages change slightly under these methods.[30] Several factors are responsible for the phenomenon. Firstly, the dimension of a MOSFET is much smaller than our devices. In our case, the channel length is 2.5 μm, nearly one hundred times larger than a MOSFET. Secondly, the gate in our case is a back gate geometry which has a less efficient gating effect due to the 285 nm SiO_2. However, high efficiency top gating holds in the case of a MOSFET. Other factors, such as parasitic resistance, gate-source capacitance and mobility degradation effects are more complicated and need to be studied in detail.[30, 31, 82, 83, 84, 85] Because V_{th} extracted by RM reflects the intrinsic threshold voltage, the significant difference in extracted V_{th}s between other three methods and RM indicates a mobility degradation effect and parasitic resistance.[30, 31] Parasitic resistance can't be eliminated after the device fabrication, but mobility degradation can be optimized by polymer encapsulation.

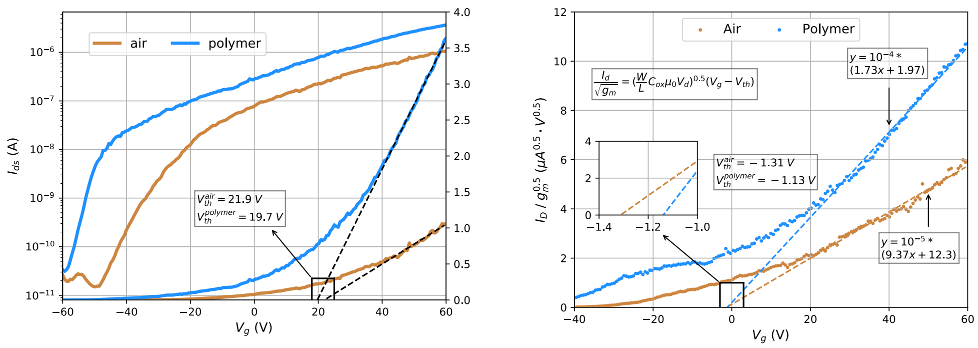
(a) (b)

Figure 6.11: Transfer characteristics of the same device as in Fig. 6.9. (a) Threshold voltages extracted from the ELR method. (b) V_{th}s extracted from RM with fitting functions shown. The orange curve is measured in air and the blue curve is measured under polymer protection.

The polymer used in this section is the same as the polymer used in the EBL section. The polymer is polymethyl methacrylate (PMMA) with a molecular weight 950k, formulated in anisole with mass concentration 3%.

Figure 6.11 (a) measures the transfer characteristics of the same device as in Fig. 6.9 in air and polymer, respectively. It is clear that the magnitude of the channel current measured in polymer is about 3 times larger than that measured in air. The reason responsible for the increasing current is that the PMMA layer protects the channel from the gaseous molecules in the air. Gaseous molecules play the role of impurity scattering centers, which attenuate both current and mobility of the device.[32, 81, 82] V_{th}s are extracted based on the ELR method. As can be seen, V_{th} is 21.9 V in air and it slightly shifts towards the negative region to 19.7 V in polymer, showing a difference of 2.2 V.

In Fig. 6.11 (b), we continue to study the V_{th} by using the RM. V_{th} in air is -1.31 V and -1.13 V in polymer. The difference between measuring in air and polymer is -0.18 V, which is much smaller than the 2.2 V extracted from ELR method. The small V_{th} difference calculated by RM tells that polymer encapsulation doesn't change the intrinsic performance of the device, namely it doesn't introduce any chemical or physical reaction to change the lattice structure of MoS_2. This guarantees the feasibility of the polymer-encapsulation technique, because it is undesirable to improve the device performance by sacrificing the intrinsic merits of the materials.

So far, we have evaluated how the polymer-encapsulation technique optimizes the threshold voltage and weakens the mobility-degradation effect. In the following, we are going to present that polymer encapsulation can significantly improve the stability of MoS_2 FETs. We measure the transfer characteristics under both ambient and encapsulation conditions, under three sweep rates (1, 2 and 10 V/s) of back-gate voltage. As mentioned in Chapter 5, loop sweep and various sweep rates can be achieved by changing the software setup.

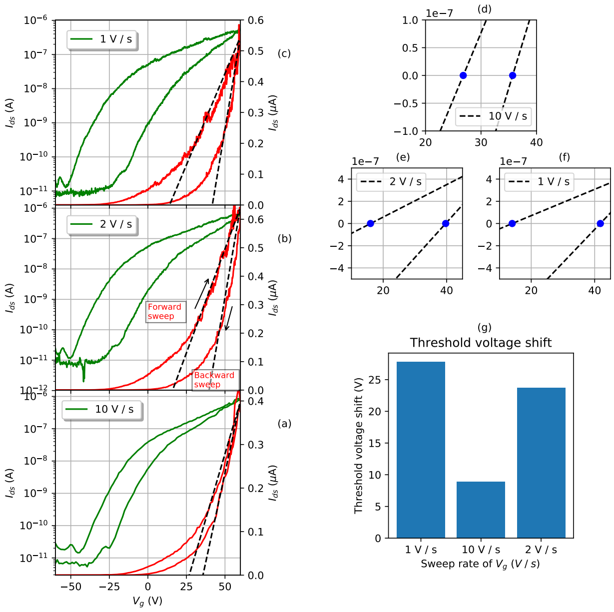

Figure 6.12: Gate loop sweep under ambient conditions. (a), (b) and (c) are transfer characteristics under back-gate sweep rate 10, 2 and 1 V/s, respectively. (d), (e) and (f) are the corresponding zoomed areas to show V_{th}s. (g) summarises the threshold voltage shifts. V_{ds} is set at 1 V for all the transfer curves.

In Fig. 6.12 (a), (b) and (c), it can be seen that forward sweeps show higher current magnitudes than backward sweeps, which is same as in repoted works.[86, 87] This phenomenon is due to charge trapping and detrapping in the Schottky barrier in the MoS_2/metal contact.[87] (d), (e) and (f) are zoomed-in areas to show V_{th}s under each sweep rate. We define the threshold-voltage shift as the V_{th} difference between forward and backward sweep. In (g), threshold voltage shift decreases with sweep rate increasing. Threshold voltage shift drops from 25 V at a rate 1 V/s to 10 V at 10 V/s. It can be attributed that a faster sweep speed will suppress the molecular absorption on the surface, because the hysteresis is mainly caused by water vapor absorption on the surface.[86]

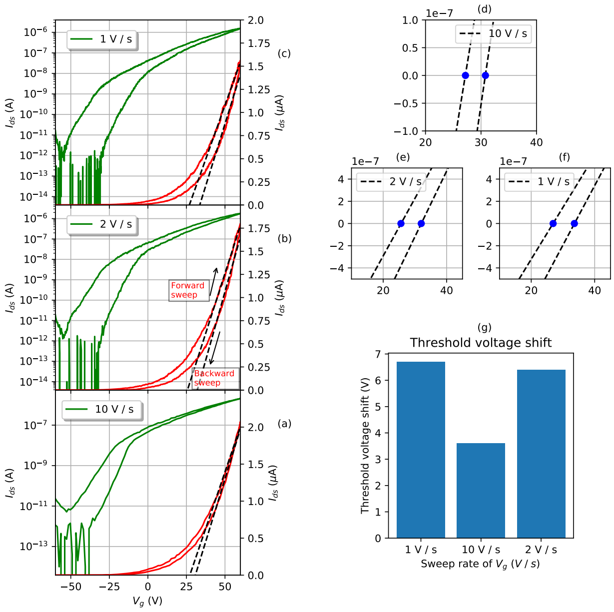

Figure 6.13: Gate loop sweep under polymer protection. (a), (b) and (c) are transfer characteristics under back-gate sweep rate 10, 2 and 1 V/s, respectively. (d), (e) and (f) are the corresponding zoomed areas to show V_{th}s. (g) summarises the threshold voltage shifts. V_{ds} is set at 1 V for all the transfer curves.

Figure. 6.13 is measured under encapsulation conditions. In (a), (b) and (c), we get the impression that the threshold-voltage shift becomes smaller compared with Fig. 6.12. From (d) to (f), the threshold-voltage shift drops with an increase of sweep rate, which shows a similar trend to that measured in air. In (g), it can be seen that threshold-voltage shift is 6.5 V at 1 V/s, which is already smaller than 9 V at 10 V/s measured in air. Hence, polymer protection can significantly enhance the stability of the device. Since stability is a crucial parameter of a field-effect transistor when it works as a logic unit, our polymer-encapsulation technique gives new insights into enhancing performance of two-dimensional field-effect transistors and future integrated circuit based on 2D FETs.

Mobility

In this section, we are going to discuss the difference in mobility when the device is measured in air or in polymer. Mobilities are extracted based on the the data shown in Fig. 6.9. Extracted mobilities are shown in Fig. 6.14.

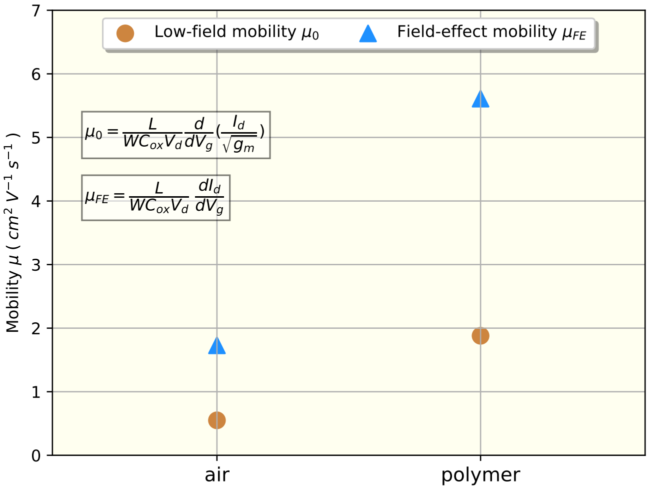

Figure 6.14: Mobility comparison between encapsulated and un-encapsulated measurements. Both field-effect mobility and low-field mobility are in the unit of $cm^2\ V^{-1}\ s^{-1}$.

Fig. 6.14 shows that both the low-field mobility μ_0 and field-effect mobility μ_{fe} are enhanced about by three times after encapsulation (low-field mobility is the mobility of the device in the presence of a low electric field[29, 31]). One reason is that the polymer protects the MoS_2 from impurity scattering caused by gaseous molecules. Due to the lower possibility of being scattered and a reduction of energy loss, electron mobility is enhanced. In order to further study the effects of encapsulation on mobility, we consider the model of a small-signal equivalent FET circuit.[5, 88] The small-signal equivalent FET circuit is a successful model to describe silicon-based MOSFETs. It has also been successfully applied to describe graphene FETs.[5] In Fig. 6.15, R_s and R_d are the contact resistances at the source and drain electrodes, respectively. After encapsulation, the value of R_s (or R_d) is same as the pristine contact resistance. The reason is that the fabrication technique, contact dimension, contact materials and temperature are not changed when we measure the same device after encapsulation. The above parameters mainly determine the contact resistance.[81]

After polymer encapsulation, the capacitance between gate and polymer C_{gp}, and source and drain $C_{polymer}$ will be introduced. Equation 2.7 shows $\mu_{fe} \propto C_{ox}^{-1}$. In the case of encapsulation, $C_{equivalent} = (C_{BG}^{-1} + C_{gp}^{-1} + C_{polyer}^{-1})^{-1}$, which means that the total capacitance becomes smaller, which resembles the situation where the total resistance is smaller than the resistance on each branch in the parallel circuit. Thus, the mobility is enhanced due to the inverse proportional relationship between μ_{fe} and $C_{equivalent}$ in Eq. 2.7.

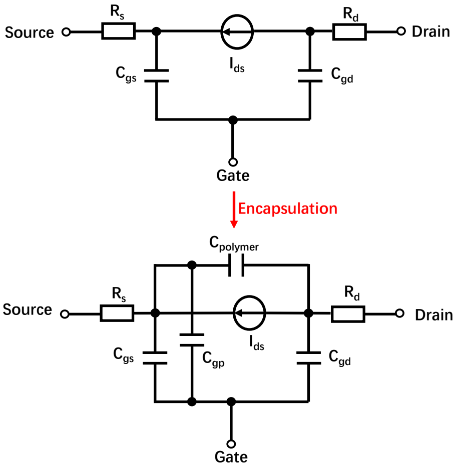

Figure 6.15: Small-signal equivalent FET circuits for pristine and encapsulated devices.

6.2 Atmospheric plasma jet

6.2.1 Damage evaluation

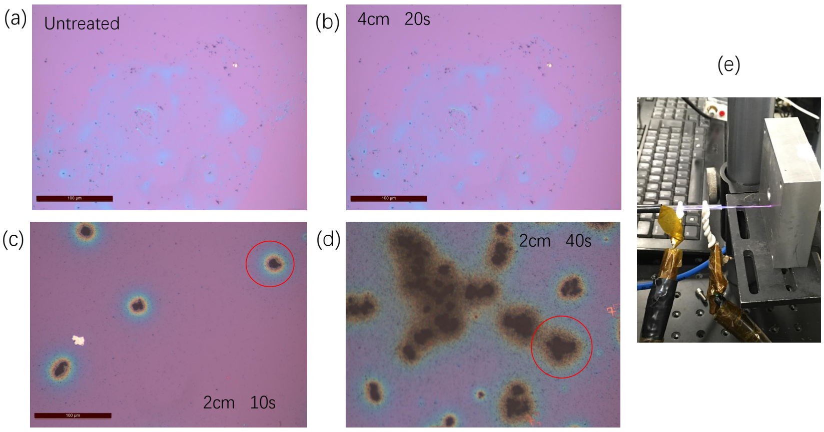

Figure 6.16: Substrates (SiO_2) treated under different conditions with an inductively-coupled atmospheric plasma jet. (a) is the untreated substrate. (b) is the same area as (a) with 4cm-distance and 20s-duration plasma exposure. (c) and (d) are treated areas on another chip (same substrate material as (a) and (b)) with 2 cm, 10 s and 40 s plasma, respectively. (e) Photo of the atmospheric plasma jet.

There are two reasons to conduct experiments based on atmospheric plasma jets. Firstly, the cost of an atmospheric plasma jet is much lower than that of the inductively-coupled plasma chamber, since it doesn't require the vacuum condition. Secondly, it can be used to conduct site-specific and mask-free modification on a sample. Ye *et al* successfully demonstrate site-specific and mask-free modification on graphene by using an atmospheric plasma jet with N_2:He (1:49) mixed gas.[38] In their case, a micro-plasma jet is generated through a glass tube nozzle whose diameter is 30 μm and smallest moving step size is 10μm.

A photograph of the inductively-coupled atmospheric plasma jet is shown in Fig. 6.16 (e). We identified the threshold distance for the plasma jet in terms of plasma introduced damage. In Fig. 6.16, the distance (4 cm or 2 cm) is defined as the distance between the outlet of the plasma jet and the surface of the sample. As can be seen in Figs. 6.16 (a) and (b), there is no damage with the distance set at 4 cm and duration set as 20 s. Both (c) and (d) clearly show damage as depicted by red circles. In (c), 2 cm and 10 s treatment introduces a medium level of damage, and with duration increasing, severe damage happens, nearly causing the whole chip destroyed in (d).

We can conclude that 4 cm is the safe distance for sample treatment with our plasma jet. However, the bombardment effect caused by the plasma jet is so strong that it can even severely damage the substrate, which is out of our expectation. When using an inductively-coupled plasma chamber, we never observe any physical damage on the substrate. Due to the severe damage caused by the bombardment effect, in order to treat samples by the inductively-coupled atmospheric plasma jet, further optimization needs to be done to decrease the ion energy or the voltage in the coupled coils.

Chapter 7

First principles study of oxygen-plasma-treated monolayer MoS_2

Based on Chapter 6 and published work,[35, 36, 59, 89] after plasma treatment, vacancies have been observed through TEM (Fig. 6.3) and surface thickness increasing has been discovered by AFM (Fig. 6.2). Both vacancies and increasing of thickness cause the MoS_2 lattice structure to be changed. In Chapter 6, we study how plasma modifies the monolayer MoS_2 at the device level. In this Chapter, we are going to zoom into the molecular level to study the electronic properties of oxygen-plasma-treated MoS_2.

Based on the experimental study in Chapter 6, from both pre- and post-treat devices, we only observed a semiconductor phase from transfer characteristics. Precisely speaking, after oxygen plasma exposure, devices still show n-type semiconductor behaviour, even though the V_{th} and μ_{fe} change. By applying *in situ* scanning transmission electron microscopy, Lin *et al* have proved that the phase transition from 2H to 1T in monolayer MoS_2 requires a temperature of $T = 600\ ^oC$ with a duration of at least 100 seconds.[90] The monolayer 1T structure can be understood as a collective displacement of S atoms in the bottom layer.[90] Then, Muharrem *et al* shows that the 1T MoS_2 nanosheet behaves as a typical metallic phase through electrochemical characterization.[91] Due to the energy required to convert from 2H to 1T,[90, 92, 93] it can be concluded that the 2H phase is a more common and stable existence for MoS_2 than 1T under ambient conditions.

In the following discussion, MoS_2 specifically refers to MoS_2 with a 2H crystal structure.

Moreover, before the discussion of calculations, the configuration of the calculation should be mentioned. CPU is an Intel(R) Core(TM) i7-6700HQ CPU @ 2.60GHz with 16 processor cores. Parallel computing is based on MPI & OpenMP with 4 MPI processes and 4 OpenMP Threads.

The calculation in this Chapter is based on the software QUANTUM ESPRESSO which is an open-source package that is freely available.[94]

7.1 Band structure and density of states

(The reason that we conduct band structure calculation through DFT rather than tight-binding model or $\boldsymbol{k}\cdot\boldsymbol{p}$ *method has been clarified in beginning of Chapter 4).*

In order to execute accurate band structure calculations, we need to choose the lattice constants carefully. Thus, we collected information about the 2D MoS_2 lattice structure from both experimental and theoretical publications. The lattice structure of MoS_2 is a typical hexagonal Bravais lattice. Lattice constants measured by experiment are $a = 3.15 \pm 0.02$ and $c = 12.30$ angstroms at room temperature.[95, 96] Theoretical values of the lattice structure are $a = 3.16$ and $c = 12.28$ angstroms,[97, 98, 17, 21, 99] where c is the distance between two neighbouring layers. The distance between neighboring Mo and S atoms is $d_{Mo-S} = 2.40$ angstroms, and the angle between the $Mo - S$ bond and the Mo plane is $\theta = 40.6^o$. [97, 98, 17, 21, 99] An Illustration of the above parameters are shown in Fig. 7.1.

Followed by the determination of the lattice parameters, we need to find out a proper vacuum size for the monolayer unit cell. This is because the QUANTUM ESPRESSO (QE) can't model an ideal 2D system. The only approach to model a 2D system is to increase the interlayer distance until the interlayer Van der Waals' force can be ignored. Thus, we define the final interlayer distance as the vacuum size c_v. This value will be reflected in the QE input files. Due to $c = 12.30$ angstroms, we tuned the vacuum size from 15 to 40 angstroms and studied the evolution of the total energy, band gap and calculation time. The band gap is defined by the difference between the highest occupied molecular orbital (HOMO) and the lowest unoccupied molecular orbital (LUMO),

$$E_g = E_{HOMO} - E_{LUMO} \tag{7.1}$$

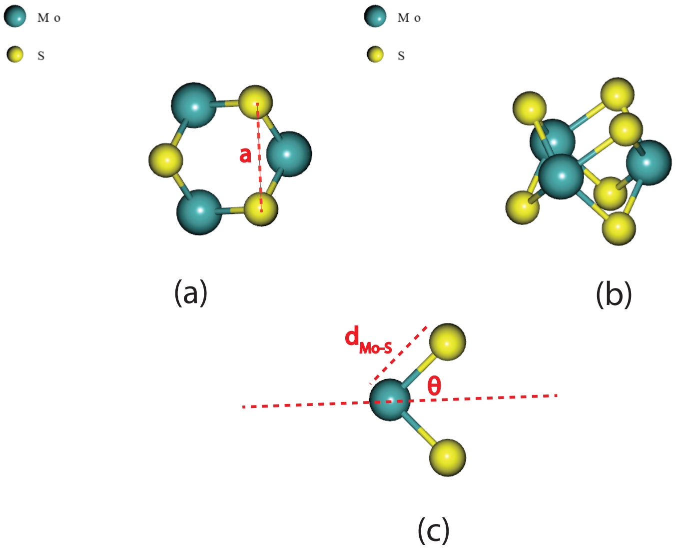

Figure 7.1: Lattice structure of monolayer MoS_2. (a) The top view shows a typical hexagonal Bravais lattice of monolayer MoS_2. (b) Front view shows a sandwich structure of monolayer MoS_2 where the plane of Mo atoms is sandwiched by two S-atom planes. (c) The unit cell of monolayer MoS_2 with bond length and angle depicted. ($a = 3.15$ angstroms, $d_{Mo-S} = 2.40$ angstroms, $\theta = 40.6^o$)

In the self-consistent field (scf) calculation, the number of bands needs to be determined in order to calculate the band gap. We define the number of bands for the single unit cell as 32, due to the 6 valence electrons in a S atom and 14 valence electrons in a Mo atom. Thus, the number of bands should be larger than 26 to calculate the LUMO energy. The corresponding electronic configurations for S and Mo atoms are shown as below,

S	[Ne]$3s^2 3p^4$
Mo	[Ar]$4s^2 4p^6 4d^5 5s^1$

In the Mo atom, the electronic configuration is $4d^5 5s^1$ rather than $4d^4 5s^2$, which is based on the Hund's third rule. The Hund's third rule claims that the system occupies the lowest energy when outermost subshell is empty, half-filled or full-filled.

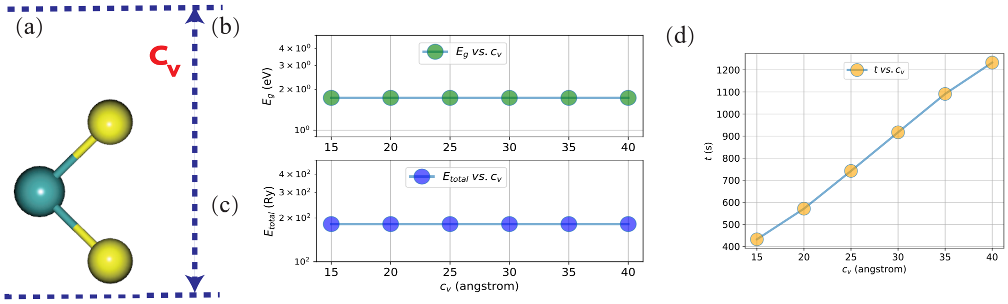

Figure 7.2: (a) Illustration of the vacuum size c_v which is larger than the pristine interlayer distance c. (b) Band gap E_g *vs.* c_v. (c) Total energy E_{total} *vs.* c_v. (d) Total CPU time t *vs.* c_v. K-points are 12 × 12 × 1. PPs are US with the PBE XC functional. Wave-function cutoff and charge cutoff are 200 Ry and 800 Ry, respectively.

As shown in Fig. 7.2, c_v has been tuned from 15 to 40 angstroms with a step size 5 angstroms. PPs for both S and Mo atoms are USPPs with Perdew-Burke-Ernzerhof (PBE) GGA functional.[100] The pseudization method is that of Rappe-Rabe-Kaxiras-Joannopoulos (RRKJ).[101] In Fig. 7.2 (b) and (c), it can be seen that both E_g and E_{total} remain at a steady level with respect to the increase of c_v. Precisely, E_{total} ranges from -181.581160 to -181.581161 Ry with accuracy to 6 decimals. In 7.2 (b), the y axis has been taken absolute values in order to be plotted in the logarithmic scale. E_g keeps the value of $1.7296eV$ in each calculation (the QUANTUM ESPRESSO output file only has four-decimal accuracy for Fermi energy, HUMO and LUMO). In Fig. 7.2

(d), it is clear that the calculation time increases linearly with respect to c_v, resulting from the increasing size of the unit cell (c_v is the height of the unit cell).

The most important information revealed in Fig. 7.2 is that E_g and E_{total} keep steady with increasing of c_v, suggesting the threshold of interlayer distance where the interlayer Van der Waals' force can be neglected can be set at $c_v = 15$ angstroms. Also considering the time cost of calculation, we finally set the dimension of the unit cell and corresponding atomic positions as follows (they will be reflected in the QUANTUM ESPRESSO input files),

a=3.169, c=20.000

Mo	-0.000158	1.829714	3.081000
S	1.584342	0.914720	1.515852
S	1.584342	0.914720	4.646148

With lattice parameter determined, we then calculate the electronic band structure of monolayer MoS$_2$, and show it in Fig. 7.3 (a) and (b). The PP, XC functional and K-points are same as for Fig. 7.2. The first Brillouin zone (BZ) of monolayer MoS$_2$ is hexagonal due to its hexagonal lattice in real space, which is depicted in Fig. 7.3 (a). The path with high symmetry points in the first BZ is chosen along $\Gamma - K - M - \Gamma$. b_1 and b_2 are basis vectors in the reciprocal lattice. The coordination of high-symmetry points and basis vectors in Fig. 7.3 (a) is shown as,

$$b_1 = \frac{4\pi}{\sqrt{3}a}(\frac{\sqrt{3}}{2}, -\frac{1}{2}, 0)$$

$$b_2 = \frac{4\pi}{\sqrt{3}a}(0, 1, 0)$$

$$\Gamma = (0, 0, 0) \qquad K = (\frac{2\pi}{3a}, \frac{-2\pi}{\sqrt{3}a}, 0)$$

$$M = (\frac{\pi}{a}, \frac{-\pi}{\sqrt{3}a}, 0) \qquad -K = (\frac{4\pi}{3a}, 0, 0)$$

where a is the lattice parameter with value 3.169 angstroms. The calculated band structure based on the above coordination is shown in Fig. 7.3 (c). It shows a direct band gap of 1.73 eV at the K valley, which is smaller than the value measured by photoluminescence (PL). The phenomenon that PBE functional underestimates the band gap of monolayer MoS_2 has also been observed by other researchers.[22, 97, 102] The corresponding reported band gap values are 1.59 eV,[22] 1.68 eV,[97] and 1.7 eV,[102] respectively.

Firstly, the PBE functional itself is an approximate analytic expression. Perdew *et al* elucidated how to construct a simple GGA functional by adding three extra conditions to correlation energy and four conditions to exchange energy respectively.[100] They also discussed the evolution of the gradient contribution in terms of density variation under both slowly and rapidly varying limits and compared it with LDA approximation.[100] As shown in Perdew's original paper, the PBE XC functional underestimated or overestimated the molecular atomization energies with a mean abs. error of 7.9 $kcal/mol$.[100]

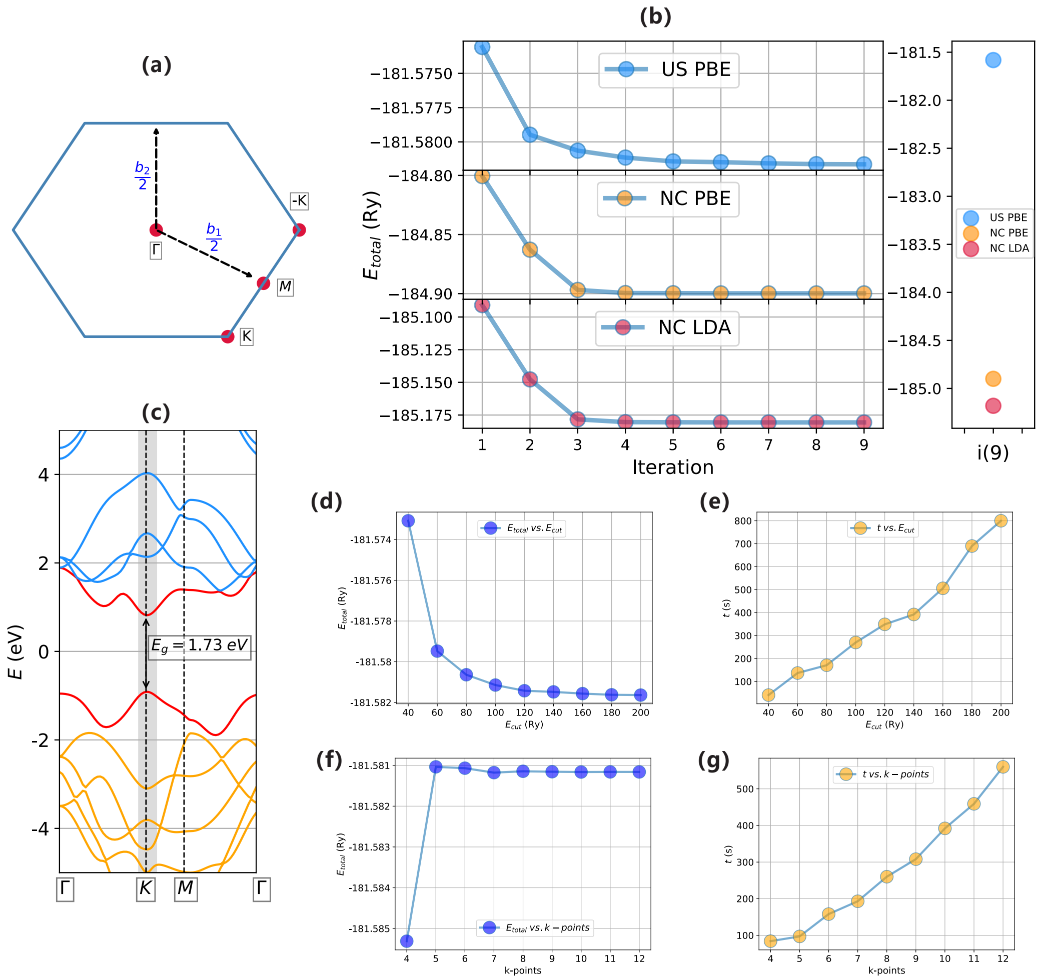

Figure 7.3: (a) Illustration of the first BZ of monolayer MoS_2 with high symmetry points and reciprocal basis vectors shown. (b) Comparison of the total energy among three different PPs. For all of them, k-points sampling is $8 \times 8 \times 1$. The x axis is the iteration number, and the subfigure on the right compares the final total energy at the $9th$ iteration. (c) Band structure of monolayer MoS_2 shows a band gap value 1.73 eV with USPP and PBE functional. The cutoff for WF and charge are 120 and 480 Ry, respectively. (d) and (e) show typical trends of E_{total} and t with the increasing of E_{cut}. (f) and (g) show how E_{total} and t change when k-point density increases. In (d) to (g), PPs are US with PBE functional.

Secondly, due to the peculiar spatial localization of d orbitals, strong spin-orbit coupling effect and spin polarization effect in transition metals,[16] the physics of transition metals and their compounds is not trivial. The most famous example is the Mott insulators, such as NiO and CoO, which are predicted to be conductors by band theory, are insulators measured in experiments.[103] The contradiction between theory and experiment lead to the development of the Hubbard model, which describes the strongly correlated electron gas and can be understood as adding a correlation potential into the tight-binding Hamiltonian.[104] The Hubbard term has also been included in modern DFT calculations, where it is called DFT+U. Thus, we believe that the underestimation in the band gap is also due to the above localization properties of the d orbital electrons on the Mo atom.

In Fig. 7.3 (b), we compare the total energy from three different PPs. For all of them, the calculation converges within nine iterations. It can be seen that the total energy from the NCPP is about 3 Ry lower than that of the USPP. Within the NC scheme, the PBE and LDA functionals give rather close results with -184.9 and -185.2 Ry. In Fig. 7.3 (d) (US PBE), we study the relation between E_{total} and E_{cut}. It is clear that E_{total} converges rapidly to -181.582 Ry after E_{cut} is larger than 120 Ry, suggesting E_{cut} = 120 Ry can be set in the following calculations to help saving time, and a larger E_{cut} is not necessary. In Fig. 7.3 (f), E_{total} also converges to -181.581 Ry when the k-point sampling is larger than $8 \times 8 \times 1$. Hence, the same conclusion can be made that the BZ mesh grid can be chosen as $8 \times 8 \times 1$ in the following calculations. Fig. 7.3 (e) and (g) show the same and reasonable trend that the calculation time is proportional to the E_{cut} or k-point sampling. This is because the larger the E_{cut}, the more plane waves are needed. The more sampling points in the BZ, the more calculation is needed also.

Incidentally, the mixing beta (β) is set at 0.3 for all the calculations in this chapter to ensure the consistency of calculation cost. β is a damping parameter to prevent the instability of the charge density by considering old charge densities from previous iterations.[50] $C^{(n)}$ is the charge density in the nth iteration.

$$C^{(n+1)} = \beta C^{(n)} + (1 - \beta) C^{(n-1)} \tag{7.2}$$

In Table. 7.1, we compare the band gap values from various works. From the experimental point of view, the most common way to measure the band gap is using photoluminescene (PL). In Chapter 6, the measured PL peak of monolayer MoS_2 is located at 1.84 eV in Fig. 6.4. In published works, the measured band gap ranges from 1.79 to 1.89 eV.[28, 105, 70, 106] Another approach to measure the band gap is Scanning tunneling spectroscopy (STS), in which the measured value is the sum of the optical band gap and exciton binding energy. Thus, in ref [107], the measured gap is 2.15 eV that is larger than values measured by PL. Regarding theoretical works, the most used XC functionals are LDA, PBE and HSE06. In refs [97, 108], HSE06 has been used. The HSE06 functional is a typical hybrid functional, which has a common expression, $E_{XC} = aE_x^{HF} + (1-a)E_x^{PBE} + E_c^{PBE}$. The idea of the hybrid functional is to mix various functionals together to remove the error, since some functionals underestimate the energy and some overestimate it. The hybrid functional plays an important role in the DFT Jacob's Ladder, and it does give better results than LDA or GGA in some cases.[109] Some other popular hybrid functionals are B3LYP and OLYP.[110, 111].

(*This paragraph is the caption for Table 7.1.* Due to the size of Table 7.1, we arrange an entire page to show it.)

Table 7.1:Summary of the band gap values from both experimental and theoretical publications. All band-gap values are in the unit of eV. The unit of c_v is angstrom. WF stands for wave function. The k-points refers to the mesh grid for Brillouin zone sampling. β is the mixing factor for self-consistency. HSE06 is a hybrid functional.[112] Areas highlighted in yellow are results calculated by the author. In ref [108] and [22], the researchers applied different XC functionals, thus they are isolated out by gridlines in order to avoid formatting disorder.

Table 7.1: Summary of band gap values from publications and our work.

Experiment

Method	Value(eV)	Note
Photoluminescene (PL)	1.84	Chapter 6, Fig. 6.4
PL	1.85	ref [28]
PL	1.89	ref [105]
PL	1.79	ref [70]
PL	1.85	ref [106]
Scanning tunneling spectroscopy (STS)	2.15	ref [107] Optical band gap (1.93) + exciton binding energy (0.22)

Theoretical claculation

Method	PP	Value(eV)	Note
DFT-PBE	US	1.86	This work
DFT-PBE	NC	1.89	Cutoff WF=30 Ry, cutoff charge=150 Ry, k-points 12 × 12 × 1
DFT-LDA	NC	1.90	
DFT-PBE	US	1.72	This work
DFT-PBE	NC	1.73	Cutoff WF=200 Ry, cutoff charge=800 Ry, k-points 12 × 12 × 1
DFT-LDA	NC	1.73	
DFT-LDA		1.86	ref [113]
DFT-LDA		1.89	ref [114]
DFT-PBE		1.70	ref [102]
DFT-PBE		1.93	ref [115]
DFT-PBE		1.65	ref [108]
DFT-HSE06		2.12	
DFT-LDA		1.87	ref [116]
DFT-LDA		1.67	ref [22]
DFT-PBE		1.59	
DFT-GGA		1.75	ref [17]
DFT-PBE		1.80	ref [21]
DFT-HSE06		2.23	ref [97]
GW		2.84	ref [117]

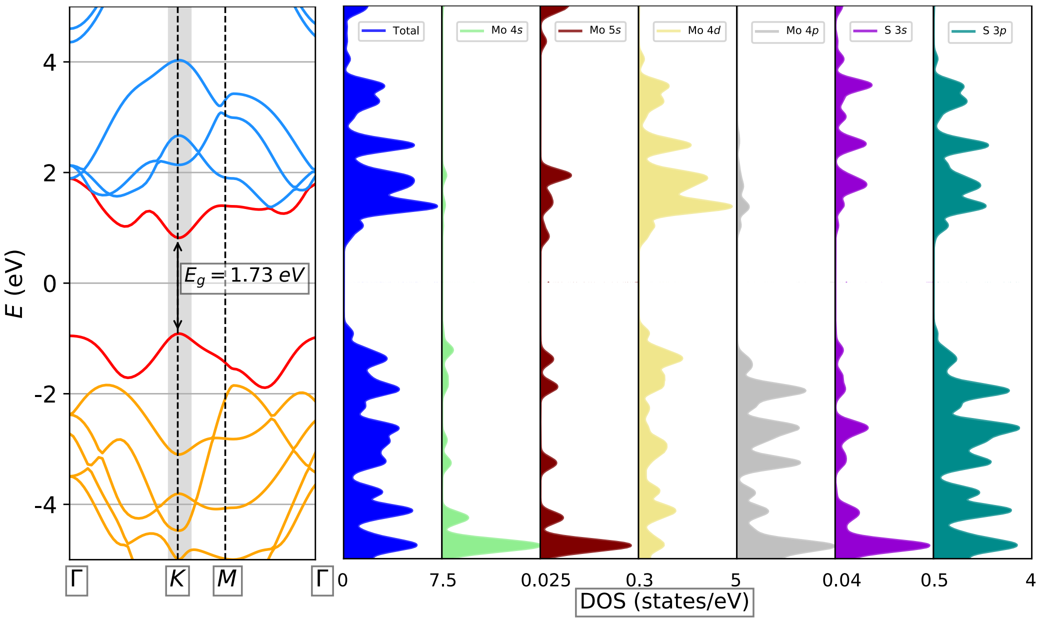

Figure 7.4: Band structure and PDOS of monolayer MoS_2. The total DOS is placed on the left, followed by PDOS of orbitals from Mo and S atoms. The PDOS of S $3s$ (or $3p$) orbital is the sum of $3s$ (or $3p$) orbitals from two S atoms in the same unit cell. The x axis in the PDOS plot is the range of DOS for each orbital. For example, the total DOS ranges from 0 to 7.5 $states/eV$, and Mo $4s$ ranges from 0 to 0.025 $states/eV$.

In Fig. 7.4, we calculated the total density of states (DOS) and projected density of states (PDOS) of pristine monolayer MoS_2 by using the *dos.exe* and *projwfc.exe* packages in the QUANTUM ESPRESSO. The figure filled in blue is the total DOS, showing a clear band gap of 1.73 eV. The following figures arranged in sequence are PDOS plots which include four valence orbitals from one Mo atom and two valence orbitals from two S atoms. In the last two subfigures, we add the contribution of $3s$ and $3p$ PDOS from the two S atoms together, because there are two S atoms in one unit cell. The x axis represents the value for each orbital. For example, the total DOS ranges from 0 to 7.5 $states/eV$. It can be seen that Mo $4d$ and S $3p$ have a significant contribution to the total DOS, because their PDOS ranges are much larger than those of other orbitals. This result is also consistent with Eugene's work.[118] If we compare the sum of four orbitals in the conduction band from Mo and the sum from S atoms, it can be found that one Mo atom occupies a great portion of the total DOS than the two S atoms, which has also been observed by Cao *et al.*[119] It is reasonable that Mo $4s$ and $4p$ have a small percentage in the total DOS in this energy range, because they are inner shell orbitals compared with $5s$ and $4d$ orbitals.

Moreover, the large portion of Mo $4d$ orbital in the total DOS is exactly what we expect. Because the larger PDOS the d orbital has, the more significant spin-orbit coupling it shows. The spin-orbit coupling originated from Mo $4d$ orbitals in monolayer MoS_2 leads to new physics that graphene doesn't have. For example, the spin-orbit coupling in monolayer MoS_2 further causes the coupling between spin and valley degrees of freedom, which introduces more possible combinations of valley and spin indices in the photoexcitation process.[18]

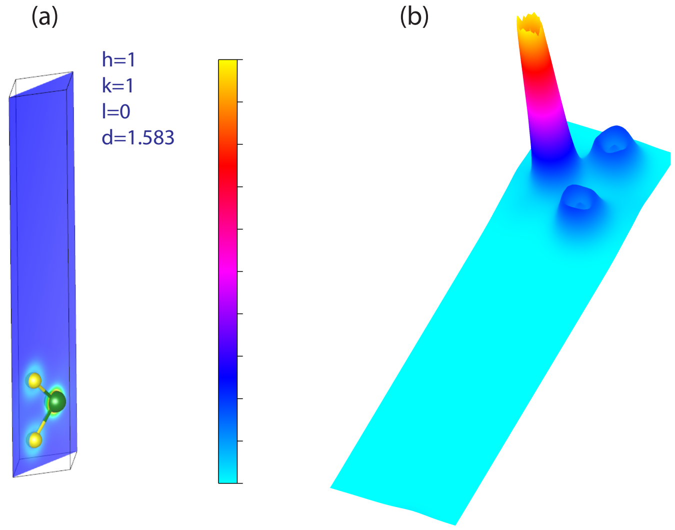

Figure 7.5: Charge density illustration of a monolayer MoS_2 unit cell with lattice parameters determined in the previous discussion. (a) shows the lattice plane where all three atoms are. (b) depicts the bird's-eye view of the charge density. hkl are Miller indices and d is the distance between the plane and origin.

In Fig. 7.5, we study the charge density of monolayer MoS_2 with the chosen unit cell in the previous discussion. In (a), the lattice plane is determined with Miller indices $h = 1$, $k = 1$ and $l = 0$, and the distance between the plane and origin is $d = 1.583$ angstroms. In (b), it is clear that the charge density of a Mo atom is significantly higher than that of S atoms. This result is within our expectation, because in Fig. 7.4, we already see that Mo atom occupies a greater percentage in the total DOS, leading to the intuition that Mo atom also has larger charge density than S atoms. A better explanation is that the number of valence electrons in a Mo atom (14) is more than double that of a S atom (6). Please note that the charge density and DOS are two different ways to analyse an electron system.

So far, we have discussed the electronic properties of monolayer MoS_2 from lattice parameters, band structure, DOS, PDOS and charge density. Now we are going to dig out the same information from the oxygen-plasma-treated MoS_2 system. The first job is to construct the unit cell of the system. The idea of the construction should be built on the experimental observation in *Chapter* 6, especially Figs. 6.2 and 6.3. More information from the literature is also necessary.

In ref [70], the authors propose two possible interactions between oxygen plasma and monolayer MoS_2. One is physical absorption of O atoms on the MoS_2 surface. Another one is the chemical bonding between O and Mo atoms, namely the filling of S vacancies by O atoms. They further prove that the chemical bonding between O and Mo is strong and can introduce heavy p doping in MoS_2. However, the authors didn't show AFM height profiles of the samples before and after plasma irradiation.[70] In this work, we have shown that the sample becomes thicker after 2s of O_2 plasma irradiation in Fig. 6.2. The same phenomenon has also been observed by Zhu *et al.* They find that the surface roughness increases with increasing exposure duration in the RF O_2 plasma.[35] Azcatl *et al* have shown that ultraviolet-ozone can remove the carbon contamination from the MoS_2 surface and cause a formation of weak bonding between S and O atoms.[71] This surface adsorption can be regarded as a doping strategy to functionalize MoS_2.[74] Various adsorption configurations with adatoms from Group 1^{st} to 7^{th} have been studied to show that surface adsorption can modulate the electronic properties of MoS_2 significantly.[74] Moreover, Qi *et al* also systematically study the role of chemisorption and physisorption separately from *in-situ* electrical measurements. However, their chemical species is oxygen gas rather than oxygen plasma.[72]

Based on the above discussion, three possible interactions between oxygen atoms and monolayer MoS_2 have been shown in Fig. 7.6. (a) shows a pristine MoS_2 unit cell. (b) and (c) depict chemisorption and physisorption respectively. (d) illustrates a typical sulphur vacancy.

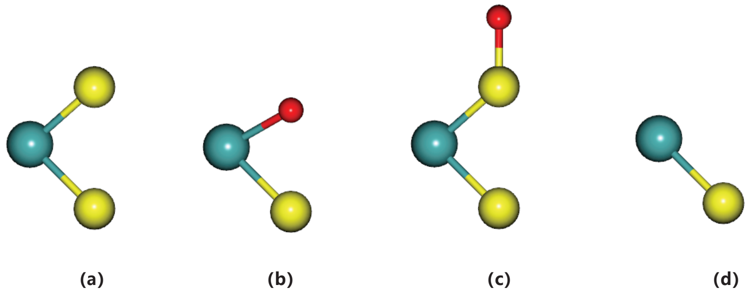

Figure 7.6: Unit cells under different adsorption configurations of oxygen-plasma-treated monolayer MoS_2. (a) Unit cell of pristine monolayer MoS_2. (b) An oxygen atom fills a sulphur vacancy. The formation of the chemical bond between O and Mo is called chemisorption. (c) Physisorption of an O atom. (d) A typical sulphur vacancy. Mo atoms are in green, S atoms are in yellow and O atoms are in red. The color style of atoms is same in the rest of figures.

We attribute the thickness increasing observed in Fig. 6.2 to physisorption. To exclude the possibility of chemisorption, we used DFT to calculate the bond length between O and Mo under *relax calculation* scheme. Corresponding results are shown in Fig. 7.7. PPs for oxygen, sulphur and molybdenum atoms are all USPP based on RRKJ pseudization method with PBE XC functionals.[101] Cutoffs for wave function and charge are 120 and 480 Ry, respectively.

In Fig. 7.7 (b), it can be seen that relax calculation converges at 9^{th} iteration in the case of physisorption where four atoms are in the unit cell. In (e), seven iterations are required to reach convergence in the case of chemisorption. Total energy E_t for two situations are shown in (c) and (f). E_ts for physisorption and chemisorption are -213.865 Ry and -192.986 Ry respectively. It is reasonable that E_t^{phy} is lower than E_t^{che} due to there are more atoms in the unit cell of physisorption.

In the output files of relax calculation, atomic positions can be read. The atomic positions are extracted from the final iteration, which minimizes the total force in the unit cell.

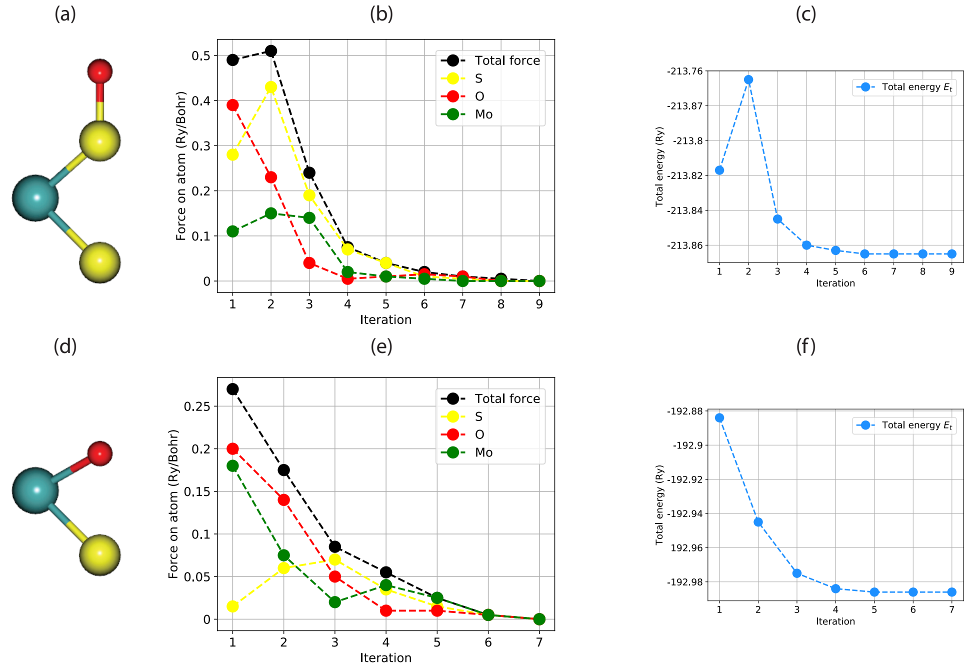

Figure 7.7: Relax calculation for two types of unit cells. (a) and (d) are unit cells for physisorption and chemisorption. (b) and (d) are calculated forces on atoms in the unit cells at each iteration. (c) and (f) show total energies E_ts converge with respect to the number of iterations.

In Table. 7.2 and Fig. 7.7, Hellman-Feyman force threshold is set at 10^{-4} Ry/Bohr. From the atom positions shown as below, the $Mo - O$ bond length is 2.138 angstroms in the case of chemisorption, which is shorter than the $Mo - S$ bond length in the pristine monolayer MoS_2. Thus, we can conclude that the chemisorption can't cause thickness to be increased. And it is clear that in the right column of Table. 7.2 that physisorption can cause thickness increase due to the formation of bonds between O and S atoms. Moreover, Fig. 7.7 and Table. 7.2 set up the foundation for further super-cell calculation for post-treated MoS_2. In the following discussion, atomic positions in Table.

7.2 will be used to do calculations.

So far, we already have three types of unit cells to construct a super cell. As shown in Fig. 7.6, (a), (c) and (d) (pristine MoS_2, physisorption and vacancy) are three types of building block in super cells. Let's start from a 2×2 super cell.

Table 7.2: Optimized atom positions in two types of unit cell. Chemisorption is on the left and physisorption is on the right.

Chemisorption				Physisorption			
Mo	-0.000158	1.829592	3.240155	Mo	-0.000158	1.829578	3.140954
S	1.584342	0.914793	1.656471	S	1.584342	0.914768	1.574874
O	1.584342	0.914769	4.346374	S	1.584342	0.914764	4.674063
				O	1.584342	0.914764	6.152884

In Fig. 7.8, we illustrate a typical 2×2 oxygen-plasma-treated monolayer MoS_2 supercell. (a) demonstrates a simplified schematic of the supercell with unit cells labelled by different colors. Unit cells of physisorption, pristine MoS_2 and sulphur vacancy are labelled in red, yellow and gray. (b) shows the supercell in ball-and-stick model. There are 4 unit cells in the supercell, and all of them are also labelled by numbers. Labelled numbers tell the location of the unit cells in the supercell. For example, the 3^{rd} unit cell (vacancy) is located at southwest in (b), and it also appears in the bottom left corner in (a). The simplified schematic with color notation will be used in the following discussion.

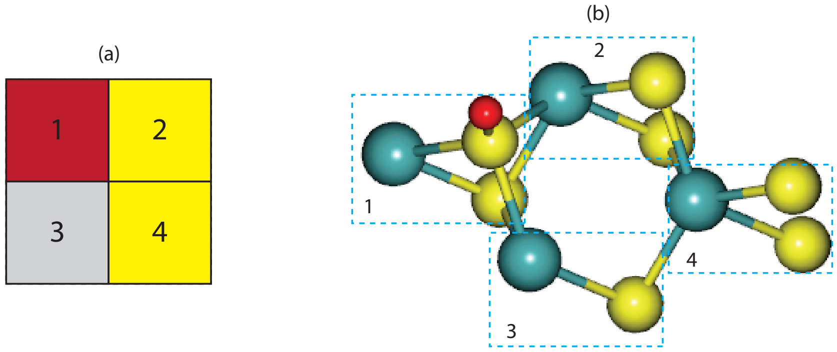

Figure 7.8: A 2 × 2 oxygen-plasma-treated monolayer MoS_2 supercell. (a) is a simplified schematic of the supercell. Red, yellow and gray squares represent physisorption, pristine MoS_2 and sulphur vacancy respectively. (b) shows a 2 × 2 supercell with a combination of physorption, pristine MoS_2 and sulphur vacancy. Numbers (from 1 to 4) are used to label unit cells. Spacial distribution of labelled unit cells are consistent in (a) and (b).

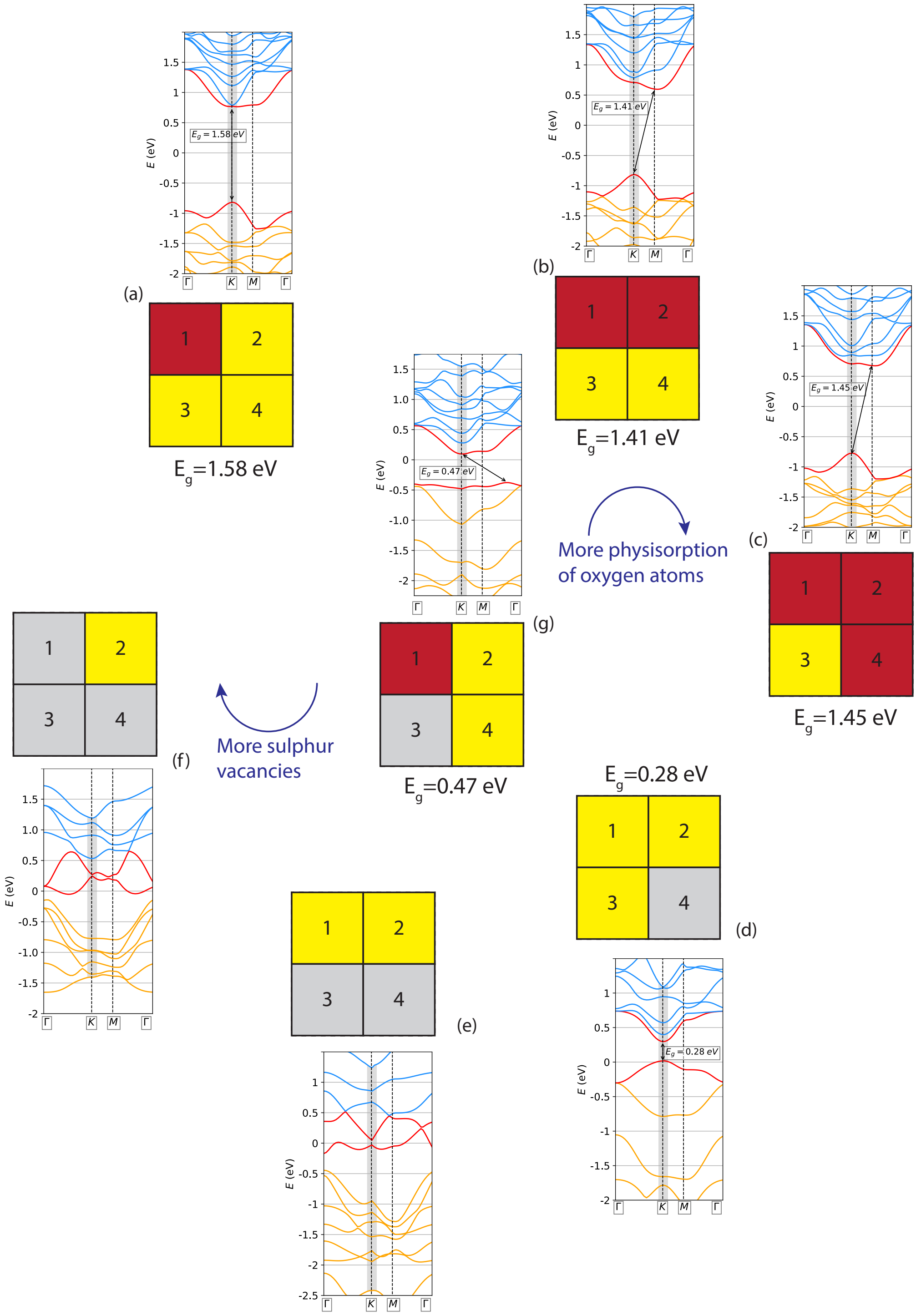

Figure 7.9: Band structures of 2 × 2 supercells with different combinations of pristine MoS_2, sulphur vacancy and physisorption. Totally, seven types of combination are shown. The upper (lower) three figures show evolution of band structure with the increasing of portion of physisorption (sulphur vacancy). In the middle, it is a combination including all three types of unit cell.

In Fig. 7.9, we discuss the evolution of the band structure with respect to the portion of physisorption or sulphur vacancy. In the upper (lower) three figures, the portion of physisorption (sulphur vacancy) increases along the clockwise direction. The color notation used here is defined in Fig. 7.8.

In the upper three figures, firstly, it can be seen that the direct band gap becomes indirect band gap when the percentage of physisorption is over 50%. It is also known that the pristine monolayer $\mathrm{MoS_2}$ is a direct band gap semiconductor. In Fig. 7.9 (a), the sample still has a direct band gap when 25% of the supercell is transformed into physisorption after plasam treatment. However, the band gap quenches to 1.58 eV which is 0.15 eV smaller than the calculated band gap of pristine monolayer $\mathrm{MoS_2}$ in Fig. 7.3. Moreover, in (b) and (c), the band gap value keeps dropping to 1.41 and 1.45 eV when 50% and 75% percent of the supercell are covered by oxygen atoms. So far, the adhered oxygen atoms cause two effects (direct band gap to indirect band gap and quenching of band gap value).

In the lower three figures (d), (e) and (f), combination of only two types of unit cell are discussed. In (d), when there is one S vacancy in the supercell, the band gap significantly quenches to 0.28 eV but still remains a direct band gap. In (e), when one more S vacancy is added in, there is nearly no band gap in the system. Until 75% of the system is defective shown in (f), the conduction and valence band already overlap, namely the system is a conductor rather than a semiconductor. This evolution is reasonable. Because when more and more top-layer S atoms are removed by plasma, molybdenum atoms start to dominate the system. Due to the conductivity of Mo, the system gradually transforms into the conductor phase with more and more S atoms removed. (One point needs to be emphasised: Results above need to be tested using larger supercells, including relaxation.)

We don't calculate the band structure of the system where all four squares are physisorption (red) or vacancy (gray), because that circumstance is unrealistic. One can't ideally cover the pristine ML $\mathrm{MoS_2}$ with oxygen atoms on the surface or remove all top-layer S atoms by plasma treatment. At least, from Figs. 6.2 and 6.3, what we have observed is the existence of both physisorption and vacancy. Technically speaking, both bombardment effect and physisorption play important roles in the plasma irradiation, which leads to the combination of squares in (g).

Figure 7.9 (g) is a more general yield of ML MoS_2 treated by oxygen plasma. We design two yellow squares (pristine) in it due to the fact of most areas of the sample not being modified in the 2s rapid plasma treatment. In (g), it shows an indirect band gap with $E_g = 0.47\ eV$, which is within our expectation. Because from (b) and (c), we already observe that O adatom can cause the formation of an indirect band gap. From (d) to (f), we already infer that the elimination of top-layer S atoms results in better conductivity. Thus, (g) tells that the combination of physisorption and sulphur vacancy integrates effects from both of them.

More importantly, the curvatures of band edges (CB or VB) are different in different combinations. The curvature of the band edge reflects the effective electron (hole) mass due to $m_e^* = \hbar^2(\partial^2 E/\partial k^2)^{-1}$. In (a) to (c), it can be observed that the curvatures of conduction band edges are more flat compared with Fig. 7.3, suggesting heavier effective electron mass caused by adhered oxygen atoms. On the other hand, in (d) to (f), curvatures of valence band edges are also more flat than Fig. 7.3, indicating heavier effective hole mass caused by sulphur vacancies. Finally, both of effects that effective masses of electron and hole increase are reflected in (g).

The observation in (g) is important, because it gives insight into how to design band-structures based on 2D MoS_2. Band-structure engineering is an important topic in semiconductor industry. The most common band-structure engineering technique in modern silicon-based semiconductor industry is doping.[29] For example, by doping silicon with boron or phosphorus, we can obtain p-type or n-type silicon which can be used to fabricate CMOS.

Finally, I would like to combine the site-specific modification technique[38] (mentioned in Chapter 6.2) and results obtained in Fig. 7.9 together. In Figs. 6.3 (the TEM image) and 7.9, patterns containing three types of unit cell will appear in the real system randomly because the sample is globally treated by oxygen plasma. And the fluctuation in plasma will also cause non-uniform treatment on the sample surface leading to a less-controllable yield. If the site-specific modification with an accurate prediction of plasma energy distribution can be utilized to locally treat 2D MoS_2, the yield of physisorption or sulphur vacancy can be highly controlled due to their different energy requirements. Once the two types of yield can be controlled, the band structure engineering for 2D MoS_2 can be significantly optimized.

7.2 Magnetism and density of states

In the last section, we mainly discuss electronic properties of pristine and oxygen-plasma-treated ML MoS_2. In this section, we are going to study their magnetic properties by DFT.

Cao *et al* find that Mo adatoms can introduce local magnetic moments and strong spin polarization near the Fermi energy.[119] They also find that neither Mo nor S vacancies can introduce magnetism.[119] The phenomenon that defects can't introduce magnetism or spin-polarized state has also been found by Wang *et al.*[120] They apply GGA+U calculation to study the defective system, and no splitting is observed in the DOS results. Since MoS_2 is not a strongly-correlated electron system, GGA+U method doesn't provide much difference from the GGA method.[120]

Two-dimensional TMDs with adatoms have also been studied. He *et al* report magnetic properties of ML MoS_2 with nonmetal-atom adsorption.[121] They find that oxygen adatoms on the ML MoS_2 surface can't introduce magnetism. Ma *et al* study various 2D-TMD systems such as $MoSe_2$, $MoTe_2$ and WS_2. They find that adding oxygen adatoms can't introduce magnetism into these systems.[122]

Moreover, Yan *et al* study the magnetism of pristine MoS_2 powder, exfoliated 2H MoS_2 nanosheet and Li-MoS_2 hybrid systems experimentally and theoretically.[123] They show that pristine MoS_2 powder exhibits a diamagnetic behaviour at a temperature of $T = 2\ K$ when the magnetic field ranges from -6 to +6 $\times 10^4\ Oe$. However, after exfoliation, 2H MoS_2 nanosheet presents paramagnetism under the same measurement conditions. They also apply DFT method to calculate the PDOS of Mo $4d$ orbitals,[123] and their results are consistent with those of Cao, Wang, and Ma *et al.*[119, 120, 122]

In Fig. 7.10, calculated results concerning magnetism are shown. PPs are same as those PPs used in the last section. The k-point grid is set to $8 \times 8 \times 1$. The cutoffs for wavefunction and charge are 100 and 500 Ry, respectively. Spin polarization is set as collinear. Both (a) and (b) are consistent with results from other works.[119, 120, 122, 123] In (a) and (b), it can be seen that the densities of states of spin up and down are symmetric with respect to the x axis, indicating the system is not ferromagnetic (some papers use the term nonmagnetic).

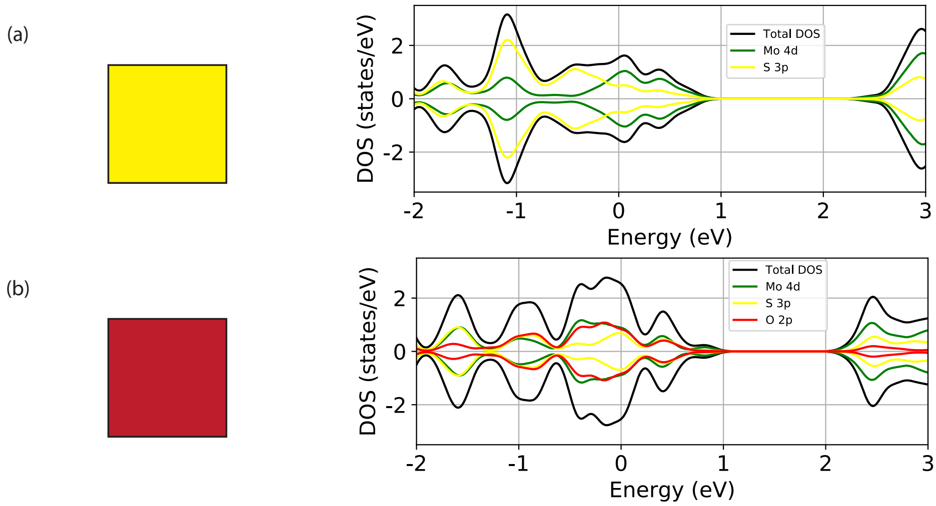

Figure 7.10: (a) is the spin-dependent DOS of pristine monolayer MoS_2. (b) is the spin-dependent DOS of physisorption-type unit cell. Each calculation is based on the unit cell (1×1) shown by color notation.

To further classify whether the system is antiferromagnetic or paramagnetic, one can analyse in two ways. One way is experimental measurement in magnetic field, paramagnetic materials will show a positive magnetization in a magnetic field with a rather small susceptibility about 10^{-5}. However, antiferromagnetic materials will show negative susceptibility in an external magnetic field.[124] Yan *et al* already show that exfoliated MoS_2 is paramagnetic by experimental measurement.[123] Another convenient way is based on the electronic configurations of the material. The electronic configurations of Mo and S are shown in the last section. If there are unpaired electrons in the unit cell, and their spins are parallel, then the material is paramagnetic. In a Mo atom, there are 6 unpaired electrons due to the Hund's third law. And there are 2 unpaired electrons in a S or O atom. Thus, it is clear that monolayer MoS_2 or physisorption-type unit cell is paramagnetic.

Moreover, Fig. 7.10 is also consistent with Fig. 7.4 and other works[119, 120, 122, 123] in terms of the magnitude of each orbital. It can be seen that in (a) and (b), the Mo $4d$ orbital occupies a large portion of the total DOS in the conduction band. It is reasonable because Mo $4d$ orbital has more d orbital electrons than

S or O atoms and a larger spatial distribution. In (b), it can be seen that O $2p$ orbital has a small contribution to the CB, but a significant contribution to the VB. This is because electrons of an O atom are highly localized due to the small atomic radius.

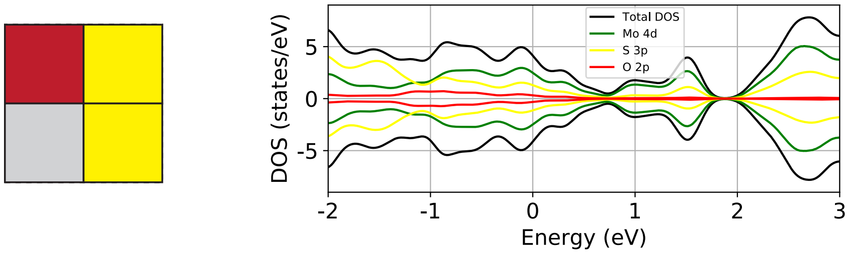

Figure 7.11: Spin-dependent DOS for a 2 × 2 super cell, denoted by color notation shown on the left. Spin up and down DOS for Mo $4d$, S $3p$ and O $2p$ are shown on the right.

Figure 7.11 shows the calculated spin-dependent DOS for a 2 × 2 super cell containing three types of unit cell. The result is within our expectation, because from the calculation shown in Fig. 7.10 and other works[119, 120, 122, 123], we already know that neither vacancy nor oxygen adatoms can introduce a ferromagnetic phase. Thus, it is reasonable that their combination can neither introduce magnetism. In Fig. 7.11, it also shows that the Mo $4d$ orbital make a significant contribution to the conduction band, and the valence band is mainly dominated by S and O atoms.

7.3 Spin-orbit coupling effect

We further study the spin-orbit coupling effect in pristine ML MoS_2 and oxygen-plasma-treated ML MoS_2. In the spin-orbit calculation, full-relativistic norm conserving PPs with the PBE XC functional for Mo, S and O atoms are used.[125] K-points is set to 8 × 8 × 1. The cutoff for wavefunction and charge are 100 and 500 Ry, respectively. Spin polarization is set as non-collinear.

Theoretically speaking, we may ask how does SOC affect the system? Before considering SOC, the Hamiltonian is diagonal in the energy representation. And after adding the SOC term into the total Hamiltonian, H_{total} becomes block diagonal which can be easily seen from the tight-binding Hamiltonian. The SOC strength can be defined by the difference of eigenvalues of the two blocks. The spin-orbit coupling Hamiltonian is

$$H_{SOC} = \sum_{\alpha} \frac{\lambda_\alpha}{\hbar^2} \boldsymbol{L_\alpha} \cdot \boldsymbol{S_\alpha} \tag{7.3}$$

where $\lambda_\alpha/\hbar^2$ is atomic spin-orbit coupling strength in the unit of $eV/\hbar^2$. $\boldsymbol{L_\alpha}$ and $\boldsymbol{S_\alpha}$ are the atomic orbital angular momentum operator and spin operator respectively. The subscript α indicates each atom in the calculated unit cell.

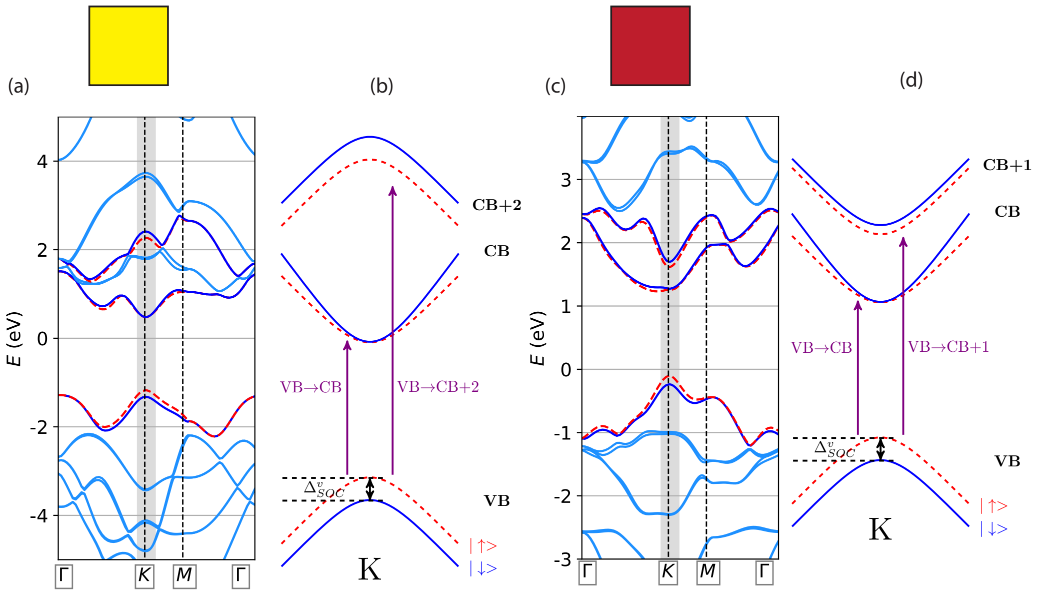

Figure 7.12: (a) and (c) are band structures considering SOC for a pristine ML MoS_2 unit cell and physisorption-type unit cell, respectively. (b) and (d) are the optical transitions with SOC caused band splitting at the **K** valley. Red dashed lines refer to spin-up bands and blue solid lines are spin-down bands. **CB+1** or **CB+2** stands for the second- or third- conduction band.

Figure 7.12 shows the results of band-structure calculation considering SOC. In (a), we can see the band splitting happens in both the VB and CB. The spin-up band has a higher energy than that spin-down band at the **K** valley at the valence-band edge. However, in the conduction-band edge (CB) and the third conducton band (CB), the spin-up electron has lower energy than the spin-down electron at the **K** valley. This phenomenon is consistent with other researchers' work.[17, 22, 23, 126] (b) is a simplified illustration corresponding to (a). The band splitting caused by SOC is highlighted in (b). Red dashed lines refer to spin-up bands and blue solid lines are spin-down bands. The energy split in the valence band at **K** valley is denoted by Δ^v_{SOC}.

In Fig. 7.12 (c), we calculate the band structure based on the physisorption-type unit cell. The band splitting in the VB still appears at the **K** valley. However, compared with (a), the band splitting in CB happens at the second conduction band (CB+1) rather than CB. Thus, the order of the band which is splitted can be changed by O adatom. It is mainly because O adatom can cause the band structure to change, which has been found in Fig. 7.9. Here the order refers to CB, CB+1 or CB+2.

Table 7.3: Calculated SOC strength of pristine and physisorption-type MoS_2 are shown on the left. Results from published work is shown on the right.[127]

This work	λ_{SOC} (meV)
Pristine MoS_2	73
Treated MoS_2	67

Ref [127]	λ_{SOC} (meV)
Pristine MoS_2 (PT)	87
Pristine MoS_2 (TB+SOC)	86

We further quantitatively study the SOC strength λ_{SOC}. The SOC strength is defined as $\lambda_{SOC} = \Delta^v_{SOC}/2$.[17] Δ^v_{SOC} is extracted at the **K** valley.

As shown in Table. 7.3, our results (73 meV) are consistent with those of Kosmider *et al* (87 meV) in terms of pristine ML MoS_2.[127] Two methods (perturbation theory and tight binding + SOC) are used in Kosmider's work and give a consistent result. In the physisorption-type unit cell, λ_{SOC} becomes 67 meV, that is 6 meV smaller than the untreated unit cell. It is a rather small change, indicating that O atom doesn't play an important role in the SOC effect. And it is known that in the 2D-TMD system the transition metal plays an important role in SOC due to the large orbital quantum number in the d orbital.[17]

The results in this section give insights into the potential for 2D-TMD based valley electronics and spin filters. We observe that oxygen adatoms introduced by oxygen-plasma treatment can modify the band structure, leading the order of the splitted band to be changed. Regarding valley electronics, a changed order of the splitted bands cause a more complex selection rule for photoexcitation, leading to a more complex spectrum of emitted circularly polarized light.[18] In terms of spin filters, in a 2D-TMD system, the electron transmission in a magnetic heterostructure depends on the potential barrier, valley and spin indices.[45, 23, 24] Thus, a changed band structure caused by plasma treatment can modulate the transmission. A more detailed discussion is provided in Chapter 10.

In this Chapter, we applied DFT to study the electronic and magnetic properties of oxygen-plasma-treated monolayer $\mathrm{MoS_2}$. After treatment, lattice parameters of physisorption-type unit cell are optimized by a *relax* calculation. We consider three types of unit cell, which are proposed based on our experimental observation shown in the Chapter 6. We further combine the three types of unit cell to make various 2×2 super cells. By calculating their band structures, we find that sulphur vacancy can cause significant quenching of the band gap and that oxygen adatoms can make the direct band gap an indirect band gap. Moreover, from the spin-dependent DOS, we also find that neither sulphur vacancy nor oxygen adatom can introduce a ferromagnetic phase in to ML $\mathrm{MoS_2}$, which is consistent with others' work. Regarding spin-orbit coupling, our calculated SOC strength of pristine $\mathrm{MoS_2}$ is consistent with others' work. An oxygen adatom can cause the location of band splitting to change, which is attributed to the modification of band structures by oxygen adatoms.

Chapter 8

Transfer matrix method for electron transport in MoS_2/MoO_x heterostructures

Plasma modification has attracted interest and been widely employed to treat 2D materials in order to extract new physics properties and develop potential applications due to its feature.[34, 68, 89, 128, 129] In Chapter 6 and 7, we have discussed the physisorption-type surface modification of ML MoS_2 by oxygen-plasma treatment. In this section, we are going to study the chemisorption-type modification, namely the chemical interaction between MoS_2 and oxygen plasma and how it causes a new phase to be generated in the system.

8.1 Device structure

Figure. 8.1 (a) shows the fabrication method used to obtain MoS_2/MoO_x heterostructure nano devices. The subscript x ranges from 2 to 3. The reason that we define the proportion of oxygen atoms as x is due to the difficulty of conducting isotropic plasma treatment on the surface. Monolayer MoS_2 samples can be obtained by mechanical exfoliation or chemical vapor deposition. After doing spin coating, a polymethylmethacrylate film will cover the sample. Then, we use electron beam lithography (EBL) to make patterns on the sample, and develop the sample to get two open windows. Then, we utilize an oxygen plasma to treat the sample to get MoO_3.[35, 89] We then expose the sample in H_2 to transform MoO_3 into MoO_2.[89] It is necessary to do the spin coat again to protect one of the two windows from being exposed in H_2. For simplicity, we just sketch the spin coat and EBL once in Fig. 8.1.

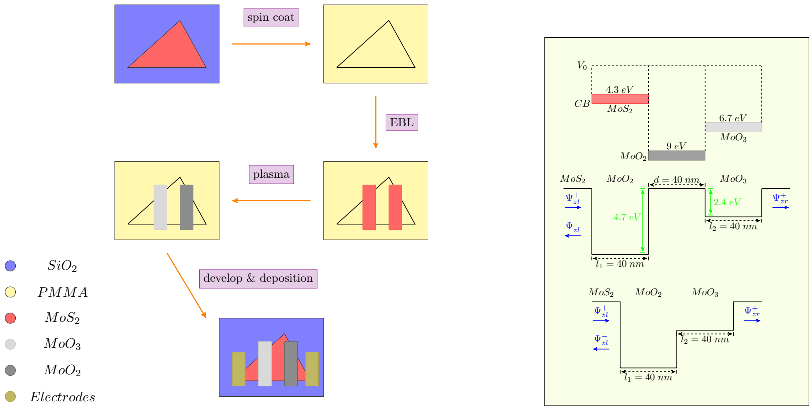

(a) (b)

Figure 8.1: (a) The flow chart of the fabrication method based on e-beam lithography. (b) An illustration of the band structures of MoS_2, MoO_2 and MoO_3 and the conduction band offset in their heterostructures.

Since the analysis of electron transport in a finite superlattice was done by Tsu and Esaki,[130] the resonant tunneling diode has been intensively studied both experimentally and theoretically.[131, 132, 133, 134, 135] Regarding its theoretical framework, the commonly used method is the transfer matrix method, which is a general method to deal with second-order differential equations.[136] Here, the conservation of momentum along a certain direction causes the breakdown of the conservation of the kinetic energy component due to the variation of effective mass of electron, suggesting that the coupling between transverse and longitudinal components needs to be considered.[134]

There are three similarities between traditional semiconductor superlattices and MoS_2/MoO_x heterostructures, which build the bridge between them. (1) The similarity of their geometries. For both of them, each region contacts with its adjacent regions closely. (2) The effective mass of electron changes spatially in both systems. (3) The parabolic-band effective-mass approximation can be applied in both systems. Thus, we can employ the transfer matrix method to analyse the electron transport in MoS_2/MoO_x heterostructures.

We are going to study the electron transport in MoS_2/MoO_x heterostructures under the condition of finite electric field and zero electric field, and compare the results with those for a $GaAs/Ga_{1-x}Al_xAs$ superlattice. By discussing the results, we not only give insights to help understand the negative differential resistance (NDR) discovered in 2D materials,[137, 138, 139] but also shed light on the possible design of nanoscale electronics devices.

After the described chemical treatment, a conduction band offest will form in the system. It is known that the electron affinity of MoS_2 is 4.3 eV.[4, 140] The band structures of MoO_2 and MoO_3 have also been studied theoretically and experimently. The electron affinities of MoO_2 and MoO_3 are 9 eV and 6.7 eV, respectively.[141, 142, 143, 144, 145, 146, 147] As shown in Fig. 8.1 (b), the depths of quantum wells are 4.7 eV in MoO_2 and 2.4 eV in MoO_3. l_1 and l_2 correspond to the widths of MoO_2 well and MoO_3 well. d is the width of MoS_2 in the middle. In the following calculation, we set $l_1 = 40\ nm$, $l_2 = 40\ nm$ and $d = 40\ nm$, which are the feasible parameters in EBL.[148, 149]

For one electron, one-band, parabolic-band effective-mass approximation, the Schrödinger equation in the presence of electric field is given by

$$[\frac{1}{2m^*(z)}\hat{p}_{xy}^2 + \hat{p}_z\frac{1}{2m^*(z)}\hat{p}_z + \hat{U}(z) - e\boldsymbol{F}\cdot\boldsymbol{z}]\Psi_\alpha(x,y,z) = E\Psi_\alpha(x,y,z) \quad (8.1)$$

Here, the z axis points to the direction of tunnelling, m_z^* is the space dependent effective mass, and $U(z)$ is the potential-energy function. $\hat{p}_{xy}^2$ and $\hat{p}_z^2$ stand for the momentum operators perpendicular and parallel to the z axis. $\boldsymbol{F}$ is the electric field strength. α denotes the index of the well.

Since the effective mass of an electron changes spatially in the heterostructure, the conservation of the momentum along a certain direction causes the breakdown of the kinetic-energy conservation along that direction. Thus, the coupling between transverse momentum and longitudinal momentum needs to be considered. In order to study how the coupling affects the tunneling process, the wave function of an electron should be separated with respect to its transverse and longitudinal momentum, to give

$$\Psi(x,y,z) = e^{ik_{xy}\rho}\psi(z) \quad (8.2)$$

where k_{xy} is the transverse momentum and ρ is the transverse-plane coordinate. At the same time, the Schrödinger equation can be written as,

$$[-\frac{\hbar^2}{2m^*(z)}\frac{d^2}{dz^2}+\hat{U}_\alpha(z)-eF_zz]\psi_\alpha(z)=E_z\psi_\alpha(z) \tag{8.3}$$

where E_z is the longitudinal component of total kinetic energy, and the subscript α denotes the region (MoS_2, MoO_3 or MoO_2 region) shown in Fig. 8.1. To study the influence of coupling between transverse and longitudinal momenta, an effective barrier height $U(k_{xy})$ needs to be introduced,[134] specifically

$$\hat{U}_\alpha(k_{xy})=\hat{U}_\alpha(z)-(1-\gamma_\alpha)(\hbar^2k_{xy}^2/2m_\alpha^*) \tag{8.4}$$

where $\gamma_\alpha=m_{MoS_2}^*/m_\alpha^*$. Thus, the wave functions without the presence of electric field in different regions can be written as

$$-\frac{\hbar^2}{2m_{MoS_2}^*}\frac{d^2}{dz^2}\psi(z)=E_z\psi(z) \tag{8.5}$$

$$-\frac{\hbar^2}{2m_\alpha^*}\frac{d^2}{dz^2}\psi_\alpha(z)+U(k_{xy})\psi_\alpha(z)=E_z\psi_\alpha(z) \tag{8.6}$$

Here, $E_z=E-E_{xy}$ is the longitudinal energy of the incident electron, and $E_{xy}=\hbar^2k_{xy}^2/2m_{MoS_2}^*$ is the transverse kinetic energy of the incident electron. The detailed derivation from Eqs. 8.3 to 8.5 can be found in [134].

In the presence of an electric field, the Schrödinger equation in the well becomes,

$$\frac{d^2}{dZ^2}\psi(Z)-Z\psi(Z)=0 \tag{8.7}$$

where Z is the dimensionless coordinate which is a common method to deal with Schrödinger equations in the presence of an electric field,[150] and

$$Z_\alpha=-[2m_\alpha^*/(e\hbar F_z)^2]^{1/3}(E_z-U_\alpha(k_{xy})+eF_zz) \tag{8.8}$$

The solutions to this equation are

$$\psi(Z)=aAi(Z)+bBi(Z) \tag{8.9}$$

where $Ai(Z)$ and $Bi(Z)$ are the Airy functions.[131, 135]

In GaAs, the effective mass of electron is $m_e^*=0.067m_e$ ($m_e=9.109\times10^{-31}kg$ is the mass of free electron). In the monolayer MoS_2, the effective mass of electron is $0.37m_e$.[151] For MoO_3 and MoO_2, the effective masses are $0.31m_e$.[146] and $0.85m_e$[141] respectively. It is obvious that effective mass of the electron in a MoS_2/MoO_x heterostructure is at least five times heavier than that in a $GaAs/Ga_{1-x}Al_xAs$ superlattice.

In order to calculate the transmission amplitude, the continuity condition is needed. Without electric field, the continuity condition is,

$$\psi_\alpha(z_\alpha) = \psi_\beta(z_\alpha) \tag{8.10}$$

$$\frac{1}{m_\alpha^*} \cdot \frac{d}{dx}\psi_\alpha(z_\alpha) = \frac{1}{m_\beta^*} \cdot \frac{d}{dx}\psi_\beta(z_\alpha) \tag{8.11}$$

In the presence of external electric field, the continuity condition is,

$$\begin{aligned} &\begin{pmatrix} Ai(Z_\alpha^+) & Bi(Z_\alpha^+) \\ m_\alpha^{*-2/3}Ai'(Z_\alpha^+) & m_\alpha^{*-2/3}Bi'(Z_\alpha^+) \end{pmatrix} \begin{pmatrix} a_\alpha \\ b_\alpha \end{pmatrix} \\ = &\begin{pmatrix} Ai(Z_\beta^-) & Bi(Z_\beta^-) \\ m_\beta^{*-2/3}Ai'(Z_\beta^-) & m_\beta^{*-2/3}Bi'(Z_\beta^-) \end{pmatrix} \begin{pmatrix} a_\beta \\ b_\beta \end{pmatrix} \end{aligned} \tag{8.12}$$

Here, Z_α^+ and Z_β^- represent the coordinates Z in the αth and βth region.

By using continuity condition, the transmission coefficient can be obtained. The expression for a global transfer matrix is[45]

$$M_g = \begin{pmatrix} (t')^{*-1} & rt^{-1} \\ -t^{-1}r' & t^{-1} \end{pmatrix} \tag{8.13}$$

where t and r are the transmission and reflection coefficient. $t'$and r' are the time inversed transmission and reflection coefficients. When the scattering process is symmetric with respect to time reversal, we have $t = t'$ and $r = r'$. In this work, the global transfer matrix consists of three parts for the case of a double-well structure (well MoO_2 with width l_1, well MoO_3 with width l_2 and the MoS_2 in the middle with width d) and two parts for the situation of a step-well structure (well MoO_2 with width l_1 and well MoO_3 with width l_2). Then, the global transfer matrix can be expressed as the cascading of the wells,

$$M_g = M_3 \begin{pmatrix} e^{ik_0d} & 0 \\ 0 & e^{-ik_0d} \end{pmatrix} M_1 \tag{8.14}$$

Where M_3 and M_1 refer to the transfer matrices of the MoO_3 single well and MoO_2 single well (see Fig. 8.1). The transmission amplitude T is

$$T = \frac{1}{|M_{g22}|^2} = \frac{1}{1 + |M_{g12}|^2} \tag{8.15}$$

8.2 Step- and double-well structures

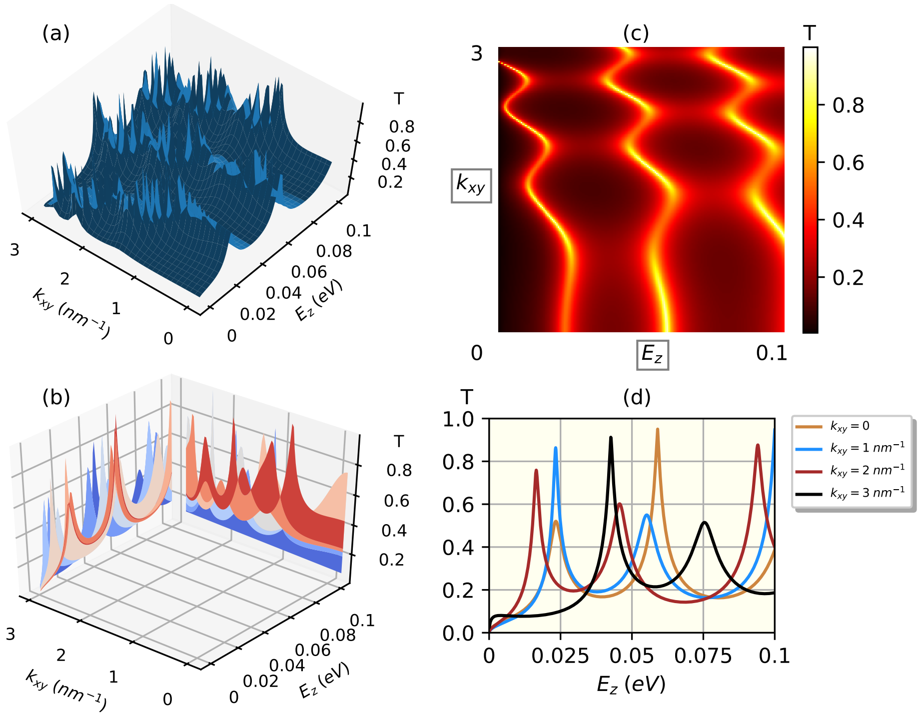

Figure 8.2: Transmission amplitudes for the step-well structure. (a) 3D plot of transmission T for the step-well structure. (b) Projections of T on E_z and k_{xy} planes based on (a). (c) Z-axis projection of T, the brighter the color is, the larger the T value (color bar). (d) 2D plot of T *vs* E_z with four different transverse momentums.

As can be seen in Fig. 8.2 (a), the step-well structure shows resonant peaks with E_z locating at 0.025, 0.05 and 0.08 eV. From (b) and (c), for the above three E_z regions, all the peaks shift towards the low energy region globally when k_{xy} increases, which is similar to what was found in previous research on the $GaAs/Ga_{1-x}Al_xAs$ double barrier.[134] In Fig. 8.2 (d), for each k_{xy}, high peaks have magnitude $0.8 \sim 0.9$ rather than 1, resulting in imperfect resonant tunnelling effect. However, small peaks show rather low T values, which should not appear in a tunnelling diode. Thus, the step-well structure needs an external electric field to optimize the resonant tunnelling condition.

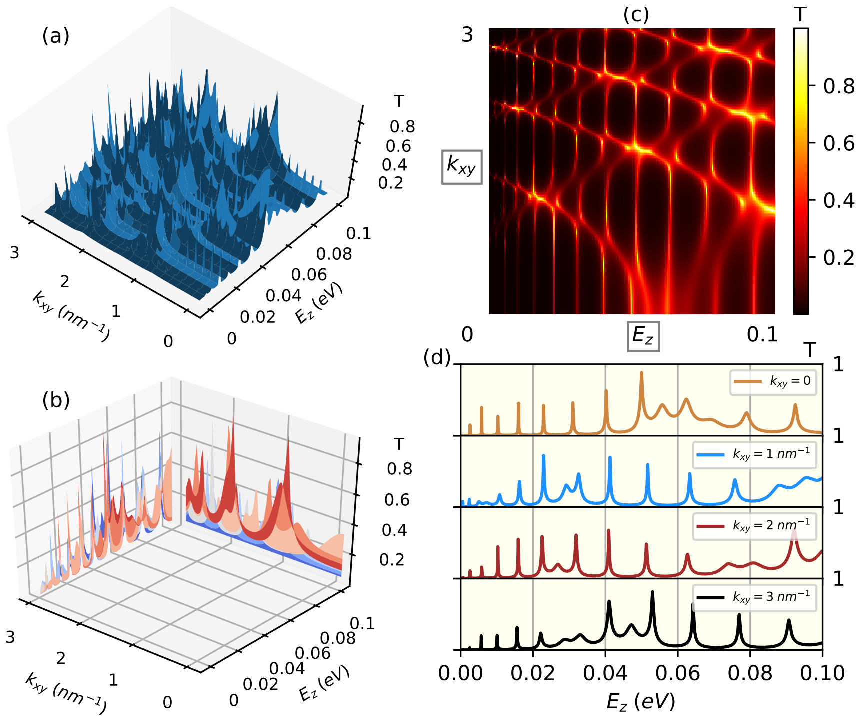

Figure 8.3: Transmission amplitudes for the asymmetric double-well structure. (a) 3D plot of transmission T. (b) Projections of T on E_z and k_{xy} planes based on (a). (c) Z-axis projection of T. (d) 2D plot of T *vs* E_z with four different transverse momentums.

Figure 8.3 describes transmission curves in an asymmetric double-well structure. In Fig. 8.3 (a), we can see more peaks with comparison to Fig. 8.2. However, from Fig. 8.3 (b) and (c), the distribution of peaks becomes much less concentrated compared with the case in the step-well structure. This is due to the distance between two wells, which alters the phase of electrons, attenuating the resonant tunnelling effect. When the distance shrinks to zero, the double-well structure will transforms into a step-well structure and show a better resonant tunnelling performance. In Fig. 8.3 (d), for each k_{xy}, many small peaks can be seen. Moreover, with k_{xy} increasing, the peak distribution doesn't show a regular transition. Concerning both the peak distribution and peak height, the double-well structure shows poor resonant tunnelling performance.

Based on the previous discussion, an external electric field is needed to optimize the resonant tunnelling condition. In the following discussion, we show the transmissions for both two structures in the presence of an external electric field along the longitudinal direction. Since a tunnelling diode is a two-terminal device, the longitudinal electric filed can be realized by applying a voltage bias between the two terminals.

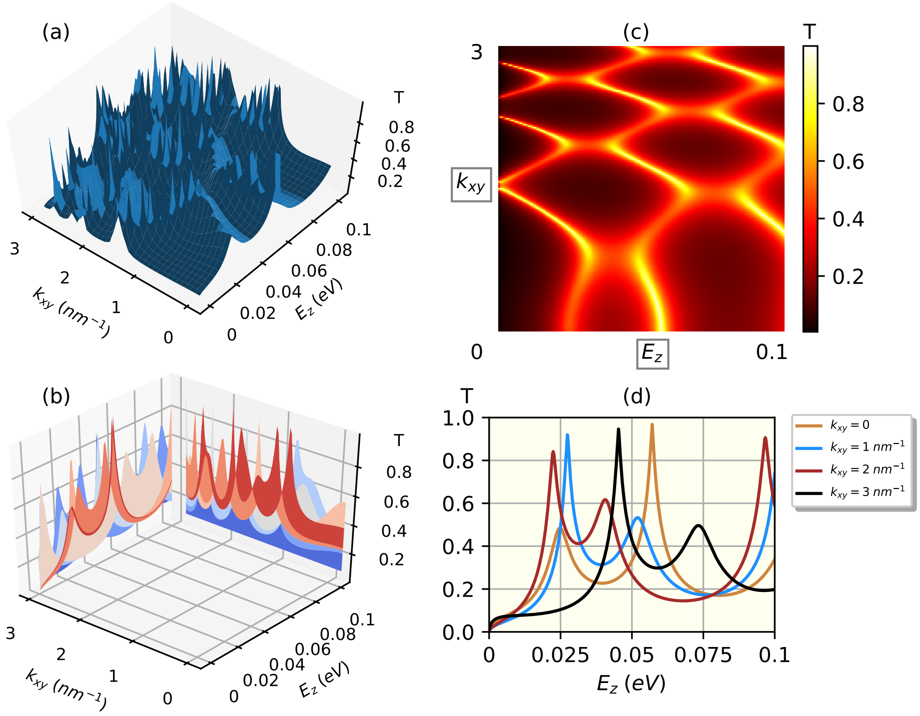

Figure 8.4: In the presence of external electric field ($V_b = 0.3\ V$), T *vs.* E_z and k_{xy} of the step-well structure. (a) 3D plot of T. (b) Projections of T on E_z and k_{xy} planes based on (a). (c) Z-axis projection of T. (d) 2D plot of T *vs* E_z.

In both Figs. 8.4 and 8.5, the applied voltage bias is 0.3 V. Compared with Fig. 8.2 (a) and (b), it is hard to tell the evolution of T in Fig. 8.4 (a) and (b). However, Fig. 8.4 (c) shows a slight enhancement of the magnitude of peaks under a weak electric field because it has a more bright area than Fig. 8.2 (c). More peaks appear within the energy region of $0.3 \sim 0.5\ eV$ and $0.5 \sim 0.8\ eV$, where as nearly no peaks appear in the case of Fig. 8.2

(c). Since more peaks emerge, we can conclude electric field can optimize the tunnelling condition to a certain extent. However, in Fig. 8.4 (d), small peaks still exist and high peaks don't reach one to become resonant peaks, indicating the external electric field still needs to be optimized.

In the case of the double-well structure, the electric field plays the same role as in the step-well case, enhancing the magnitude of peaks and introducing more peaks from Fig. 8.5 (c). However, in Fig. 8.5 (d), the evolution of T with respect to k_{xy} is still not regular, resulting from the distance between the two wells.

Generally speaking, an external electric field plays two roles in the $\mathrm{MoS_2/MoO}_x$ heterostructures. Firstly, it enhances the magnitude of existing peaks. Secondly, it intensifies the coupling between longitudinal and transverse momentums. Figure. 8.4 (c) shows that peaks only appear in the three isolated energy regions ($0 \sim 0.3\ eV$, $0.5 \sim 0.6\ eV$ and $0.8 \sim 1.0\ eV$), but more peaks are generated in the connecting area of the three energy regions ($0.5 \sim 0.6\ eV$ and $0.6 \sim 0.8\ eV$).

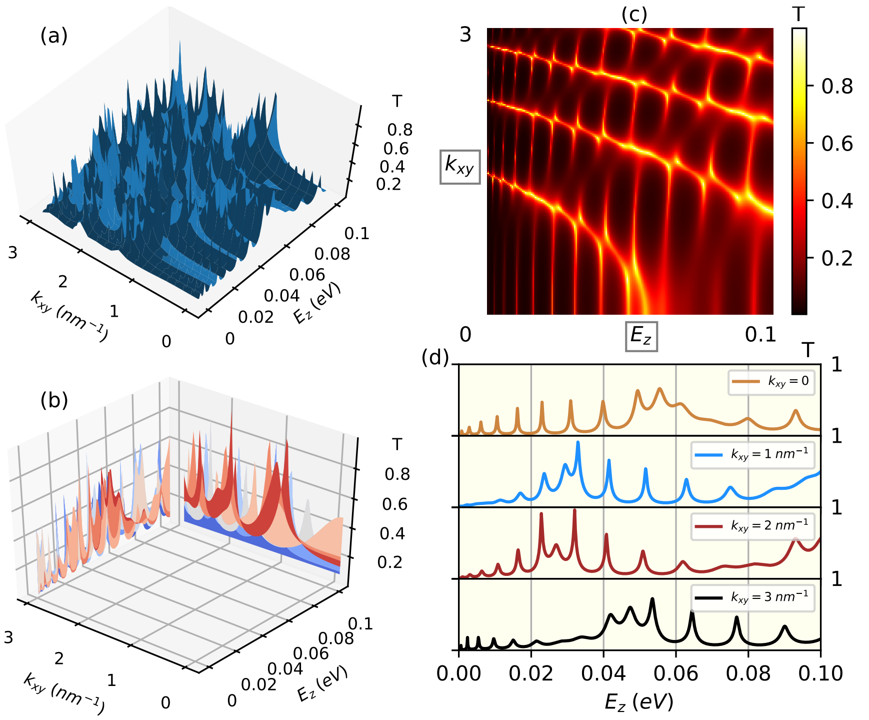

Figure 8.5: In the presence of an external electric field ($V_b = 0.3\ V$), $T\ vs.\ E_z$ and k_{xy} of the double-well structure. (a) 3D plot of T. (b) Projections of T on E_z and k_{xy} planes based on (a). (c) Z-axis projection of T. (d) 2D plot of $T\ vs\ E_z$.

To fully study the how low electric filed affects the transmission, Fig. 8.6 is presented. Fig. 8.6 illustrates the evolution of T under different positive and negative biases. In (a), for each bias, it shows a large peak within the energy range of $0 \sim 0.1\ eV$. Under $-0.15\ V$, the large peaks appears at $0.02\ eV$. Under 0, 0.15 and 0.3 V, peaks show up at $E_z = 0.06\ eV$. However, no peak shows up for a $-0.3\ V$ bias. In (b), resonant peaks don't emerge and many small peaks show up over the whole energy range. With bias increasing, the peak distribution doesn't show any regular evolution. From Fig. 8.6, we can conclude that higher bias conditions are needed due to the heavier electron effective mass in MoS_2/MoO_x heterostructures. Thus, we increase the bias value up to 1, 2 and 4 V.

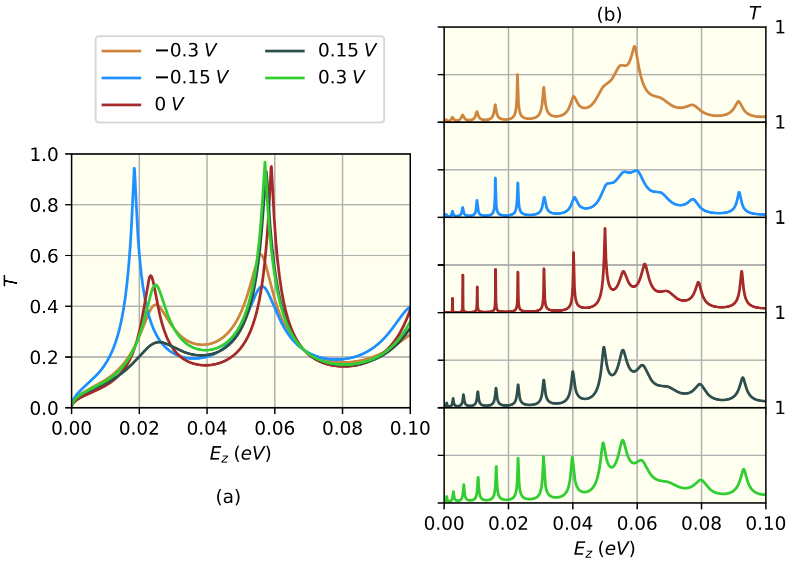

Figure 8.6: Transmission under low electric field, k_{xy} is set at zero, for (a) a step-well structure, and (b) a double-well structure.

8.3 Optimization of resonant tunnelling

Figure 8.7 shows the transmissions under $V_b = 1$, 2 and 4 V, that is ten-times larger than in Fig. 8.4, 8.5 and 8.6. For each structure, within the whole energy range, only one peak emerges with an energy value of $E_z = 0.055\ V$. In Fig. 8.7 (a), 2 V bias shows a perfect resonant peak, 1 V and 4 V show a slightly lower magnitude of peak value. However, this doesn't influence the resonant tunnelling performance since the peak distribution is quite uniform over the whole energy range. Compared with (a), Fig. 8.7 (b) demonstrates a worse resonant tunnelling performance. Although the resonant peak is quite sharp for a 2 V bias, undesirable oscillation happens in both the 1 V and 4 V cases. This phenomenon is due to the presence of separation between the two wells. After optimizing the bias condition, resonant tunnelling performance has been improved significantly, because a sharp resonant peak has been generated, indicating the negative differential resistance effect can be observed in the MoS_2/MoO_x heterostructures.

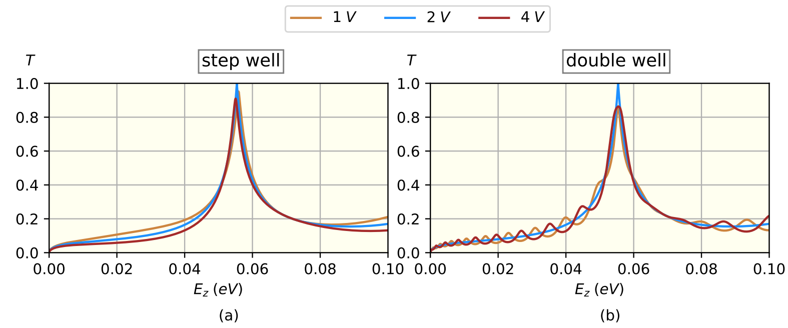

Figure 8.7: Transmission under higher bias condition with $V_b = 1$, 2 and 4 V. (a) Step-well structure. (b) Double-well structure.

In conclusion, we have shown the fabrication method used to obtain the MoS_2/MoO_x heterostructure nano device. We have also analysed the tunneling process in doule-well and step-well structures under the condition of finite electric field and zero electric field. Our analysis shows that the increasing of transverse momentum will result in the red shift of resonant peaks. We also show that low electric field ($\pm 0.3\ V$) can enhance the magnitude of peaks and intensify the coupling between longitudinal and transverse momentums. However, it can't optimize the resonant tunnelling condition due to the heavier electron effective mass of MoS_2/MoO_x heterostructures than that of traditional semiconductor superlattices. Thus, a higher bias is applied and ideal resonant tunnelling peaks are obtained, indicating that a negative differential resistance effect can be observed. Moreover, the step-well structure shows a better performance regarding resonant tunnelling than double-well structure, due to the absence of well separation which can alter the phase of electrons and affect the resonant tunnelling condition. This section gives insight on the physics of the resonant tunnelling effect and NDR in 2D-materials nano devices, also sheds light on the design of quantum electronic devices.

Chapter 9

Conclusion

In Chapter 6, we utilize radio-frequency oxygen plasma to treat 2D MoS_2 FET to enhance the performance of the device. We study the surface morphology of the same device before and after two-second rapid plasma treatment. We find that the surface thickness doubled after treatment by using AFM. We find that both the Raman E and A peaks are attenuated, and that the A exciton peak is quenched and broadened in PL spectroscopy. We further conduct electric measurements to evaluate the device performance. We find that photoresponsivity and mobility are enhanced after 2s of plasma exposure, and that the threshold voltage of the device shifts to a more negative value, indicating that the FET becomes more easily switched on. Moreover, we also utilize the polymer encapsulation technique to modify the device. We find that polymer protection can improve the device mobility and significantly enhance the device stability. The polymer protection technique can further be utilized to realize site-specific modification on MoS_2. This Chapter gives insights into surface modification and mobility engineering of 2D MoS_2 nano devices.

In Chapter 7, based on the experimental observation in Chapter 6, we apply DFT to study the electronic and magnetic properties of oxygen-plasma-treated monolayer MoS_2. We consider three types of unit cells, which are proposed based on our experimental observation in the Chapter 6. We firstly optimize the lattice parameters of the studied unit cells. We further combine the three types of unit cell to make various 2×2 super cells. By calculating their band structures, we find that sulphur vacancy can cause significant quenching of the band gap and that oxygen adatoms can make the direct band gap of pristine MoS_2 indirect band gap. Moreover, from the spin-dependent DOS, we also find that neither sulphur vacancy nor oxygen adatom can introduce a ferromagnetic phase in ML MoS_2, which is consistent with others' work. Regarding spin-orbit coupling, our calculated SOC strength in pristine MoS_2 is consistent with others' work. An oxygen adatom can change the location of band splitting changed, which is attributed to the modification of band structure by oxygen adatoms. This Chapter gives insight into band-structure engineering and the potential for valley electronics of 2D materials.

In Chapter 8, we firstly show how to fabricate MoS_2/MoO_x heterostructures using plasmas. Then we study the electron transport in them by TMM. We analyse the tunneling process in double-well structures and step-well structures under the condition of finite electric field and zero electric field. We show that the increasing of transverse momentum will result in the red shift of resonant peak. We also show that a low electric field ($\pm 0.3\ V$) can enhance the magnitude of peaks and intensify the coupling between longitudinal and transverse momentums. However, it can't optimize the resonant tunnelling condition due to the heavier electron effective mass of MoS_2/MoO_x heterostructures than that in traditional semiconductor superlattices. Thus, a higher bias is applied and ideal resonant tunnelling peaks are obtained, indicating that negative differential resistance (NDR) effect can be observed. Moreover, step-well structure shows a better performance in terms of resonant tunnelling than double-well structure, due to the absence of well separation which can alter the phase of electrons and affect resonant tunnelling condition. This Chapter gives insights into the physics of the resonant tunnelling effect and NDR in 2D-materials nano devices, also sheds light on the design of quantum electronic devices.

In conclusion, we have studied the oxygen-plasma-treated 2D MoS_2 experimentally and theoretically. This project gives insights into the physics of 2D materials including various topics such as 2D field-effect transistors, nano-device modification by plasma engineering, band-structure engineering, materials simulation, electron transport and negative differential resistance effect.

In the next Chapter, we are going to introduce the Outlook based on the results that we obtained in previous Chapters.

Chapter 10

Outlook

10.1 Mobility engineering of 2D FETs

(This section is based on Chapter 6.)

In Chapter 6, we have already discussed the merits of polymer encapsulation (protection). It can improve the device mobility and stability by protecting the device from impurity scattering coming from the environment, suggesting it can be utilized in the mobility engineering for 2D FETs. Polymer protection is one angle to study the mobility engineering of 2D FETs.

Actually, mobility engineering is a big topic in the field of 2D materials. The beginning of the story traces back to *Moore's law.* However, *Moore's law* is confronted with a fundamental barrier. Because the gate length of the most advanced Si MOSFET is 20 *nm* beyond that at which the quantum tunnelling effect will play an important role, namely, conventional electron transport model (like small-signal equivalent FET circuit in Fig. 6.15) will fail when the gate length becomes shorter and shorter. Thus, the framework of *More Than Moore* is conceived.[1] *More than Moore* is not primarily targeted on increasing circuit complexity but rather on enhancing functionalities of individual devices. The emergence of graphene and other two-dimensional (2D) materials which exhibit abundant new properties enabling novel types of nano devices.[3, 4] Extensive research effort has been concentrated on 2D field-effect transistors (2D FETs) whose channel materials are 2D materials. These novel devices reveal great potential to meet the requirements of *More Than Moore.*

Graphene FETs used to be the first candidate for post-silicon electronics due to its incredible mobility.[5] However, the lack of a bandgap and poor power gain make graphene FETs impractical to logic applications because the device cannot be properly turned off.[6, 7] The emergence of thin-film MoS_2 brought new vitality to the study of 2D FETs. Monolayer MoS_2, with a direct bandgap 1.9 eV and electron effective mass 0.39 m_e, not only meets the requirement of an effective off state but also overcomes the difficulty of the short-channel effect, a major challenge in the FET miniaturization.[2, 4] Moreover, monolayer MoS_2 also has great photoresponsivity to a broad range of waves, which makes them a good candidate for nanoscale photoelectronics.[8, 9]

The most important issue of 2D MoS_2 FETs is a relatively low mobility. For pristine MoS_2, the theoretical mobility value is about 410 $cm^2\ V^{-1}\ s^{-1}$ at room temperature.[10] However, the experimental-extracted mobilities from MoS_2 MOSFET structures are between $1 \sim 300$ $cm^2\ V^{-1}\ s^{-1}$.[11, 12, 13, 14] It is crucial to understand the effects of mobility degradation and to seek a practical approach to enhance it.

Approach Mobility engineering aims at enhancing the mobility of 2D MoS_2 FETs. The first problem that needs to be solved is contact resistance. Currently, the most common used method is thermal annealing. The most used contact materials are Au and Ti, whose work function matches the MoS_2 electron affinity. Recently, graphene was utilized to optimize contact resistance due to its work function tunable by back gating.[152, 153]

The most significant problem that needs to be solved is charge scattering. Generally, there are two main types scattering mechanisms. They are impurity scattering introduced by dirty surfaces and gaseous molecules in the environment, and phonon scattering which is governed by temperature since the number of phonons obeys the Bose-Einstein distribution.[81]

Hence, it is quite clear that figuring out the underlying physics of impurity scattering and phonon scattering is one of the main purposes of mobility engineering. However, phonon scattering cannot be eliminated since it always exists if the temperature is not zero. The mechanism of phonon scattering and relevant effects (such as deformation potential, Frohlich and piezoelectric interactions) are not totally understood and are still being studied.[32, 58, 85, 154]

Thus, reducing the impurity Coulomb scattering becomes the most important topic. D. Jena claims that coating nanostructures with high-κ dielectric can screen Coulomb impurities.[155] Some papers reported that dielectric coating can enhance mobility,[12, 156, 157] but other papers showed that dielectric coating will cause remote interface phonon (RIP) effect leading to mobility degradation.[158, 159] Th contradiction between dielectric screening and RIP needs to be solved. We also find that polymer protection can enhance the device mobility in Chapter 6. However, its drawbacks and how we can optimize the polymer encapsulation technique to further improve the device performance still needs to be studied.

10.2 Memristors and neuromorphic electronics

(This section is based on Chapter 6 and 8.)

Artificial neural networks have been an important research topic due to its wide range of applications, such as pattern recognition,[160] control system,[161] and deep learning like AlphaGo.[162] However, the computation process of AlphaGo is based on conventional computational structure also called the Von Neumann architecture, resulting in a highly complex system with 1202 CPUs and 176 GPUs, and high-power consumption.[162] To overcome the complexity and high-power consumption of Von-Neumann based neural networks, three types of hardware towards neuromorphic systems are being studied. They are very large scale integration (VLSI),[163, 164] optical neural networks,[163, 165] and electronic neuron networks.[163] In terms of electronic neuron networks, two main types of architectures are being studied, including the crossbar array,[166, 167, 168, 169, 170] and multiple-channel planar nanodevices.[171, 172, 173, 174]

In the case of the crossbar array, only two terminals can be fabricated corresponding to the top crossbar and the bottom crossbar. However, in a biological synapse, multiple input terminals are required. Thus, in terms of inputting multiple signals simultaneously to emulate a biological synapse, crossbar architecture is no longer effective. The emergence of multiple-terminal planar devices in recent years can effectively solve this problem.[171, 172, 173, 174]

In recent studies, a high switching ratio up to 200 has been achieved in multiple-channel planar devices.[173] Moreover, the retention characteristics of the high resistance state (HRS) or low resistance state (LRS) is over 24 hours, indicating a non-volatile state of memory. The success in retention characteristics suggests that long-term potentiation (depression) that is regarded as one main effect in the mechanism of human learning and memory can be emulated in electronics devices.[175, 176] Another important feature of a biological synapse is synaptic plasticity. In a planar device, synaptic plasticity can be achieved by either gating or external planar electrode.[173, 174] Moreover, gating can also enhance the switching ratio up to ten times.[173] So far, both long-term potentiation and synaptic plasticity can be achieved in a planar resistive switching memristor (PRSM), indicating that PRSMs have already become the candidate for neuromorphic electronics.

Sangwan *et al* has successfully realized heterosynaptic plasticity in polycrystalline monolayer MoS_2.[173] Their PRSM geometry is a typical FET with 6 terminals (electrodes). The terminology ‘polycrystalline’ in their case specifically refers to the grain boundary. Generally speaking, a grain boundary is one type of heterostructure, because it reflects the nonuniform spatial distribution of materials in the system. As mentioned in Chapter 6 and 8, our oxygen-plasma treatment can also introduce heterostructures into MoS_2, suggesting that plasma treatment can introduce memristive behaviour into MoS_2.

In Chapter 8, we already prove that MoS_2/MoO_x heterostructures can introduce negative differential resistance (NDR). In both Strukov and Kvatinsky’s work,[177, 178] they indicate that any nonlinear $I-V$ characteristics can be regarded as a general memristive behaviour, such as Josephson junctions and neon bulbs. Thus, in a ML MoS_2 FET, the NDR introduced by plasma can be regarded as a general memristor. Thus, ML MoS_2 is a promising candidate for memristive systems from the point of view of both PRSMs and general memristors.

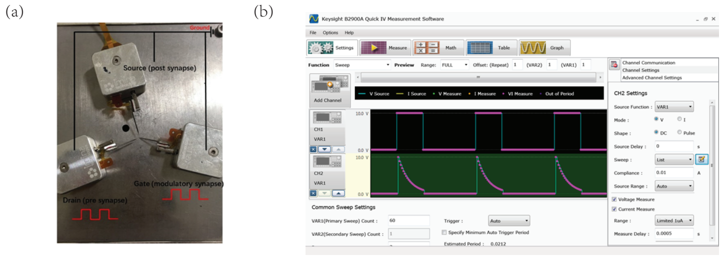

Function: Sweep
Preview Range: FULL
Offset: (Repeat) 1 (VAR2) 1 (VAR1) 1

CH2 Settings
Source Function : VAR1
Mode : ● V ○ I
Shape : ● DC ○ Pulse
Source Delay : 0 s
Sweep : List
Compliance : 0.01 A
Source Range : Auto
☑ Voltage Measure
☑ Current Measure
Range : Limited 1uA
Measure Delay : 0.0005 s

Common Sweep Settings
VAR1(Primary Sweep) Count : 60
VAR2(Secondary Sweep) Count : 1
Trigger : Auto
☐ Specify Minimum Auto Trigger Period
Estimated Period : 0.0212

Figure 10.1: (a) Different pulse modes in our system to realize synaptic plasticity. (b) Illustration of the electrical system with three terminals. This electric system is the same system as shown in Fig. 5.7.

Figure 10.1 (a) shows how we achieve synaptic plasticity in our system. This system has a similar setup as that of Sangwan *et al.*[173] Two terminals can be thought of as pre and post synapse, and the third terminal stands for the modulatory synapse. Various pulse modes are shown in (b).

10.3 Valley electronics and spin filters based on 2D TMDs

(This section is based on Chapter 7 and 8.)

Based on our calculation in Chapter 7 and others' work,[17, 21, 22] it is clear that the band gap appears at the K valley in ML MoS$_2$. Due to the time-reversal symmetry, another band gap should be at the $-K$ valley. It is known that in graphene electrons at $\pm K$ valleys are massless Dirac Fermions due to the linear dispersion relation. The similar situation also happens in ML MoS$_2$ where electrons are described by massive Dirac Fermions to the first order,[18]

$$\hat{H} = at(\tau k_x \hat{\sigma_x} + k_y \hat{\sigma_y}) + \frac{\Delta}{2}\hat{\sigma_z} \tag{10.1}$$

where $\tau = \pm 1$ is the valley index. a is the lattice parameter which can be obtained either by first principles calculation or experimental characterization. t is the hopping parameter, which is described by the Slater-Koster coefficients which we have introduced in Chapter 4. σ_x and σ_y are Pauli matrices. Thus, we summarize the coupled spin and valley in Table. 10.1.

Table 10.1: Coupled spin and valley indices for an electron in ML MoS$_2$. The valley indices of K and K are +1 and -1.

	K	-K
$\mid\uparrow>$	(1, 1)	(1, -1)
$\mid\downarrow>$	(-1, 1)	(-1, -1)

The modified Dirac Hamiltonian has the form [179, 180]

$$\hat{H} = v_F(\hat{\sigma_\tau} \cdot \hat{p}) + \frac{\Delta}{2}\sigma_z + \lambda s\tau(\frac{1-\sigma_z}{2}) + \frac{\hat{p}^2}{4m_0}(\alpha + \beta\sigma_z) \tag{10.2}$$

λ is spin-orbit coupling strength whose value is about 70 meV as calculated in Chapter 7. v_F is the Fermi velocity for ML MoS_2 with a value of 0.53×10^6 m/s. The v_F of ML MoS_2 is half of the v_F of graphene. $s = \pm 1$ and $\tau = \pm 1$ are spin and valley indices, respectively. Δ is band gap value. $\alpha = 0.43$ and $\beta = 2.21$ can be regarded as correction terms.[24, 151, 179]

In Chapter 8, we have shown that the TMM is a powerful tool to study electron transport in 2D systems. The TMM method can also be applied to analyse electron transport with the Hamiltonian shown in Eq 10.2. Majidi *et al* apply the TMM to study the spin- and valley- dependent electron transmission in a normal/ferromagnetic/normal MoS_2 heterostructure.[24] In their case, due to the exchange bias generated at the interface between a ferromagnetic phase (such as high κ dielectric EuO) and nonmagnetic phase (MoS_2),[181, 182] the Hamiltonian in Eq 10.2 changes to $\hat{\tilde{H}} = \hat{H} - hs$, where h is the exchange-field strength. They find the electron transmission highly depends on the coupled spin and valley indices.[24]

Majidi's work gives good insight into the spintronics and 2D spin filters.[24] Now, we would like to compare our structure shown in Chapter 8 with theirs. In our case, we don't have the ferromagnetic phase over the ML MoS_2. It is known that the fabrication of overlayer ferromagnetic phase is based on atomic layer deposition (ALD). Thus, our rapid plasma treatment is a more convenient technique in terms of device fabrication. Then, regarding transmission T, Majidi *et al* tune T by introducing an exchange bias, which later appears in the Hamiltonian with the form hs. In their case, the band gap Δ is a constant in the whole transport process. However, in our case, we don't have the exchange-field introduced term in the Hamiltonian. What we have is the conduction-band offset in the MoS_2/MoO_x heterostructure as shown in Fig. 8.1. Thus, what we can tune is the Δ in Eq 10.2. In Chapter 8, we have already shown that the quantum well generated by the conduction band offset can realize resonant tunneling effect and NDR. Thus, the next step would be studying the spin-dependent transmission with the $\pm K$-valley Hamiltonian shown in Eq 10.2.

Moreover, the device conductance G (observable) can also be modified. G is defined as,[24, 133]

$$G = G_0 \int_{-pi/2}^{\pi/2} T(E_F, s, \tau) cos\theta d\theta \tag{10.3}$$

Here, θ is the angle between incident electrons and quantum wells/barriers. Majidi *et al* study the chemical-potential dependent conductance. In our case the chemical potential of the materials can be easily tuned by back gating.

10.4 Relativistic band structure for 2D TMDs

(This section is based on Chapter 7.)

(The main reference of this section is Ref [183].)

In Chapter 7, we have studied the spin-orbit coupling (SOC) effect in pristine and oxygen-plasma-treated ML MoS$_2$. It is known that the SOC is a relativistic correction, because SOC is caused by the interaction between electron spin and electron magnetic moment. The interaction is described by Thomas precession. The SOC Hamiltonian has the form $\hat{H}_{SOC} = \frac{1}{2\mu^2 c^2 r}\frac{dV}{dr}\hat{L}\cdot\hat{s}$. It is proportional to $(\frac{v}{c})^2$, indicating that it is a relativistic correction. Moreover, a more strightforward way to show it is to solve the Dirac equation for a hydrogen atom. The solved eigenvalues will directly show the energy splitting caused by SOC.

However, except for the SOC, there are other three types of relativistic correction to the electrons moving around a nuclei. They are Lamb shift, relativistic mass correction, and Darwin term.

W. E. Lamb and J. C. Retherford applied a microwave-based method to prove the existence of an energy shift of $2S_{1/2}$ and $2P_{1/2}$ in a hydrogen atom, resulting in $2S_{1/2}$ having a higher energy than $2P_{1/2}$.[184] The Lamb shift is an important effect in nuclear physics. It mainly happens in the core energy level. The uncertainty principle in the core levels, where electrons are tightly bounded to the nuclei, causes a large uncertainty of momentum. Thus, electrons at d or f orbitals don't show an observable Lamb shift. Regarding band structure calculations, we can neglect the energy contribution from the Lamb shift.

The relativistic mass correction and Darwin term can both be dealt with using perturbation theory. Let's consider the relativistic-mass correction Hamiltonian H_{rel} first. Expanding the relativistic kinetic energy to third order, we have,

$$\hat{T} = \sqrt{m^2c^4 + p^2c^2} - mc^2 = mc^2(1 + \frac{p^2}{2m^2c^2} - \frac{p^4}{8m^4c^4}) - mc^2 + \dots \quad (10.4)$$

Where m is the electron rest mass. The second term in the bracket is the traditional kinetic energy. The third term $H_{rel} = -\frac{p^4}{m^3c^2}$ is the relativistic-mass correction Hamiltonian. Thus, the new Hamiltonian is $\hat{H} = \hat{H}_0 + \hat{H}_{rel}$. To calculate the eigenvalue of $\hat{H}_{rel}$ is to calculate $< \hat{p}^4 >$. It would be much easier to solve the eigen equation of $< \hat{p}^4 >$ in atomic and dimensionless units. We directly show the calculated results,

$$< \hat{p}^4 >= -\frac{3}{n^4} + \frac{4}{n^3(l+\frac{1}{2})} \tag{10.5}$$

where n and l are the principal and angular momentum quantum number. Then, the calculated dimensionless energy would be,

$$< \hat{H}_{rel} >= (|E_0|\frac{\alpha^2}{n})(\frac{3}{4n} - \frac{1}{l+\frac{1}{2}}) \tag{10.6}$$

Here, α is fine structure constant. $E_0 = \epsilon_0/n^2$ is dimensionless ground state energy. The illustration of the relativistic-mass correction caused energy shift is shown in Fig. 10.2. In Fig. 10.2, the y axis is energy shift δE. The principal and angular momentum quantum numbers are $n = 2$ and $l = 0,\ 1$ respectively. On the right side, three dashed lines show the energy shift of each orbital.

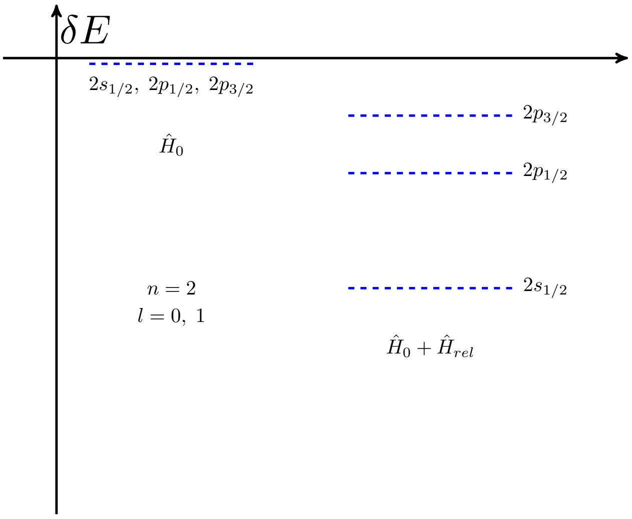

Figure 10.2: Energy shift caused by relativistic mass correction. The y axis is energy shift δE.

We further study the Darwin term, and integrate the Darwin term with $\hat{H}_{rel}$. The Darwin term was first derived by C. G. Darwin. It has the form,[185]

$$\hat{H}_D = \frac{1}{8}(\frac{\hbar^2}{mc})^2\nabla^2 V \tag{10.7}$$

where $\nabla^2 \frac{1}{r} = -4\pi\delta(x)$. The process of dealing with $\hat{H}_D$ is same as $\hat{H}_{rel}$. The calculated dimensionless eigenvalues of $\hat{H}_D$ are,

$$< \hat{H}_D >= \pi\alpha^2 < \delta(x) > \tag{10.8}$$

The $< \delta(x) >$ doesn't vanish only at $x = 0$. Only s orbital electrons with $l = 0$ have a contribution to the Darwin term. In Fig. 10.3, it can be seen how $\hat{H}_D$ the energy splitting.

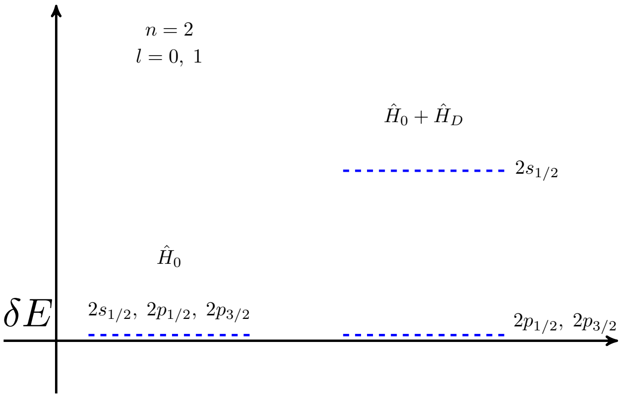

Figure 10.3: Energy shift caused by Darwin term. The y axis is energy shift δE.

Let's compare Figs. 10.2 and 10.3. It can be found that the relativistic-mass correction has a negative energy shift. The Darwin term provides a positive energy shift. Thus, the final effect of energy splitting would not be significant.

The full Hamiltonian $\hat{H} = \hat{H}_0 + \hat{H}_{SOC} + \hat{H}_{rel} + \hat{H}_D$ has a significant influence on heavy elements like tungsten (W), platinum (Pt) and plumbum (Pb).[186] Lent *et al* show that $\hat{H}_{rel}$ and $\hat{H}_D$ causes a significant band splitting around the Fermi level in PbTe.[187] Moreover, Herman *et al* apply the relativistic orthogonalized plane wave method to explain the band structure of GeTe and PbTe.[188] Christensen also apply relativistic augmented plane wave method to show the energy shift in the band structure of tungsten.[189] The relativistic correction (the relativistic mass correction or the Darwin term) is not significant in MoS_2. However, whether it is important in heavy-element TMDs like WS_2 or WSe_2 hasn't been studied. We believe that the study of the full-relativistic correction on heavy-element 2D TMDs will give us a better understanding of the physics of TMDs.

Appendix A

Quantum Espresso input files

(A template of QE input file is shown. By changing the input parameters, figures in Chapter 7 can be repeated.)

```
& CONTROL
calculation = ”scf”
restart_ mode = ”from_ scratch”
prefix=”mos2”
pseudo_ dir = ”...”
outdir=”...”
/
& SYSTEM
a=6.33800e+00
c=1.50000e+01
ecutrho=5.00000e+02
ecutwfc=1.00000e+02
ibrav= 4
lspinorb= .FALSE.
nat= 12
noncolin= .FALSE.
nosym= .FALSE.
ntyp= 3
occupations= ”fixed”
```

```
/
& ELECTRONS
conv_ thr=1.00000e-06
electron_ maxstep=200
mixing_ beta=3.00000e-01
mixing_ mode=”plain”
startingpot=”atomic”
startingwfc=”atomic+random”
/
K_ POINTS {automatic}
8 8 1 0 0 0

ATOMIC_ SPECIES
Mo 95.94000 Mo.pbe-spn-rrkjus_ psl.1.0.0.UPF
S 32.06600 S.pbe-nl-rrkjus_ psl.1.0.0.UPF
O 15.99940 O.pbe-nl-rrkjus_ psl.1.0.0.UPF

ATOMIC_ POSITIONS {angstrom}
Mo -0.000158 1.829578 3.140954
S 1.584342 0.914768 1.574874
S 1.584342 0.914764 4.674063
Mo -1.584658 4.574013 3.140954
S -0.000158 3.659203 1.574874
Mo 3.168842 1.829578 3.140954
S 4.753342 0.914768 1.574874
S 4.753342 0.914764 4.674063
Mo 1.584342 4.574013 3.140954
S 3.168842 3.659203 1.574874
S 3.168842 3.659199 4.674063
O 3.168842 3.659199 6.152884
```

Appendix B

MATLAB code for transfer matrix method

(No extra files are needed. The following code can be run directly in MATLAB.)
(Here, .∧ is power operation. ∧ can be input by ”shift + 6”.)

(The following code can reproduce Fig. 3.2.)

```
b=10; x1=0:0.001:3; x2=-2:0.001:0;
T1= 1 ./ ( 1 + 0.25 .* ( (x1.∧ 2 -x1).(-1) ).* ( sin(2*b.*(x1-1).∧(0.5)) ).∧2);
T2= 1 ./ ( 1 + 0.25 .* ( (x2.∧ 2 -x2).(-1) ).* ( sin(2*b.*(-x2+1).∧(0.5)) ).∧2);
plot(x1,T1); hold on; plot(x2,T2);
xlabel(’E/V’);ylabel(’T’);
```

(The following code can reproduce Fig. 8.2.)

```
hb=1.055*1e-34;me=9.109*1e-31;
l1=40*1e-9;d=0;l2=40*1e-9;
U1=-4.7;U2=-2.4;
m0=0.37*me;
m1=0.85*me;
m2=0.31*me;
[kxy,Ez]=meshgrid(0:3e7:3e9,0:0.001:0.1);
Ukxy1=1.6*1e-19*U1-(1-m0/m1) .* ( ((hb.*kxy).∧2) / (2*m1) );
```

```
Ukxy2=1.6*1e-19*U2-(1-m0/m2) .* ( ((hb.*kxy).∧2) / (2*m2) );
k0=((1.6*1e-19*2*m0.*(Ez)).∧0.5) / hb;
k1=((2*m1.*(1.6*1e-19.*Ez-Ukxy1)).∧0.5) / hb;
k2=((2*m2.*(1.6*1e-19.*Ez-Ukxy2)).∧0.5) / hb;
Mg12=(cos(l2.*k2) + (k0./k2+k2./k0) .* (sin(l2.*k2)*0.5*1i)) .* ((k1./k0-k0./k1)
.* (sin(l1.*k1))*0.5*1i) .* (exp(1i.*k0*d)) + ((k2./k0-k0./k2).*(sin(l2.*k2))*0.5*1i)
.* ( cos(l1.*k1)-(k0./k1+k1./k0).*(sin(l1.*k1))*0.5*1i ) .* (exp(-1i.*k0*d));
Mg22=(k2./k0-k0./k2) .* (sin(l2.*k2)*0.5*-1i) .* (k1./k0-k0./k1) .* (sin(l1.*k1)*0.5*1i)
.* (exp(1i.*k0*d)) + (cos(l1.*k1) - (k0./k1+k1./k0) .* (sin(l1.*k1)*0.5*1i)) .*
(cos(l2.*k2) - (k0./k2+k2./k0) .* (sin(l2.*k2)*0.5*1i)) .* (exp(-1i.*k0*d));
a=abs(Mg12);T=1./(1+a);

surf(kxy,Ez,T);
shading interp;set(gca, ’YDir’,’reverse’); colormap(jet);
xlabel(’kxy (nm{ ∧ {-1} })’,’FontWeight’,’bold’);
ylabel(’Ez (eV)’,’FontWeight’,’bold’);
zlabel(’Transmission’,’FontWeight’,’bold’);
set(gca,’XTickLabel’,{’0’,’0.5’,’1’,’1.5’,’2’,’2.5’,’3’});
set(gca,’FontName’,’Times New Roman’,’FontSize’,9,’FontWeight’,’bold’);
view([-1.4,0.6,1]);
```

Bibliography

[1] Wolfgang Arden, Michel Brillouët, Patrick Cogez, Mart Graef, Bert Huizing, and Reinhard Mahnkopf. More-than-Moore white paper. *Version*, 2:14, 2010.

[2] F Schwierz, J Pezoldt, and R Granzner. Two-dimensional materials and their prospects in transistor electronics. *Nanoscale*, 7(18):8261–8283, 2015.

[3] Andre K Geim and Konstantin S Novoselov. The rise of graphene. *Nature Materials*, 6(3):183–191, 2007.

[4] Kin Fai Mak, Changgu Lee, James Hone, Jie Shan, and Tony F Heinz. Atomically thin MoS_2: a new direct-gap semiconductor. *Physical Review Letters*, 105(13):136805, 2010.

[5] Frank Schwierz. Graphene transistors. *Nature Nanotechnology*, 5(7):487–496, 2010.

[6] Gui Gui, Jin Li, and Jianxin Zhong. Band structure engineering of graphene by strain: First-principles calculations. *Physical Review B*, 78(7):075435, 2008.

[7] Fengnian Xia, Damon B Farmer, Yu-ming Lin, and Phaedon Avouris. Graphene field-effect transistors with high on/off current ratio and large transport band gap at room temperature. *Nano Letters*, 10(2):715–718, 2010.

[8] Zongyou Yin, Hai Li, Hong Li, Lin Jiang, Yumeng Shi, Yinghui Sun, Gang Lu, Qing Zhang, Xiaodong Chen, and Hua Zhang. Single-layer MoS_2 phototransistors. *ACS Nano*, 6(1):74–80, 2011.

[9] Xudong Wang, Peng Wang, Jianlu Wang, Weida Hu, Xiaohao Zhou, Nan Guo, Hai Huang, Shuo Sun, Hong Shen, Tie Lin, et al. Ultrasensitive and broadband MoS_2 photodetector driven by ferroelectrics. *Advanced Materials*, 27(42):6575–6581, 2015.

[10] Kristen Kaasbjerg, Kristian S Thygesen, and Karsten W Jacobsen. Phonon-limited mobility in n-type single-layer MoS_2 from first principles. *Physical Review B*, 85(11):115317, 2012.

[11] Branimir Radisavljevic and Andras Kis. Mobility engineering and a metal–insulator transition in monolayer MoS_2. *Nature Materials*, 12(9):815–820, 2013.

[12] Branimir Radisavljevic, Aleksandra Radenovic, Jacopo Brivio, i V Giacometti, and A Kis. Single-layer MoS_2 transistors. *Nature Nanotechnology*, 6(3):147–150, 2011.

[13] Wenzhong Bao, Xinghan Cai, Dohun Kim, Karthik Sridhara, and Michael S Fuhrer. High mobility ambipolar MoS_2 field-effect transistors: Substrate and dielectric effects. *Applied Physics Letters*, 102(4):042104, 2013.

[14] Wei Liu, Jiahao Kang, Wei Cao, Deblina Sarkar, Yasin Khatami, Debdeep Jena, and Kaustav Banerjee. High-performance few-layer-MoS_2 field-effect-transistor with record low contact-resistance. In *Electron Devices Meeting (IEDM), 2013 IEEE International*, pages 19–4. IEEE, 2013.

[15] Michael A Lieberman and Alan J Lichtenberg. *Principles of plasma discharges and materials processing.* John Wiley & Sons, 2005.

[16] Xiaodong Xu, Wang Yao, Di Xiao, and Tony F Heinz. Spin and pseudospins in layered transition metal dichalcogenides. *Nature Physics*, 10(5):343, 2014.

[17] Gui-Bin Liu, Wen-Yu Shan, Yugui Yao, Wang Yao, and Di Xiao. Three-band tight-binding model for monolayers of group-VIB transition metal dichalcogenides. *Physical Review B*, 88(8):085433, 2013.

[18] Di Xiao, Gui-Bin Liu, Wanxiang Feng, Xiaodong Xu, and Wang Yao. Coupled spin and valley physics in monolayers of MoS_2 and other group-VI dichalcogenides. *Physical Review Letters*, 108(19):196802, 2012.

[19] Kin Fai Mak, Keliang He, Jie Shan, and Tony F Heinz. Control of valley polarization in monolayer MoS_2 by optical helicity. *Nature Nanotechnology*, 7(8):494, 2012.

[20] Hualing Zeng, Junfeng Dai, Wang Yao, Di Xiao, and Xiaodong Cui. Valley polarization in MoS_2 monolayers by optical pumping. *Nature Nanotechnology*, 7(8):490, 2012.

[21] Shiang Fang, Rodrick Kuate Defo, Sharmila N Shirodkar, Simon Lieu, Georgios A Tritsaris, and Efthimios Kaxiras. Ab initio tight-binding Hamiltonian for transition metal dichalcogenides. *Physical Review B*, 92(20):205108, 2015.

[22] Andor Kormányos, Guido Burkard, Martin Gmitra, Jaroslav Fabian, Viktor Zólyomi, Neil D Drummond, and Vladimir Falko. k· p theory for two-dimensional transition metal dichalcogenide semiconductors. *2D Materials*, 2(2):022001, 2015.

[23] PM Krstajić, P Vasilopoulos, and M Tahir. Spin-and valley-polarized transport through ferromagnetic and antiferromagnetic barriers on monolayer MoS2. *Physica E: Low-dimensional Systems and Nanostructures*, 75:317–321, 2016.

[24] Leyla Majidi, Moslem Zare, and Reza Asgari. Valley-and spin-filter in monolayer MoS_2. *Solid State Communications*, 199:52–55, 2014.

[25] Fernando Wypych and Robert Schöllhorn. 1T-MoS_2, a new metallic modification of molybdenum disulfide. *Journal of the Chemical Society, Chemical Communications*, (19):1386–1388, 1992.

[26] Ivan N Yakovkin. Dirac cones in graphene, interlayer interaction in layered materials, and the band gap in MoS_2. *Crystals*, 6(11):143, 2016.

[27] *Part I*, page 5256. Cambridge University Press, 2017.

[28] Andrea Splendiani, Liang Sun, Yuanbo Zhang, Tianshu Li, Jonghwan Kim, Chi-Yung Chim, Giulia Galli, and Feng Wang. Emerging photoluminescence in monolayer MoS_2. *Nano Letters*, 10(4):1271–1275, 2010.

[29] Dieter K Schroder. *Semiconductor material and device characterization.* John Wiley & Sons, 2006.

[30] Adelmo Ortiz-Conde, FJ Garcıa Sánchez, Juin J Liou, Antonio Cerdeira, Magali Estrada, and Y Yue. A review of recent MOSFET threshold voltage extraction methods. *Microelectronics Reliability*, 42(4):583–596, 2002.

[31] Gérard Ghibaudo. New method for the extraction of MOSFET parameters. *Electronics Letters*, 24(9):543–545, 1988.

[32] Song-Lin Li, Katsunori Wakabayashi, Yong Xu, Shu Nakaharai, Katsuyoshi Komatsu, Wen-Wu Li, Yen-Fu Lin, Alex Aparecido-Ferreira, and Kazuhito Tsukagoshi. Thickness-dependent interfacial coulomb scattering in atomically thin field-effect transistors. *Nano Letters*, 13(8):3546–3552, 2013.

[33] Th Von Woedtke, S Reuter, K Masur, and K-D Weltmann. Plasmas for medicine. *Physics Reports*, 530(4):291–320, 2013.

[34] Narae Kang, Hari P Paudel, Michael N Leuenberger, Laurene Tetard, and Saiful I Khondaker. Photoluminescence quenching in single-layer MoS_2 via oxygen plasma treatment. *The Journal of Physical Chemistry C*, 118(36):21258–21263, 2014.

[35] Hui Zhu, Xiaoye Qin, Lanxia Cheng, Angelica Azcatl, Jiyoung Kim, and Robert M Wallace. Remote plasma oxidation and atomic layer etching of MoS_2. *ACS Applied Materials & Interfaces*, 8(29):19119–19126, 2016.

[36] Norman MD Brown, Naiyi Cui, and Archibald McKinley. An XPS study of the surface modification of natural MoS_2 following treatment in an RF-oxygen plasma. *Applied Surface Science*, 134(1):11–21, 1998.

[37] Akihiro Inoue, Takahiro Komori, and Ken-ichi Shudo. Atomic-scale structures and electronic states of defects on Ar+-ion irradiated MoS_2. *Journal of Electron Spectroscopy and Related Phenomena*, 189:11–18, 2013.

[38] Dong Ye, Shu-Qun Wu, Yao Yu, Lin Liu, Xin-Pei Lu, and Yue Wu. Patterned graphene functionalization via mask-free scanning of micro-plasma jet under ambient condition. *Applied Physics Letters*, 104(10):103105, 2014.

[39] Chi Woong Jang, Young Tae Byun, Deok Ha Woo, Seok Lee, and Young Min Jhon. Oxygen plasma post process to obtain consistent conductance of carbon nanotubes in carbon nanotube field-effect transistors. *Applied Physics Letters*, 101(17):173104, 2012.

[40] DS Rawat, N Taylor, S Talapatra, SK Dhali, PM Ajayan, and AD Migone. Effect of surface cleaning and functionalization of nanotubes on gas adsorption. *Physical Review B*, 74(11):113403, 2006.

[41] Sanghak Yeo, Changrok Choi, Chi Woong Jang, Seok Lee, and Young Min Jhon. Sensitivity enhancement of carbon nanotube based ammonium ion sensors through surface modification by using oxygen plasma treatment. *Applied Physics Letters*, 102(7):073108, 2013.

[42] Helga Timko, F Djurabekova, K Nordlund, Leila Costelle, K Matyash, R Schneider, A Toerklep, G Arnau-Izquierdo, A Descoeudres, S Calatroni, et al. Mechanism of surface modification in the plasma-surface interaction in electrical arcs. *Physical Review B*, 81(18):184109, 2010.

[43] J Upadhyay, Do Im, S Popović, A-M Valente-Feliciano, L Phillips, and L Vušković. Plasma processing of large curved surfaces for superconducting rf cavity modification. *Physical Review Special Topics-Accelerators and Beams*, 17(12):122001, 2014.

[44] https://www.fischione.com/products/contamination-solutions/model-1020-plasma cleaner, 2014.

[45] Peter Markos and Costas M Soukoulis. *Wave propagation: from electrons to photonic crystals and left-handed materials.* Princeton University Press, 2008.

[46] BR Nag. Resonant tunneling diode. *Physics of Quantum Well Devices*, pages 188–201, 2000.

[47] Kwok Kwok Ng. *Complete guide to semiconductor devices.* Wiley Online Library, 2002.

[48] John C Slater and George F Koster. Simplified LCAO method for the periodic potential problem. *Physical Review*, 94(6):1498, 1954.

[49] W Kohn and JM Luttinger. Quantum theory of electrical transport phenomena. *Physical Review*, 108(3):590, 1957.

[50] Richard M Martin. *Electronic structure: basic theory and practical methods.* Cambridge university press, 2004.

[51] Pierre Hohenberg and Walter Kohn. Inhomogeneous electron gas. *Physical Review*, 136(3B):B864, 1964.

[52] Walter Kohn and Lu Jeu Sham. Self-consistent equations including exchange and correlation effects. *Physical Review*, 140(4A):A1133, 1965.

[53] Leonard Kleinman and DM Bylander. Efficacious form for model pseudopotentials. *Physical Review Letters*, 48(20):1425, 1982.

[54] Eiji Nakamachi, Yasutomo Uetsuji, Hiroyuki Kuramae, Kazuyoshi Tsuchiya, and Hwisim Hwang. Process crystallographic simulation for

biocompatible piezoelectric material design and generation. *Archives of Computational Methods in Engineering*, 20(2):155–183, 2013.

[55] Hai Li, Gang Lu, Zongyou Yin, Qiyuan He, Hong Li, Qing Zhang, and Hua Zhang. Optical identification of single-and few-layer MoS_2 sheets. *Small*, 8(5):682–686, 2012.

[56] Brian G Burke, Timothy J Herlihy Jr, Andrew B Spisak, and Keith A Williams. Deep UV pattern definition in PMMA. *Nanotechnology*, 19(21):215301, 2008.

[57] Norman Colthup. *Introduction to infrared and Raman spectroscopy*. Elsevier, 2012.

[58] Alejandro Molina-Sanchez and Ludger Wirtz. Phonons in single-layer and few-layer MoS_2 and WS_2. *Physical Review B*, 84(15):155413, 2011.

[59] Jakub Jadwiszczak, Colin OCallaghan, Yangbo Zhou, Daniel S Fox, Eamonn Weitz, Darragh Keane, Conor P Cullen, Ian OReilly, Clive Downing, Aleksey Shmeliov, et al. Oxide-mediated recovery of field-effect mobility in plasma-treated MoS_2. *Science Advances*, 4(3):eaao5031, 2018.

[60] Yulu Liu, Haiyan Nan, Xing Wu, Wei Pan, Wenhui Wang, Jing Bai, Weiwei Zhao, Litao Sun, Xinran Wang, and Zhenhua Ni. Layer-by-layer thinning of MoS_2 by plasma. *ACS Nano*, 7(5):4202–4209, 2013.

[61] Soo Hong Kim, Sun Woong Na, N-E Lee, Yun Woo Nam, and Young-Ho Kim. Effect of surface roughness on the adhesion properties of Cu/Cr films on polyimide substrate treated by inductively coupled oxygen plasma. *Surface and Coatings Technology*, 200(7):2072–2079, 2005.

[62] Arthur L Ruoff, Edward J Kramer, and Che-Yu Li. Improvement of adhesion of copper on polyimide by reactive ion-beam etching. *IBM Journal of Research and Development*, 32(5):626–630, 1988.

[63] Ya-Qing Bie, Yang-Bo Zhou, Zhi-Min Liao, Kai Yan, Song Liu, Qing Zhao, Shishir Kumar, Han-Chun Wu, Georg S Duesberg, Graham LW

Cross, et al. Site-specific transfer-printing of individual graphene microscale patterns to arbitrary surfaces. *Advanced Materials*, 23(34):3938–3943, 2011.

[64] Changgu Lee, Hugen Yan, Louis E Brus, Tony F Heinz, James Hone, and Sunmin Ryu. Anomalous lattice vibrations of single-and few-layer MoS_2. *ACS Nano*, 4(5):2695–2700, 2010.

[65] Min Su Kim, Giwoong Nam, Seki Park, Hyun Kim, Gang Hee Han, Jubok Lee, Krishna P Dhakal, Jae-Young Leem, Young Hee Lee, and Jeongyong Kim. Photoluminescence wavelength variation of monolayer MoS_2 by oxygen plasma treatment. *Thin Solid Films*, 590:318–323, 2015.

[66] Oriol Lopez-Sanchez, Dominik Lembke, Metin Kayci, Aleksandra Radenovic, and Andras Kis. Ultrasensitive photodetectors based on monolayer MoS_2. *Nature Nanotechnology*, 8(7):497, 2013.

[67] Caiyun Chen, Hong Qiao, Shenghuang Lin, Chi Man Luk, Yan Liu, Zaiquan Xu, Jingchao Song, Yunzhou Xue, Delong Li, Jian Yuan, et al. Highly responsive MoS_2 photodetectors enhanced by graphene quantum dots. *Scientific Reports*, 5:11830, 2015.

[68] Sungjin Wi, Hyunsoo Kim, Mikai Chen, Hongsuk Nam, L Jay Guo, Edgar Meyhofer, and Xiaogan Liang. Enhancement of photovoltaic response in multilayer MoS_2 induced by plasma doping. *ACS Nano*, 8(5):5270–5281, 2014.

[69] John J Gough, Niall McEvoy, Maria O'Brien, Alan P Bell, David McCloskey, John B Boland, Jonathan N Coleman, Georg S Duesberg, and A Louise Bradley. Dependence of photocurrent enhancements in quantum dot sensitized MoS_2 devices on MoS_2 film properties. *Advanced Functional Materials*, 28(13):1706149, 2018.

[70] Haiyan Nan, Zilu Wang, Wenhui Wang, Zheng Liang, Yan Lu, Qian Chen, Daowei He, Pingheng Tan, Feng Miao, Xinran Wang, et al. Strong photoluminescence enhancement of MoS_2 through defect engineering and oxygen bonding. *ACS Nano*, 8(6):5738–5745, 2014.

[71] Angelica Azcatl, Stephen McDonnell, Santosh KC, Xin Peng, Hong Dong, Xiaoye Qin, Rafik Addou, Greg I Mordi, Ning Lu, Jiyoung Kim, et al. MoS_2 functionalization for ultra-thin atomic layer deposited dielectrics. *Applied Physics Letters*, 104(11):111601, 2014.

[72] Long Qi, Ying Wang, Lei Shen, and Yihong Wu. Chemisorption-induced n-doping of MoS_2 by oxygen. *Applied Physics Letters*, 108(6):063103, 2016.

[73] Geonwook Yoo, Seongin Hong, Junseok Heo, and Sunkook Kim. Enhanced photoresponsivity of multilayer MoS_2 transistors using high work function MoO_x overlayer. *Applied Physics Letters*, 110(5):053112, 2017.

[74] Priyank Rastogi, Sanjay Kumar, Somnath Bhowmick, Amit Agarwal, and Yogesh Singh Chauhan. Doping strategies for monolayer MoS_2 via surface adsorption: a systematic study. *The Journal of Physical Chemistry C*, 118(51):30309–30314, 2014.

[75] Faguang Yan, Zhongming Wei, Xia Wei, Quanshan Lv, Wenkai Zhu, and Kaiyou Wang. Toward high-performance photodetectors based on 2D materials: strategy on methods. *Small Methods*, 2(5):1700349, 2018.

[76] Dominik Kufer, Ivan Nikitskiy, Tania Lasanta, Gabriele Navickaite, Frank HL Koppens, and Gerasimos Konstantatos. Hybrid 2D–0D MoS_2–PbS quantum dot photodetectors. *Advanced Materials*, 27(1):176–180, 2015.

[77] Seong Hun Yu, Youngbin Lee, Sung Kyu Jang, Jinyeong Kang, Jiwon Jeon, Changgu Lee, Jun Young Lee, Hyungjun Kim, Euyheon Hwang, Sungjoo Lee, et al. Dye-sensitized MoS_2 photodetector with enhanced spectral photoresponse. *ACS Nano*, 8(8):8285–8291, 2014.

[78] Chang-Hua Liu, You-Chia Chang, Theodore B Norris, and Zhaohui Zhong. Graphene photodetectors with ultra-broadband and high responsivity at room temperature. *Nature Nanotechnology*, 9(4):273–278, 2014.

[79] Zhenhua Sun, Zhike Liu, Jinhua Li, Guo-an Tai, Shu-Ping Lau, and Feng Yan. Infrared photodetectors based on CVD-grown graphene and PbS quantum dots with ultrahigh responsivity. *Advanced Materials*, 24(43):5878–5883, 2012.

[80] Archana Raja, Andres Montoya-Castillo, Johanna Zultak, Xiao-Xiao Zhang, Ziliang Ye, Cyrielle Roquelet, Daniel A Chenet, Arend M van der Zande, Pinshane Huang, Steffen Jockusch, et al. Energy transfer from quantum dots to graphene and MoS_2: The role of absorption and screening in two-dimensional materials. *Nano Letters*, 16(4):2328–2333, 2016.

[81] Song-Lin Li, Kazuhito Tsukagoshi, Emanuele Orgiu, and Paolo Samorì. Charge transport and mobility engineering in two-dimensional transition metal chalcogenide semiconductors. *Chemical Society Reviews*, 45(1):118–151, 2016.

[82] Nan Ma and Debdeep Jena. Charge scattering and mobility in atomically thin semiconductors. *Physical Review X*, 4(1):011043, 2014.

[83] Hsiao-Yu Chang, Weinan Zhu, and Deji Akinwande. On the mobility and contact resistance evaluation for transistors based on MoS_2 or two-dimensional semiconducting atomic crystals. *Applied Physics Letters*, 104(11):113504, 2014.

[84] Lang Zeng, Zheng Xin, Shaowen Chen, Gang Du, Jinfeng Kang, and Xiaoyan Liu. Remote phonon and impurity screening effect of substrate and gate dielectric on electron dynamics in single layer MoS_2. *Applied Physics Letters*, 103(11):113505, 2013.

[85] Song-Lin Li, Katsuyoshi Komatsu, Shu Nakaharai, Yen-Fu Lin, Mahito Yamamoto, Xiangfeng Duan, and Kazuhito Tsukagoshi. Thickness scaling effect on interfacial barrier and electrical contact to two-dimensional MoS_2 layers. *ACS Nano*, 8(12):12836–12842, 2014.

[86] Dattatray J Late, Bin Liu, HSS Ramakrishna Matte, Vinayak P Dravid, and CNR Rao. Hysteresis in single-layer MoS_2 field effect transistors. *ACS Nano*, 6(6):5635–5641, 2012.

[87] Jie Jiang, Zhouming Zheng, and Junjie Guo. Tuning the hysteresis voltage in 2D multilayer MoS_2 FETs. *Physica B: Condensed Matter*, 498:76–81, 2016.

[88] Michael S Fuhrer and James Hone. Measurement of mobility in dual-gated MoS_2 transistors. *Nature Nanotechnology*, 8(3):146–147, 2013.

[89] Sivacarendran Balendhran, Junkai Deng, Jian Zhen Ou, Sumeet Walia, James Scott, Jianshi Tang, Kang L Wang, Matthew R Field, Salvy Russo, Serge Zhuiykov, et al. Enhanced charge carrier mobility in two-dimensional high dielectric molybdenum oxide. *Advanced Materials*, 25(1):109–114, 2013.

[90] Yung-Chang Lin, Dumitru O Dumcenco, Ying-Sheng Huang, and Kazu Suenaga. Atomic mechanism of the semiconducting-to-metallic phase transition in single-layered MoS_2. *Nature Nanotechnology*, 9(5):391, 2014.

[91] Muharrem Acerce, Damien Voiry, and Manish Chhowalla. Metallic 1T phase MoS_2 nanosheets as supercapacitor electrode materials. *Nature Nanotechnology*, 10(4):313, 2015.

[92] M Kan, JY Wang, XW Li, SH Zhang, YW Li, Y Kawazoe, Q Sun, and P Jena. Structures and phase transition of a MoS_2 monolayer. *The Journal of Physical Chemistry C*, 118(3):1515–1522, 2014.

[93] Adriano Ambrosi, Zdeněk Sofer, and Martin Pumera. 2H to 1T phase transition and hydrogen evolution activity of MoS_2, $MoSe_2$, WS_2 and WSe_2 strongly depends on the MX_2 composition. *Chemical Communications*, 51(40):8450–8453, 2015.

[94] Paolo Giannozzi, Stefano Baroni, Nicola Bonini, Matteo Calandra, Roberto Car, Carlo Cavazzoni, Davide Ceresoli, Guido L Chiarotti, Matteo Cococcioni, Ismaila Dabo, et al. QUANTUM ESPRESSO: a modular and open-source software project for quantum simulations of materials. *Journal of physics: Condensed matter*, 21(39):395502, 2009.

[95] KD Bronsema, JL De Boer, and F Jellinek. On the structure of molybdenum diselenide and disulfide. *Zeitschrift für anorganische und allgemeine Chemie*, 540(9-10):15–17, 1986.

[96] PA Young. Lattice parameter measurements on molybdenum disulphide. *Journal of Physics D: Applied Physics*, 1(7):936, 1968.

[97] Emilia Ridolfi, Duy Le, TS Rahman, ER Mucciolo, and CH Lewenkopf. A tight-binding model for MoS_2 monolayers. *Journal of Physics: Condensed Matter*, 27(36):365501, 2015.

[98] E Cappelluti, Rafael Roldán, JA Silva-Guillén, Pablo Ordejón, and F Guinea. Tight-binding model and direct-gap/indirect-gap transition in single-layer and multilayer MoS_2. *Physical Review B*, 88(7):075409, 2013.

[99] Sohail Ahmad and Sugata Mukherjee. A comparative study of electronic properties of bulk MoS_2 and its monolayer using DFT technique: application of mechanical strain on MoS_2 monolayer. 2014.

[100] John P Perdew, Kieron Burke, and Matthias Ernzerhof. Generalized gradient approximation made simple. *Physical Review Letters*, 77(18):3865, 1996.

[101] Andrew M Rappe, Karin M Rabe, Efthimios Kaxiras, and JD Joannopoulos. Optimized pseudopotentials. *Physical Review B*, 41(2):1227, 1990.

[102] HSS Ramakrishna Matte, A Gomathi, Arun K Manna, Dattatray J Late, Ranjan Datta, Swapan K Pati, and CNR Rao. MoS_2 and WS_2 analogues of graphene. *Angewandte Chemie International Edition*, 49(24):4059–4062, 2010.

[103] Nevill F Mott. The basis of the electron theory of metals, with special reference to the transition metals. *Proceedings of the Physical Society. Section A*, 62(7):416, 1949.

[104] Eva Pavarini, Erik Koch, Frithjof Anders, and Mark Jarrell. Correlated electrons: from models to materials. *Reihe Modeling and Simulation*, 2, 2012.

[105] Goki Eda, Hisato Yamaguchi, Damien Voiry, Takeshi Fujita, Mingwei Chen, and Manish Chhowalla. Photoluminescence from chemically exfoliated MoS_2. *Nano Letters*, 11(12):5111–5116, 2011.

[106] Shinichiro Mouri, Yuhei Miyauchi, and Kazunari Matsuda. Tunable photoluminescence of monolayer MoS_2 via chemical doping. *Nano Letters*, 13(12):5944–5948, 2013.

[107] Chendong Zhang, Amber Johnson, Chang-Lung Hsu, Lain-Jong Li, and Chih-Kang Shih. Direct imaging of band profile in single layer MoS_2 on graphite: quasiparticle energy gap, metallic edge states, and edge band bending. *Nano Letters*, 14(5):2443–2447, 2014.

[108] Qu Yue, Jun Kang, Zhengzheng Shao, Xueao Zhang, Shengli Chang, Guang Wang, Shiqiao Qin, and Jingbo Li. Mechanical and electronic properties of monolayer MoS_2 under elastic strain. *Physics Letters A*, 376(12-13):1166–1170, 2012.

[109] Jianmin Tao, John P Perdew, Viktor N Staroverov, and Gustavo E Scuseria. Climbing the density functional ladder: Nonempirical meta–generalized gradient approximation designed for molecules and solids. *Physical Review Letters*, 91(14):146401, 2003.

[110] Takeshi Yanai, David P Tew, and Nicholas C Handy. A new hybrid exchange–correlation functional using the Coulomb-attenuating method (CAM-B3LYP). *Chemical Physics Letters*, 393(1-3):51–57, 2004.

[111] Jon Baker and Peter Pulay. Assessment of the OLYP and O3LYP density functionals for first-row transition metals. *Journal of Computational Chemistry*, 24(10):1184–1191, 2003.

[112] Jochen Heyd, Gustavo E Scuseria, and Matthias Ernzerhof. Hybrid functionals based on a screened Coulomb potential. *The Journal of Chemical Physics*, 118(18):8207–8215, 2003.

[113] Alfredo Ramirez-Torres, Duy Le, and Talat S Rahman. Effect of monolayer supports on the electronic structure of single-layer MoS_2. In *IOP Conference Series: Materials Science and Engineering*, volume 76, page 012011. IOP Publishing, 2015.

[114] Ashok Kumar and PK Ahluwalia. A first principle comparative study of electronic and optical properties of 1H–MoS_2 and 2H–MoS_2. *Materials Chemistry and Physics*, 135(2-3):755–761, 2012.

[115] Hannu-Pekka Komsa and Arkady V Krasheninnikov. Electronic structures and optical properties of realistic transition metal dichalcogenide heterostructures from first principles. *Physical Review B*, 88(8):085318, 2013.

[116] C Ataca and S Ciraci. Functionalization of single-layer MoS_2 honeycomb structures. *The Journal of Physical Chemistry C*, 115(27):13303–13311, 2011.

[117] Diana Y Qiu, H Felipe, and Steven G Louie. Optical spectrum of MoS_2: many-body effects and diversity of exciton states. *Physical Review Letters*, 111(21):216805, 2013.

[118] Eugene S Kadantsev and Pawel Hawrylak. Electronic structure of a single MoS_2 monolayer. *Solid State Communications*, 152(10):909–913, 2012.

[119] D Cao, HB Shu, TQ Wu, ZT Jiang, ZW Jiao, MQ Cai, and WY Hu. First-principles study of the origin of magnetism induced by intrinsic defects in monolayer MoS_2. *Applied Surface Science*, 361:199–205, 2016.

[120] Yiren Wang, Li-Ting Tseng, Peter P Murmu, Nina Bao, John Kennedy, Mihail Ionesc, Jun Ding, Kiyonori Suzuki, Sean Li, and Jiabao Yi. De-

fects engineering induced room temperature ferromagnetism in transition metal doped MoS_2. *Materials & Design*, 121:77–84, 2017.

[121] Jiangang He, Kechen Wu, Rongjian Sa, Qiaohong Li, and Yongqin Wei. Magnetic properties of nonmetal atoms absorbed MoS_2 monolayers. *Applied Physics Letters*, 96(8):082504, 2010.

[122] Yandong Ma, Ying Dai, Meng Guo, Chengwang Niu, Jibao Lu, and Baibiao Huang. Electronic and magnetic properties of perfect, vacancy-doped, and nonmetal adsorbed $MoSe_2$, $MoTe_2$ and WS_2 monolayers. *Physical Chemistry Chemical Physics*, 13(34):15546–15553, 2011.

[123] Shiming Yan, Wen Qiao, Xueming He, Xiaobing Guo, Li Xi, Wei Zhong, and Youwei Du. Enhancement of magnetism by structural phase transition in MoS_2. *Applied Physics Letters*, 106(1):012408, 2015.

[124] Bernard Dennis Cullity and Chad D Graham. *Introduction to magnetic materials*. John Wiley & Sons, 2011.

[125] Giovanni B Bachelet and M Schlüter. Relativistic norm-conserving pseudopotentials. *Physical Review B*, 25(4):2103, 1982.

[126] Rafael Roldán, María Pilar López-Sancho, F Guinea, E Cappelluti, JA Silva-Guillén, and Pablo Ordejón. Momentum dependence of spin–orbit interaction effects in single-layer and multi-layer transition metal dichalcogenides. *2D Materials*, 1(3):034003, 2014.

[127] K Kośmider, Jhon W González, and Joaquín Fernández-Rossier. Large spin splitting in the conduction band of transition metal dichalcogenide monolayers. *Physical Review B*, 88(24):245436, 2013.

[128] Ximo S Chu, Duo O Li, Alexander A Green, and Qing Hua Wang. Formation of MoO_3 and WO_3 nanoscrolls from MoS_2 and WS_2 with atmospheric air plasma. *Journal of Materials Chemistry C*, 5(43):11301–11309, 2017.

[129] Jianqi Zhu, Zhichang Wang, Hua Yu, Na Li, Jing Zhang, JianLing Meng, Mengzhou Liao, Jing Zhao, Xiaobo Lu, Luojun Du, et al. Argon plasma

induced phase transition in monolayer MoS_2. *Journal of the American Chemical Society*, 139(30):10216–10219, 2017.

[130] R Tsu and Leo Esaki. Tunneling in a finite superlattice. *Applied Physics Letters*, 22(11):562–564, 1973.

[131] DC Hutchings. Transfer matrix approach to the analysis of an arbitrary quantum well structure in an electric field. *Applied Physics Letters*, 55(11):1082–1084, 1989.

[132] FC Zhang, N Dai, H Luo, N Samarth, M Dobrowolska, JK Furdyna, and LR Ram-Mohan. Observation of localized above-barrier excitons in type-i superlattices. *Physical Review Letters*, 68(21):3220, 1992.

[133] A Matulis, FM Peeters, and P Vasilopoulos. Wave-vector-dependent tunneling through magnetic barriers. *Physical Review Letters*, 72(10):1518, 1994.

[134] Xue-Hua Wang, Ben-Yuan Gu, and Guo-Zhen Yang. Coupling between the transverse and longitudinal componentsof an electron in resonant tunneling. *Physical Review B*, 55(15):9340, 1997.

[135] Yong Guo, Bing-Lin Gu, Jing-Zhi Yu, Zhong Zeng, and Yoshiyuki Kawazoe. Resonant tunneling in step-barrier structures under an applied electric field. *Journal of Applied Physics*, 84(2):918–924, 1998.

[136] Björn Jonsson and Sverre T Eng. Solving the schrodinger equation in arbitrary quantum-well potential profiles using the transfer matrix method. *IEEE Journal of Quantum Electronics*, 26(11):2025–2035, 1990.

[137] Daniela Dragoman and Mircea Dragoman. Negative differential resistance of electrons in graphene barrier. *Applied Physics Letters*, 90(14):143111, 2007.

[138] Amretashis Sengupta and Santanu Mahapatra. Negative differential resistance and effect of defects and deformations in MoS_2 armchair nanoribbon metal-oxide-semiconductor field effect transistor. *Journal of Applied Physics*, 114(19):194513, 2013.

[139] Tania Roy, Mahmut Tosun, Xi Cao, Hui Fang, Der-Hsien Lien, Peida Zhao, Yu-Ze Chen, Yu-Lun Chueh, Jing Guo, and Ali Javey. Dual-gated MoS_2/WSe_2 van der waals tunnel diodes and transistors. *ACS Nano*, 9(2):2071–2079, 2015.

[140] Wencan Jin, Po-Chun Yeh, Nader Zaki, Datong Zhang, Jerzy T Sadowski, Abdullah Al-Mahboob, Arend M van Der Zande, Daniel A Chenet, Jerry I Dadap, Irving P Herman, et al. Direct measurement of the thickness-dependent electronic band structure of MoS_2 using angle-resolved photoemission spectroscopy. *Physical Review Letters*, 111(10):106801, 2013.

[141] Judith Moosburger-Will, Jörg Kündel, Matthias Klemm, Siegfried Horn, Philip Hofmann, Udo Schwingenschlögl, and Volker Eyert. Fermi surface of MoO_2 studied by angle-resolved photoemission spectroscopy, de haas–van alphen measurements, and electronic structure calculations. *Physical Review B*, 79(11):115113, 2009.

[142] V Stoeberl, M Abbate, LMS Alves, CAM dos Santos, and RJO Mossanek. X-ray spectroscopy and electronic structure of MoO_2. *Journal of Alloys and Compounds*, 691:138–143, 2017.

[143] Volker Eyert, R Horny, KH Höck, and S Horn. Embedded peierls instability and the electronic structure of MoO_2. *Journal of Physics: Condensed Matter*, 12(23):4923, 2000.

[144] K Inzani, M Nematollahi, F Vullum-Bruer, T Grande, TW Reenaas, and SM Selbach. Electronic properties of reduced molybdenum oxides. *Physical Chemistry Chemical Physics*, 19(13):9232–9245, 2017.

[145] Keith T Butler, Rachel Crespo-Otero, John Buckeridge, David O Scanlon, Edward Bovill, David Lidzey, and Aron Walsh. Band energy control of molybdenum oxide by surface hydration. *Applied Physics Letters*, 107(23):231605, 2015.

[146] Bruno S Dandogbessi and Omololu Akin-Ojo. First principles prediction of the electronic structure and carrier mobilities of biaxially

strained molybdenum trioxide (MoO_3). *Journal of Applied Physics*, 120(5):055105, 2016.

[147] AH Reshak. Specific features of electronic structures and optical susceptibilities of molybdenum oxide. *RSC Advances*, 5(28):22044–22052, 2015.

[148] C Vieu, F Carcenac, A Pepin, Y Chen, M Mejias, A Lebib, L Manin-Ferlazzo, L Couraud, and H Launois. Electron beam lithography: resolution limits and applications. *Applied Surface Science*, 164(1):111–117, 2000.

[149] Vitor R Manfrinato, Lihua Zhang, Dong Su, Huigao Duan, Richard G Hobbs, Eric A Stach, and Karl K Berggren. Resolution limits of electron-beam lithography toward the atomic scale. *Nano Letters*, 13(4):1555–1558, 2013.

[150] David AB Miller. *Quantum mechanics for scientists and engineers.* Cambridge University Press, 2008.

[151] Hartwin Peelaers and Chris G Van de Walle. Effects of strain on band structure and effective masses in MoS_2. *Physical Review B*, 86(24):241401, 2012.

[152] Ahmet Avsar, Ivan J Vera-Marun, Jun You Tan, Kenji Watanabe, Takashi Taniguchi, Antonio H Castro Neto, and Barbaros Ozyilmaz. Air-stable transport in graphene-contacted, fully encapsulated ultrathin black phosphorus-based field-effect transistors. *ACS Nano*, 9(4):4138–4145, 2015.

[153] Xu Cui, Gwan-Hyoung Lee, Young Duck Kim, Ghidewon Arefe, Pinshane Y Huang, Chul-Ho Lee, Daniel A Chenet, Xian Zhang, Lei Wang, Fan Ye, et al. Multi-terminal transport measurements of MoS_2 using a van der waals heterostructure device platform. *Nature Nanotechnology*, 10(6):534–540, 2015.

[154] Xiaodong Li, Jeffrey T Mullen, Zhenghe Jin, Kostyantyn M Borysenko, M Buongiorno Nardelli, and Ki Wook Kim. Intrinsic electrical transport properties of monolayer silicene and MoS_2 from first principles. *Physical Review B*, 87(11):115418, 2013.

[155] Debdeep Jena and Aniruddha Konar. Enhancement of carrier mobility in semiconductor nanostructures by dielectric engineering. *Physical Review Letters*, 98(13):136805, 2007.

[156] Bhim Chamlagain, Qing Li, Nirmal Jeevi Ghimire, Hsun-Jen Chuang, Meeghage Madusanka Perera, Honggen Tu, Yong Xu, Minghu Pan, Di Xaio, Jiaqiang Yan, et al. Mobility improvement and temperature dependence in $MoSe_2$ field-effect transistors on parylene-C substrate. *ACS Nano*, 8(5):5079–5088, 2014.

[157] HS Song, SL Li, L Gao, Y Xu, K Ueno, J Tang, YB Cheng, and K Tsukagoshi. High-performance top-gated monolayer SnS_2 field-effect transistors and their integrated logic circuits. *Nanoscale*, 5(20):9666–9670, 2013.

[158] Jingli Wang, Songlin Li, Xuming Zou, Johnny Ho, Lei Liao, Xiangheng Xiao, Changzhong Jiang, Weida Hu, Jianlu Wang, and Jinchai Li. Integration of High-k Oxide on MoS_2 by using ozone pretreatment for high-performance MoS_2 top-gated transistor with thickness-dependent carrier scattering investigation. *Small*, 11(44):5932–5938, 2015.

[159] IN Hulea, Simone Fratini, H Xie, CL Mulder, NN Iossad, G Rastelli, S Ciuchi, and AF Morpurgo. Tunable fröhlich polarons in organic single-crystal transistors. *Nature Materials*, 5(12):982–986, 2006.

[160] Chris Bishop, Christopher M Bishop, et al. *Neural networks for pattern recognition.* Oxford University Press, 1995.

[161] Kumpati S Narendra and Kannan Parthasarathy. Identification and control of dynamical systems using neural networks. *IEEE Transactions on Neural Networks*, 1(1):4–27, 1990.

[162] Jim X Chen. The evolution of computing: AlphaGo. *Computing in Science & Engineering*, 18(4):4–7, 2016.

[163] Janardan Misra and Indranil Saha. Artificial neural networks in hardware: A survey of two decades of progress. *Neurocomputing*, 74(1-3):239–255, 2010.

[164] Yongtae Kim, Yong Zhang, and Peng Li. A digital neuromorphic VLSI architecture with memristor crossbar synaptic array for machine learning. In *SOC Conference (SOCC), 2012 IEEE International*, pages 328–333. IEEE, 2012.

[165] H John Caulfield, Jason Kinser, and Steven K Rogers. Optical neural networks. *Proceedings of the IEEE*, 77(10):1573–1583, 1989.

[166] Kuk-Hwan Kim, Siddharth Gaba, Dana Wheeler, Jose M Cruz-Albrecht, Tahir Hussain, Narayan Srinivasa, and Wei Lu. A functional hybrid memristor crossbar-array/CMOS system for data storage and neuromorphic applications. *Nano Letters*, 12(1):389–395, 2011.

[167] Miao Hu, Hai Li, Yiran Chen, Qing Wu, Garrett S Rose, and Richard W Linderman. Memristor crossbar-based neuromorphic computing system: A case study. *IEEE Transactions on Neural Networks and Learning Systems*, 25(10):1864–1878, 2014.

[168] Gun Hwan Kim, Jong Ho Lee, Youngbae Ahn, Woojin Jeon, Seul Ji Song, Jun Yeong Seok, Jung Ho Yoon, Kyung Jean Yoon, Tae Joo Park, and Cheol Seong Hwang. 32 × 32 crossbar array resistive memory composed of a stacked Schottky diode and unipolar resistive memory. *Advanced Functional Materials*, 23(11):1440–1449, 2013.

[169] Mirko Prezioso, Farnood Merrikh-Bayat, BD Hoskins, GC Adam, Konstantin K Likharev, and Dmitri B Strukov. Training and operation of an integrated neuromorphic network based on metal-oxide memristors. *Nature*, 521(7550):61, 2015.

[170] Sung Hyun Jo, Ting Chang, Idongesit Ebong, Bhavitavya B Bhadviya, Pinaki Mazumder, and Wei Lu. Nanoscale memristor device as synapse in neuromorphic systems. *Nano Letters*, 10(4):1297–1301, 2010.

[171] Zhongrui Wang, Saumil Joshi, Sergey E Savelev, Hao Jiang, Rivu Midya, Peng Lin, Miao Hu, Ning Ge, John Paul Strachan, Zhiyong Li, et al. Memristors with diffusive dynamics as synaptic emulators for neuromorphic computing. *Nature Materials*, 16(1):101, 2017.

[172] Miao Wang, Songhua Cai, Chen Pan, Chenyu Wang, Xiaojuan Lian, Ye Zhuo, Kang Xu, Tianjun Cao, Xiaoqing Pan, Baigeng Wang, et al. Robust memristors based on layered two-dimensional materials. *Nature Electronics*, 1(2):130, 2018.

[173] Vinod K Sangwan, Hong-Sub Lee, Hadallia Bergeron, Itamar Balla, Megan E Beck, Kan-Sheng Chen, and Mark C Hersam. Multi-terminal memtransistors from polycrystalline monolayer molybdenum disulfide. *Nature*, 554(7693):500, 2018.

[174] Yuchao Yang, Bing Chen, and Wei D Lu. Memristive physically evolving networks enabling the emulation of heterosynaptic plasticity. *Advanced Materials*, 27(47):7720–7727, 2015.

[175] Tim VP Bliss and Graham L Collingridge. A synaptic model of memory: long-term potentiation in the hippocampus. *Nature*, 361(6407):31, 1993.

[176] Stefanie Kaech and Gary Banker. Culturing hippocampal neurons. *Nature Protocols*, 1(5):2406, 2006.

[177] Dmitri B Strukov, Gregory S Snider, Duncan R Stewart, and R Stanley Williams. The missing memristor found. *Nature*, 453(7191):80, 2008.

[178] Shahar Kvatinsky, Eby G Friedman, Avinoam Kolodny, and Uri C Weiser. The desired memristor for circuit designers. *IEEE Circuits and Systems Magazine*, 13(2):17–22, 2013.

[179] Habib Rostami, Ali G Moghaddam, and Reza Asgari. Effective lattice Hamiltonian for monolayer $\mathrm{MoS_2}$: Tailoring electronic structure

with perpendicular electric and magnetic fields. *Physical Review B*, 88(8):085440, 2013.

[180] Habib Rostami and Reza Asgari. Intrinsic optical conductivity of modified Dirac fermion systems. *Physical Review B*, 89(11):115413, 2014.

[181] RL Stamps. Mechanisms for exchange bias. *Journal of Physics D: Applied Physics*, 33(23):R247, 2000.

[182] NC Koon. Calculations of exchange bias in thin films with ferromagnetic/antiferromagnetic interfaces. *Physical Review Letters*, 78(25):4865, 1997.

[183] Claude Amsler. Nuclear and particle physics. *Nuclear and Particle Physics, by Amsler, Claude. ISBN: 978-0-7503-1140-3. IOP ebooks. Bristol, UK: IOP Publishing, 2015*, 2015.

[184] Willis E Lamb Jr and Robert C Retherford. Fine structure of the hydrogen atom by a microwave method. *Physical Review*, 72(3):241, 1947.

[185] Frank Herman, Charles D Kuglin, Kermit F Cuff, and Richard L Kortum. Relativistic corrections to the band structure of tetrahedrally bonded semiconductors. *Physical Review Letters*, 11(12):541, 1963.

[186] LF Mattheiss and RE Dietz. Relativistic tight-binding calculation of core-valence transitions in Pt and Au. *Physical Review B*, 22(4):1663, 1980.

[187] Craig S Lent, Marshall A Bowen, John D Dow, Robert S Allgaier, Otto F Sankey, and Eliza S Ho. Relativistic empirical tight-binding theory of the energy bands of GeTe, SnTe, PbTe, PbSe, PbS, and their alloys. *Superlattices and Microstructures*, 2(5):491–499, 1986.

[188] Frank Herman, Richard L Kortum, Irene B Ortenburger, et al. Relativistic band structure of GeTe, SnTe, PbTe, PbSe, and PbS. *Le Journal de Physique Colloques*, 29(C4):C4–62, 1968.

[189] N Egede Christensen. Relativistic band structure calculations. *International Journal of Quantum Chemistry*, 25(1):233–261, 1984.